SELF-FOLDING TRANSFORMER ROBOT BASED ON BIDIRECTIONAL SHAPE MEMORY POLYMER COMPOSITE ACTUATORS

by

Shuyang Chen

A thesis submitted to The Johns Hopkins University in conformity with the requirements for the degree of Master of Science.

Baltimore, Maryland

May, 2016

Abstract

Self-folding is universal in nature. The concept of self-folding has attracted interests from standpoints of both fundamental scientific research and technological innovations due to the advantages of self-folding over traditional manufacturing methods. Driven by the interests in self-folding, people have developed artificial self-folding structures at different length scales based on specific actuators that can realize unidirectional folding movement.

To overcome the limitations of unidirectional actuators in fabricating more complex structures, people also developed actuators that can realize bidirectional folding action. Most of these actuators are based on shape memory effects of shape memory polymers and alloys. However, the applicability of these bidirectional actuators is restricted by drawbacks such as complexity in fabrication and programming. We have developed and characterized an easy-to-fabricate and low-cost shape memory polymer composite actuator which could enable bidirectional folding action with adjustable angles by simple programming procedures. Based on analytical, numerical, and experimental analysis, we have shown that we can control the folding angle and

the folding force by adjusting the thickness ratio and/or the prestrain of the actuator.

To demonstrate the potential application of the actuator, we reported a self-folding transformer robot which folds from two-dimensional (2D) sheet into three-dimensional (3D) configuration by itself and transforms between different 3D shapes via controlled heating of the actuators. Then, we presented the ability of the robot to do obstacle avoidance for practical applications.

By combining findings from polymer science and robotics, we envision that the actuator can provide new opportunities for various applications including a soft robot that can transform its shape depending on surrounding environment and navigate itself.

Primary Reader: Prof. Sung Hoon Kang,

Secondary Reader: Prof. Chen Li.

Dedication

This thesis is dedicated to my beloved parents,
Mrs. Longzhi Hou and Mr. Qixiang Chen.
I will always be your pride.

Acknowledgments

I gratefully acknowledge the support of Johns Hopkins University Whiting School of Engineering start-up fund for this research.

I give my most sincere gratitude to my research advisor Professor Sung Hoon Kang, who is the pivot in my academic and research career. It is my deep honor to be his student. Also I would like to acknowledge Professors Thao (Vicky) Nguyen and Kevin Hemker for their advice and kindly letting me use the equipment and device of their lab. In addition, I would like to thank Professor Chen Li for being my thesis reader.

It is hard for me to thank enough to the professors and mentors who helped and guided me throughout the difficult as well as productive path of Hopkins Mechanical Engineering for two years. Apart from my academic advisor Professor Noah Cowan, I would like to acknowledge Professor Markus Hilpert, Professor David Kraemer, Professor Simon Leonard, Professor Marin Kobilarov, Professor Cila Herman and Professor Fred Torcaso for without their lectures and teachings this project wouldn't be realized by me. Mr. Mike Bernard, the Academic Program Administrator of Mechanical Engineering Department, gave me help in lots of aspects.

ACKNOWLEDGMENTS

A special gratitude goes to Lichen Fang, Jing Li, Yitao Chen, and all the other friendly past members of the Kang Group for always being there to give a hand to me with different problems during the long research process. In particular I would thank Dr. Santiago Orrego for his inspiration and willingness to help me even during his busy times, Dr. Suman Dasgupta for his help with the load cell training, and Jingkai Guo for helping me with the Finite Element Analysis.

It is like a dream and fortune for me to spend two invaluable years at Johns Hopkins University. I would also like to thank all the people that contribute to this highly rated university. I wish you all the best in the future.

Contents

List of Figures

List of Tables

Chapter 1

Introduction

1.1 Inspiration: Self-Folding Structures

Folding and unfolding are universal phenomena in nature such as winged insects,[1] tree leaves[2] (Figure 1.1) and brains.[3] Recently, there are increasing interests in folding due to its advantages over traditional manufacturing methods (e.g. injection molding, machining, forming, and joining), including reduced material consumption and creation of structures with improved strength-to-weight ratios.[4] Moreover, theoretical work has proven that folding is capable of achieving a large set of target geometries.[5] Origami[6]-based folding/unfolding mechanisms have contributed to lots of technological applications including space telescope,[7] robotics,[8] foldable photovoltaics,[9] microelectromechanical systems (MEMS),[10] surgery[11] and electronic devices,[12] etc. One of the well-known examples is the *James Webb Space Telescope*, the successor of *Hubble*

Space Telescope, operated by the *Space Telescope Science Institute* located in JHU campus. The *James Webb Space Telescope* is too large to fit into a rocket in its final shape so engineers have designed it to unfold like origami after its launch, as shown in Figure 1.2. People (Robert J. Lang, Erik Demaine, and Tomohiro Tachi,etc.) also developed algorithms and software to obtain the corresponding 2D crease pattern of one 3D shape such as *Origamizer* (developed by Tomohiro Tachi), as well as simulating the resulting 3D configuration when one specific 2D crease pattern is used as input, such as *Rigid Origami Simulator* (developed by Tomohiro Tachi).

Figure 1.1: Unfolding manner of leaves of hornbeam: (a) a bud, (b) buds just after opening, (c) an early stage of unfolding, and (d) corrugated leaves. Reprinted with permission from Reference.[2] ©1998 The Royal Society.

Self-folding structures, broadly refer to systems in which structures curve or fold-up either spontaneously or in response to a stimulus,[14] are more attractive than folding in many applications as they save the expensive infrastructure investment to auto-

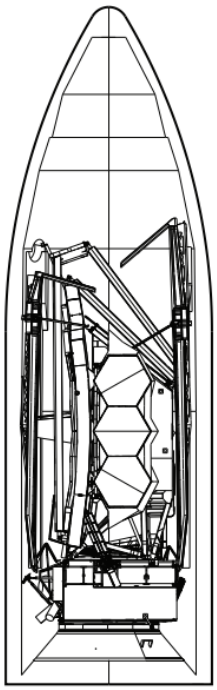

(a)

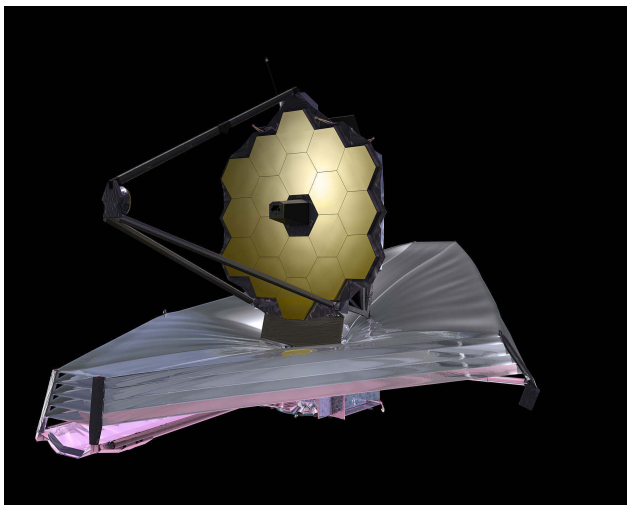

(b)

Figure 1.2: The *James Webb Space Telescope* unfolds like origami after its launch. The configuration of the space telescope before unfolding in rocket (a) and the configuration of the space telescope after unfolding in space (b). Reprinted with permission from Reference.[13]

mate the folding action. Moreover, the self-folding concept is promising to realize fabrication of functional self-folding machines and autonomous assembly of complex geometries across multiple length scales. To enable artificial self-folding structures, people also developed actuators which could realize folding action, including unidirectional and bidirectional folding actuators.

1.2 Actuation Mechanisms for Self-folding

1.2.1 Unidirectional Folding Actuators

Reliable self-folding actuation mechanism would be a boost to automated fabrication of complex folded devices, as well as to self-deployable systems. A variety of actuation mechanisms for unidirectional self-folding action have been developed based on material properties. Unidirectional folding actuator leads to the single shape of the 3D object, or only to the assembly process without automated disassembly. Common self-folding mechanisms include magnetic fields, residual stress, shape memory materials such as shape memory alloy (SMA) and prestrained polymer sheet, hydrogel and dielectric elastomer, etc.

• Magnetic Fields

Magnetic field can reliably offer relatively large force or torque for the folding action so that it has been adopted to realize angular displacement of hinged microstructures. For example, in 1999, Yi et al.[15] described the actuation of hinged, surface microma-

chined structures using a magnetic field. Electroplated magnetic material (Permalloy) is integrated with specific types of hinged microstructures (Figure 1.3). Rotation of the flap happens when strength of magnetic field (H_{ext}) exceeds a threshold value. Under a given external magnetic field, the angular displacement of a hinged structure would be determined by the volume of the magnetic material (Permalloy) or by the stiffness of an auxiliary flexural loading spring.

Actuation based on magnetic field has the following advantages: 1) high efficiency and yield in chips-scale or wafer-scale parallel actuation; 2) minimum dedicated chip area for active actuation; and 3) fast response time.[15] However, additional cost would be introduced to generate and program the magnetic field.

• Residual Stress

Residual stresses are stresses that remain in a solid material after the original cause of the stresses has been removed. Residual stresses can occur through a variety of mechanisms including inelastic (plastic) deformations, temperature gradients (during thermal cycle) or structural changes (phase transformation).

Residual stress could be used to produce complex three-dimensional (3D) microdevices and microstructures. For instance, Bassik et al.[16] presented lithographically patterned microscaled thin films which would fold spontaneously via residual stress with any desired angle. The strategy uses thin film sheets with multilayer hinges consisting of chromium (Cr) and copper (Cu) layers (Figure 1.4). Folding occurs spontaneously as a result of the large ($\sim$ 1 GPa) residual tensile stress within the

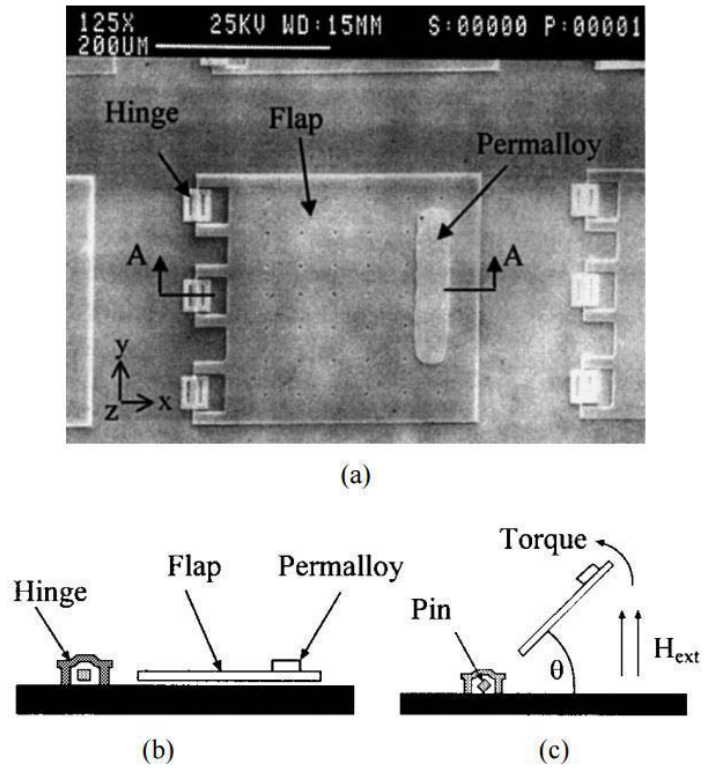

Figure 1.3: (a) An SEM micrograph of a specific type hinged flap which is capable of rotating about the y-axis. The primary method for controlling its angular displacement is the use of different Permalloy volumes. (b) Schematic cross-sectional view (A-A) of the hinged flap when there is no magnetic field applied. (c) When strength of magnetic field (H_{ext}) exceeds a threshold value, the flap rotates out of plane to reach $\theta = 90°$. Reprinted with permission from Reference.[15] ©1999 IEEE.

Cr film, while the Cu provides structural support. The folding angle is adjusted by changing r, which is defined as the ratio of the length of the square rigid panel to that of the hinge. The microstructures could realize bidirectional folding (mountain and valley folds) only globally instead of locally so that it is still categorized by "unidirectional" folding.

• Shape Memory Alloy (SMA)

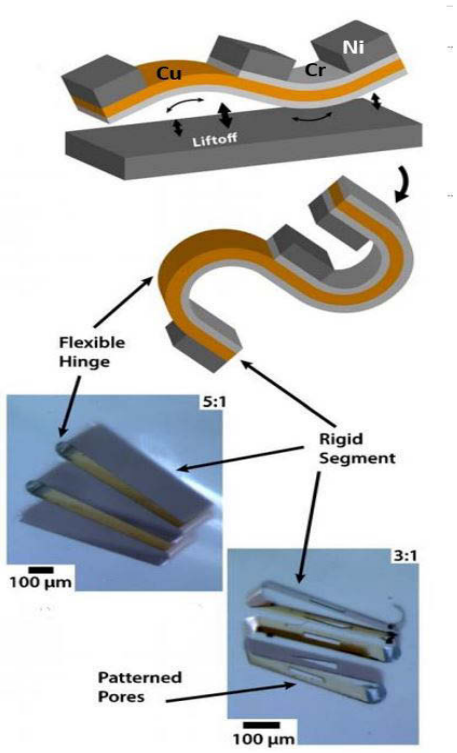

Figure 1.4: *top* Folding occurs as a result of the large residual tensile stress via dissolving the sacrificial layer (which is not shown here). *middle* An assembled structure with mountain and valley folds. *down* Optical micrograph of two assembled structures with r = 5 and r= 3 ratio, respectively. Reprinted with permission from Reference.[16] ©2009 American Institute of Physics.

Shape memory alloys (SMAs) are materials that exhibit the ability to memorize shapes through a thermally induced solid state phase transition. The recovery stress provided by the SMA due to shape memory effect can be used to offer force or torque for the folding action. In 2010, Hawkes et al. used shape memory alloys (SMAs) to actuate a sheet in programmable matter.[17] The sheet (Figure 1.5a) is able to fold into a set of predetermined shapes by activating embedded SMA actuators which are specifically patterned on the sheet via Joule heating (Figure 1.5b). However, it is difficult to program SMAs. This method depends on complex fabrication processes

and material systems, and would not be efficient in the assembly of specific target structures. Similar works were published later.[18,19]

• Prestrained Polymer Sheet

Prestrained polymer is one kind of shape memory material which would return to memorized shape by shrinkage in response to external localized heating stimuli. The recovery stress caused by the shrinkage can be used as a source for folding. In 2012, Liu et al.[20] introduced the self-folding of thin prestrained polystyrene (also known as Shrinky-Dinks), which would shrink in-plane if heated uniformly. Black ink patterned on either side of the polymer sheet is used to provide localized absorption of light, which heats the underlying polymers to temperatures above their glass transition temperatures. At these temperatures, the predefined inked regions (i.e. hinges) relax and shrink, thereby folded structures can be realized by choosing an appropriate geometry of the inked pattern (such as line width) and the support temperature. Mountain and valley folds are achieved by putting ink on either side of the polymer sheet, respectively. Self-folding is therefore achieved in a simple way without the use of complex materials and fabrication steps (as shown in Figure 1.6).

Two years later, Felton et al.[8] demonstrated their work of a crawling robot that folds itself automatically by employing the similar idea reported by Liu et al.[20] The robot starts as a flat sheet with embedded electronics and mechanical devices, and transforms autonomously into a functional movable machine (Figure 1.7a). In order to accomplish that, they developed shape memory composites (Figure 1.7b) which

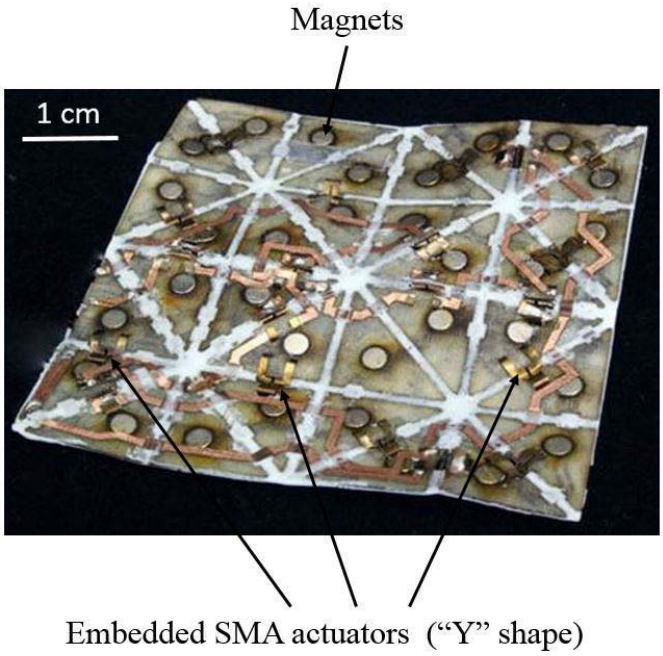

(a)

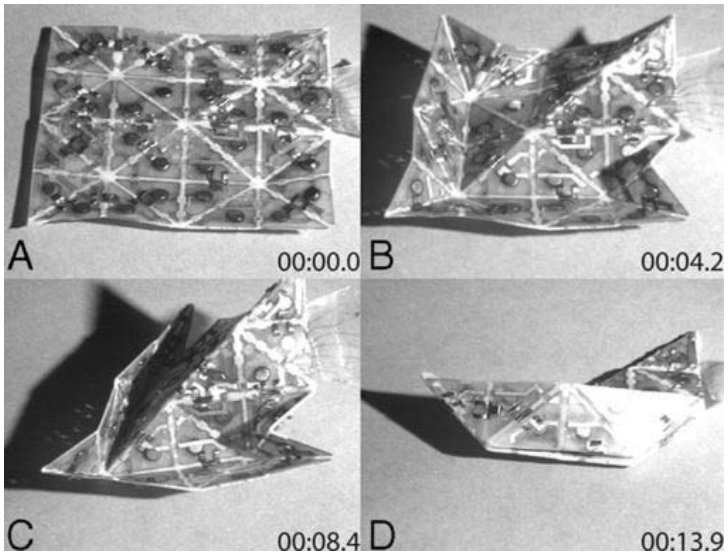

(b)

Figure 1.5: The 2D self-folding sheet with embedded SMA actuators (a) and its transformation process folding into a boat actuated by inputting one amp current (b). Reprinted with permission from Reference.[17] ©2010 PNAS.

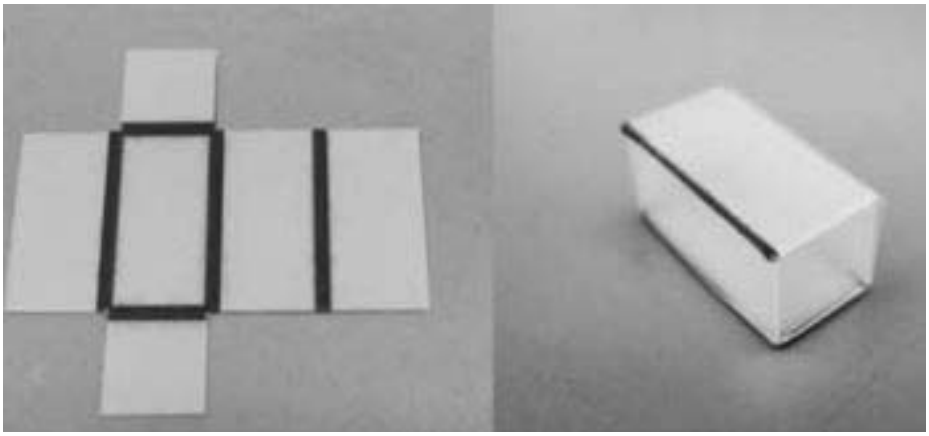

Figure 1.6: *right* Rectangular box (20 mm × 10 mm × 10 mm), which is created by self-folding of Shrinky-Dinks patterned with black ink (width = 1.5 mm) on the *left*. Reprinted with permission from Reference.[20] ©2011 Royal Society of Chemistry.

are composed of Shrinky-Dinks, papers and patterned copper layer (used as heating element). The composites fold themselves along embedded hinges in response of heat generated by the copper layer via Joule Heating. The robot can thereby fold itself and then walk away without human intervention but under the control of a micro-controller. This robot demonstrates the practical application as well as the potential both for complex self-folding machines and autonomous, self-controlled assembly of the self-folding concepts drawn from natural contexts. In 2015, Mao et al.[21] also employed the similar "prestrained polymer" method to create sequentially self-folding structures by 3D printing hinges with digital shape memory polymer (SMP) parts (which would be stretched later) into components. The sequential-folding action is realized by using the difference of time response of the SMP parts with different glass transition temperatures ($T_g s$) (Figure 1.8).

• Hydrogel

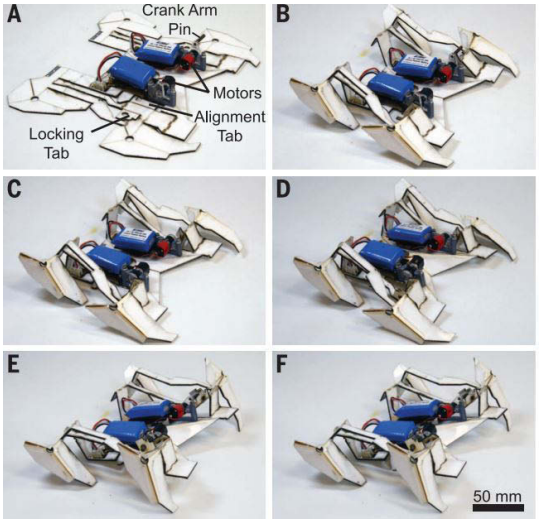

(a)

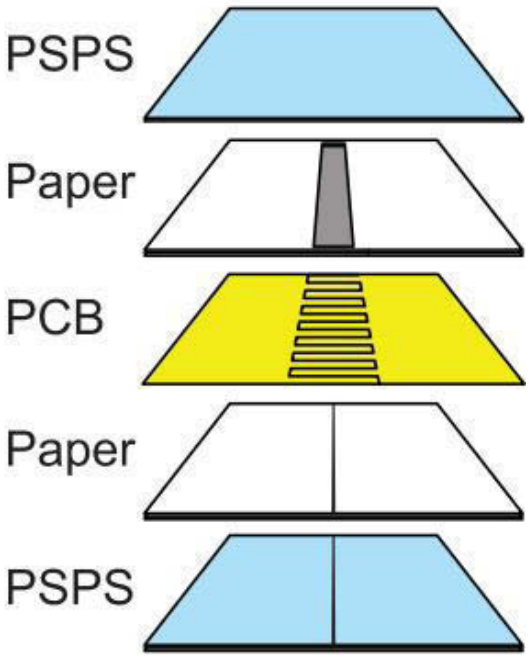

(b)

Figure 1.7: The robot assembles itself in five steps, three of which are self-folding. (A to F) (a) and the self-folding shape-memory composite (b). Reprinted with permission from Reference.[8] ©2014 American Association for the Advancement of Science.

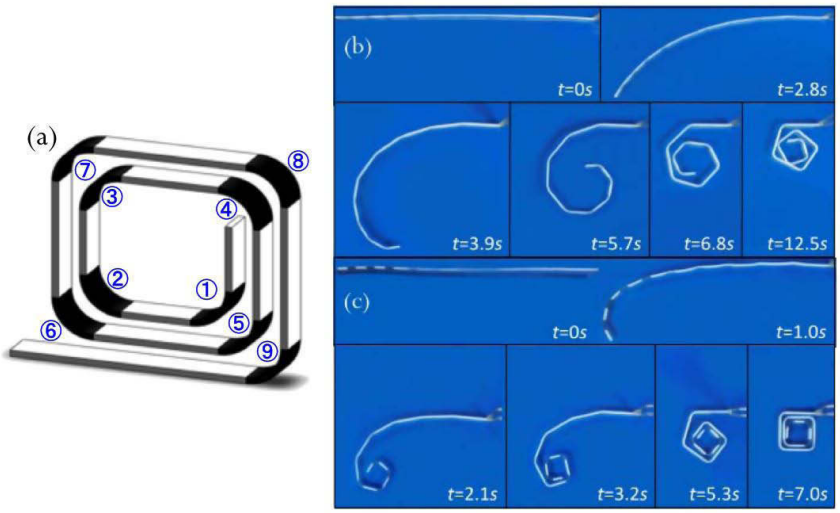

Figure 1.8: The schematic graph of the helical SMP component (a), the black numbered parts are SMPs. Series of photographs showing the shape recovery process of the helical SMP component (b) with uniform hinge sections, and (c) with graded hinge sections. Reprinted with permission from Reference.[21] This article is licensed under a Creative Commons Attribution 4.0 International License.

Hydrogel products constitute a group of polymeric materials, the hydrophilic structure of which renders them capable of holding large amounts of water in their three-dimensional networks. The functional features of an ideal hydrogel material can be listed as follows:[22]

- The highest absorption capacity (maximum equilibrium swelling) in saline.
- Desired rate of absorption (preferred particle size and porosity) depending on the application requirement.
- The highest absorbency under load (AUL).
- The lowest soluble content and residual monomer.

- The lowest price.
- The highest durability and stability in the swelling environment and during the storage.
- The highest biodegradability without formation of toxic species following the degradation.
- Colorlessness, odorlessness, and absolute non-toxic.

Obviously the favorable property of these hydrogels is their ability to swell when put in contact with an aqueous solution. Research on hydrogel-based self-folding actuation was also reported. In 2005, Guan et al.[23] described the fabrication of bilayer hydrogel composites which would fold into 3D structures upon contacting with water due to differential swelling of the two layers (Figure 1.9). While this is a simple and inexpensive approach to realize self-folding, its applicability as an actuator is highly limited due to its miniature scale such that the force it can provide is finite. In addition, fabrication and manipulation face daunting practical challenges in terms of scalability.

• Dielectric Elastomer

In the last decade or so, there has been a great deal of interest in using dielectric elastomer actuators as artificial muscles for soft robotics since dielectric elastomers have similar mechanical properties as human skin-notably a low elastic modulus and a large strain capability-and their actuation can be controlled by the application of

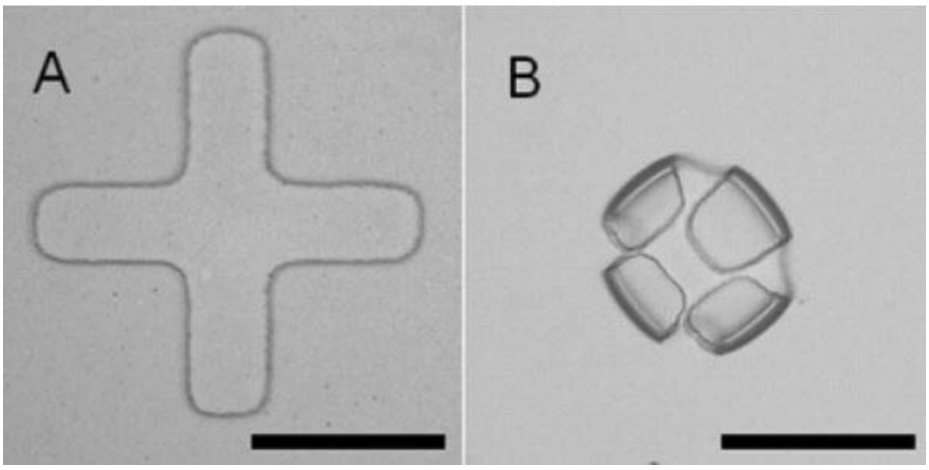

Figure 1.9: Optical micrographs of a cross-shaped microwell (A) and a 3D microstructure (B). Scale bars = 100 μm. Reprinted with permission from Reference.[23] ©2005, American Chemical Society.

an electrical voltage.[24] The detailed description of dielectric elastomer actuation is well established.[25]

In 2015, Shian et al.[26] reported a gripper made by incorporating stiff fibers into voltage-actuated dielectric elastomer beams. The gripper would fold once voltage is applied to dielectric elastomer and unfold without voltage (Figure 1.10). Another work of the application of dielectric elastomer was also described by Shintake et al. in 2016.[27]

As mentioned above, different kinds of actuation mechanisms to realize unidirectional self-folding were introduced. However, the applicability of these actuation mechanisms is greatly restricted mainly by their unidirectional folding property and complex fabrication processes as well as by high energy input, which therefore greatly confines the flexibility of the self-folding structures. Obviously it is necessary to fabricate one actuator that can achieve bidirectional folding action. Here, we define

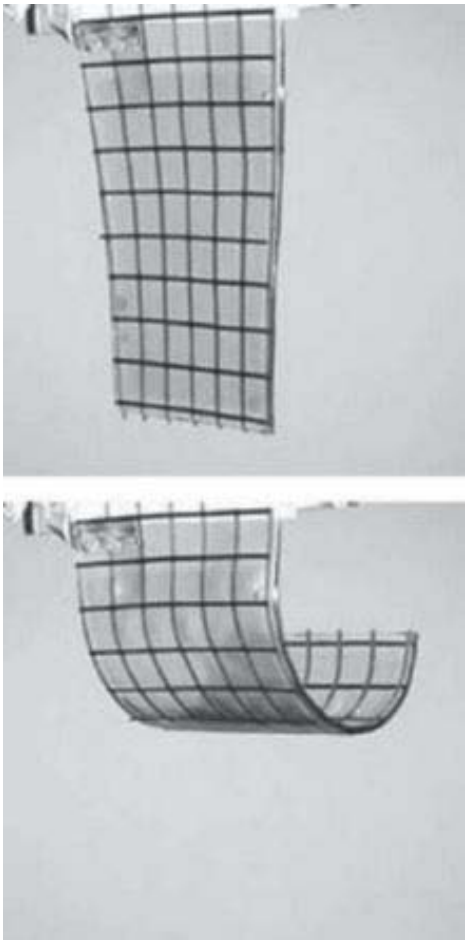

Figure 1.10: *top* The gripper remains vertical without external voltage. *bottom* The gripper folds upon external voltage is applied to dielectric elastomer beam. Reprinted with permission from Reference.[26] ©2015 WILEY-VCH Verlag GmbH & Co. KGaA, Weinheim.

bidirectional folding actuator as the actuator that can produce two opposing folding directions such as upward and downward in a single device.

Here is an example to clarify the definition. Recently, advanced 3D printing technology is used to print active structures, leading to the emergence of four-dimensional (4D) (the 4-th dimension being the time-dependent shape change after the printing) printing[28,29] based self-folding structures. In 2014, Ge et al. applied the 4D printing

concept to the fabrication and design of self-folding structures, where a flat sheet automatically folds into a complicated 3D component.[30] In order to realize that, they printed dynamic composites composed of SMP fibers and an elastomeric matrix, which would fold to the desired angle once the external load is released and recover to a flat shape when ambient temperature is above the glass transition temperature (T_g) of the SMP fibers (Figure 1.11a). The composites would be used as the smart hinges to enable folding patterns. The hinges could realize folding and unfolding in response to temperature change, and thereby the assembly and disassembly of 3D component can be achieved. However, human intervention (external stress) is a must to realize the assembly process (Figure 1.11b), and so strictly speaking, it is not a completely self-folding action. In addition, under the definition of bidirectional folding actuators introduced before, this actuator should still be defined as unidirectional folding actuator since it can only achieve the movement of folding and recovery instead of folding in two opposing directions (e.g. upward and downward).

1.2.2 Bidirectional Folding Actuators

The applicability of the unidirectional actuators introduced above is limited by their uni-directionality. In order to overcome this limitation, people also actively developed actuation mechanisms based on material properties to achieve bidirectional self-folding movement, which would realize more complex 3D structures, multifunctional 3D shapes or assembly plus disassembly without human intervention. At cur-

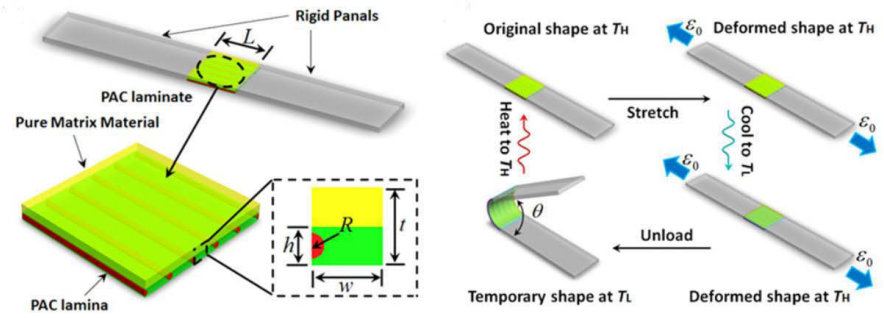

(a)

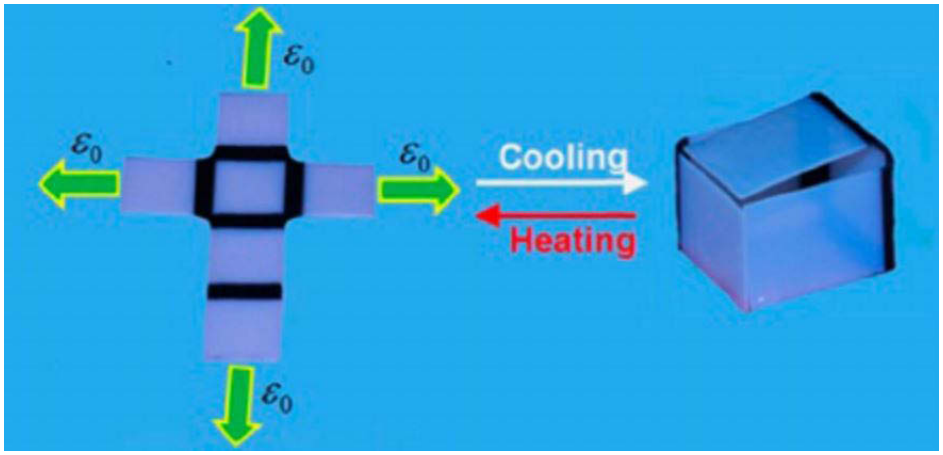

(b)

Figure 1.11: Schematics and the thermomechanical programming steps of the dynamic hinge (a) and the assembly and disassembly processes of a box. Human intervention is a must to provide external load that is necessary for assembly process (b). Reprinted with permission from Reference.[30] ©2014 IOP Publishing, Ltd.

rent stage, most of the mechanisms are based on shape memory effect (SME) so that SMPs and SMAs are usually involved.

However, these SME-based mechanisms also have several limitations (which will be discussed in Chapter 2 in detail), such as need of expensive materials and complex thermomechanical programming processes[31,32] or complex design and fabrication procedures,[33,34] or less degree of controllability.[35] Therefore, it will be beneficial to

develop low-cost and easy-to-fabricate bidirectional actuators with adjustable folding angles.

Those previous work would provide invaluable insight for us to determine all the factors that should be considered during innovative actuator design and fabrication. Based on our research, we will introduce one kind of SMP composite actuator which can realize bidirectional self-folding with adjustable folding angles. Moreover, it has advantage over other bidirectional folding actuators because it is easy-to-fabricate and requires low cost for fabrication. In order to show the practical application of this actuator, in this thesis we would present one robot that could self-fold and transform from 2D sheet into different 3D shapes (boat and car) based on the bidirectional folding ability of the actuator. The robot would be controlled to conduct self-navigation by Arduino during the car state. We also believe the application potential is more than that and therefore worthwhile to be well explored.

1.3 Actuation Methods for Locomotion of Self-folding Structures

In order to accomplish the movement of robot after self-folding from 2D sheet into 3D configuration, we need to figure out suitable actuation method for the robot locomotion and navigation. Robot locomotion is the collective name for the various methods that robots use to move themselves from place to place. People also

get inspirations of novel robot locomotion actuation mechanisms from nature by researching the methods animals adopt to physically interact with different surrounding environments such as terrestrial,[36] aerial,[37] and aquatic environments.[38] However, the number of locomotion mechanisms that are suitable for self-folding structures/robots is limited due to multiple reasons:

- The materials of the robotic base must be stiff and strong enough to ignore the vibration and friction caused by the movement of the robot.
- It needs careful and complex computation of the configuration of the actuators on the 2D base to guarantee the robot can move smoothly after folding into complex 3D architecture since there may exist big difference in positions of actuators before and after folding.
- The self-folding action may interfere the movement of the robot, etc.

So far the published actuation methods for locomotion of self-folding structures/robots have mainly relied on motors and magnetic fields.

Most of the mechanisms for locomotion of self-folding structures are based on motors.[8,39] Miyashita et al.[40] demonstrated a mobile robot which could fold itself and then use two vibration motors (caged by the self-folded outer skeleton for stabilization) for locomotion in 2015 (Figure 1.12). The robot would achieve a translational locomotion speed of 2.95 cm/s and a turning angular speed of 0.74 rad/s. However, the motion of the robot is sensitive to the friction of the ground, and the asymmet-

ric pleat patterns will have an influence on the stability of robot motion. Another challenge for motor-based actuation method is to scale down the size of modules considering the space occupied by actuators. Typically, actuators such as motors contribute more than 50% of the volume and weight of the whole module.[41]

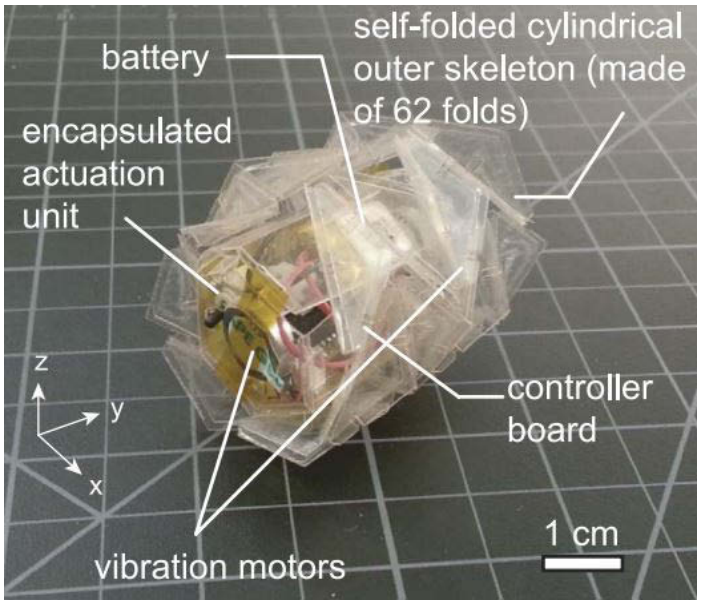

Figure 1.12: View of self-folded outer skeleton with a modularized actuation unit. Reprinted with permission from Reference.[40] ©2015 Massachusetts Institute of Technology.

Although the motor-based method is the most common actuation mechanism for locomotion of self-folding structures/robots. People also introduced innovative method such as magnetic field to realize robot movement. Miyashita et al.[42] in 2015 also presented a novel single-sheet structure that could self-fold into a centimeter-sized mobile robot that subsequently walks and swims driven by an external magnetic field exerted by embedded coils underneath the robot (Figure 1.13). However, the locomotion method is not that practical due to the complex design and fabrication processes

and additional cost introduced by the alternating magnetic filed, etc.

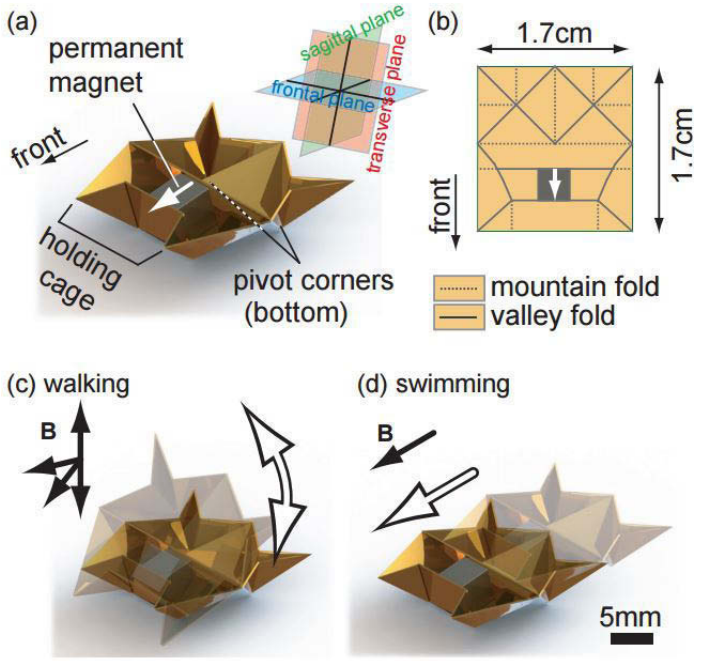

Figure 1.13: The designed mobile robot and the actuation methods. (a) The outlook. (b) The crease pattern. (c) Walking mode by torque-based control. (d) Swimming mode by force-based control. Reprinted with permission from Reference.[42] ©2015 IEEE.

Based on the introduction above, both actuation mechanisms for locomotion of self-folding structures have pros and cons. But considering the fabrication complexity and cost issues, we decided to use motor-based actuation method for locomotion of our self-folding robot.

In addition, there is limited number of work published to explore the functionality of the self-folded macro-scale robots. In order to contribute to that, our robot would conduct self-navigation task such as obstacle avoidance during its car state on the ground by integration of sensor networks and Arduino microcontroller.

1.4 Outline of Thesis

The structure of the thesis is arranged as follows:

The Chapter 2 will introduce different kinds of bidirectional folding actuators developed at current stage for making self-folding structures.

The Chapter 3 will explain the modeling of the actuator and characterize its important properties including folding angle and recovery force via finite element method simulation.

The Chapter 4 and Chapter 5 will describe the detailed fabrication and experimental characterization results of the actuator, including folding angle and recovery force.

The Chapter 6 will present the practical application of the actuator by making a robot that could self-fold from 2D to 3D and transform between different 3D shapes (boat and car) without human intervention. The performance of obstacle avoidance conducted by the robot during its car state would be shown as well.

The Chapter 7 will discuss conclusions and future work of the thesis.

Chapter 2

Mechanisms of Bidirectional Folding Actuators

Bidirectional folding actuators are necessary to overcome the limitations of unidirectional actuators. Thus people actively developed actuation mechanisms achieving bidirectional self-folding movement.

As mentioned briefly in Chapter 1.2.2, bidirectional folding actuation techniques have also been developed to realize self-assembly of multifunctional or highly complex 3D geometries. Most of the developed actuation mechanisms are based on shape memory effect (SME) of SMPs and SMAs. Although using forces derived from material properties (usually happens in thin films) such as swelling,[43,44] shrinkage and capillary force[45] can also realize bidirectional folding or self-assembly/disassembly of complex patterns, the application of using these methods as actuators development

is highly restricted by the small magnitute of the folding force.

2.1 Background: Shape Memory Effect

The shape memory effect (SME) describes the phenomenon of restoring the original shape of a plastically deformed sample by heating it.[46] One-way SME, also known as irreversible SME, denotes the fact that external stimulus would not drive the recovered shape(s) back to the previous temporary shape(s). Multi-SME refers to a shape memory material that is able to memorize more than one temporary shapes and subsequently recovering them in a controllable manner. It is critical to point out that multi-SME also belongs to the one-way SME since the shape changing occurs in only one direction (Figure 2.1). On the contrary, two-way SME can exhibit reversible shape switching between two (or more) distinct shapes.[47] The most typical materials that exhibit SMEs are SMPs and SMAs. However, the SME mechanisms and properties of SMA and SMP are significantly different, which would be described in following section.

2.1.1 Shape Memory Alloy (SMA)

Shape memory alloys (SMAs) are materials that exhibit the ability to memorize shapes through a thermally induced solid state phase transition. Among several industrially developed SMAs (CuZnAl, CuAlNi, NiTi), the most common SMA is

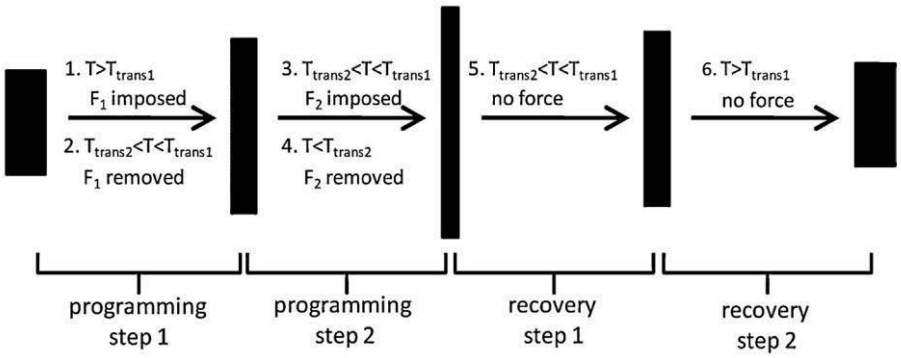

Figure 2.1: Schematic illustration of multi-SME. T_{trans1}, T_{trans2} are temperatures beyond which shape switching between two shapes happens. F_1, F_2 are forces used to program the shape memory material. Reprinted with permission from Reference.[47] ©2015 Elsevier Ltd.

NiTi (Nitinol) alloy used for its ductility and fatigue and corrosion resistance. The SME of SMA is derived from a diffusion-less reversible crystallographic transformation from the high-temperature parent austenite phase to the low-temperature martensite phase.[48] The process can be activated by either stress, temperature or a combination of both,[49] as shown in Figure 2.2. SMA is softer in the martensite phase but stiffer in the austenite phase. SMAs are usually used as actuating devices due to their large recovery stress (150-300 MPa) and reasonable strain recovery up to 8%.[50]

2.1.2 Shape Memory Polymer (SMP)

Shape memory polymers (SMPs) are another kind of materials that can recover their permanent shapes from one (or sometimes multiple) programmed temporary shape(s) in response to an appropriate applied stimulus, such as temperature change, light[51] and chemicals. Most of the existing SMPs fall into three major categories,

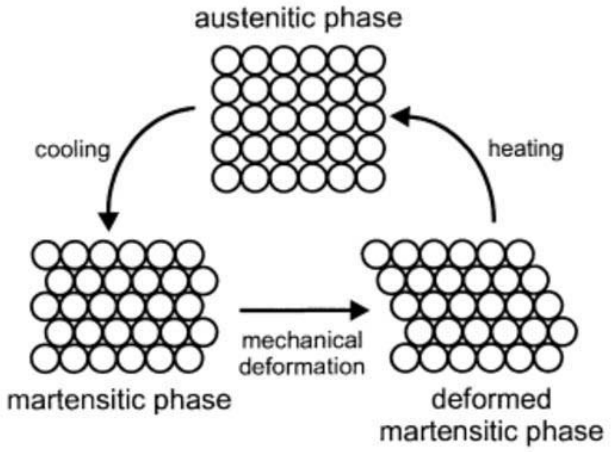

Figure 2.2: Schematic representation of the mechanism of the shape-memory effect for metallic alloys based on a martensitic phase transformation. Reprinted with permission from Reference.[50] ©2002 WILEY-VCH Verlag GmbH, Weinheim, Fed. Rep. of Germany

according to the type of stimuli applied to induce the SME, thermo-responsive SMPs, photo-responsive SMPs and chemo-responsive SMPs.[49]

The SME of SMP is achieved through a specific thermo-mechanical programming process, which usually starts at a temperature higher than a specific transition temperature, T_{trans}, where the SMP is deformed to the desired shape. While holding this deformation constant, the SMP is then cooled below T_{trans}. During the cooling process, the SMP becomes more rigid so that the SMP is able to fix the temporary deformed shape. Glass transition temperature (T_g) is the switching temperature where the polymer transits from stiff glassy state to soft rubbery state.[50] T_{trans} can be either the glass transition temperature or the crystalline melting temperature (T_m) of the polymer.[50] The stiffness of the SMP exhibits a trend opposite to that of the SMA,

where the stiffness is high below T_{trans} and is low above T_{trans}.

During this transition process, the storage modulus of the polymer reduces significantly, as shown in Figure 2.3. Tan Delta, or loss tangent, also shown in Figure 2.3, describes the viscoelastic dissipation characteristic of the polymer. And the peak of the Tan Delta curve represents the key temperature, T_{trans}. SMP has lower recovery stress (1-3 MPa) but exhibits a large amount of recoverable strain, which can be greater than 800%, compared to SMA.[52]

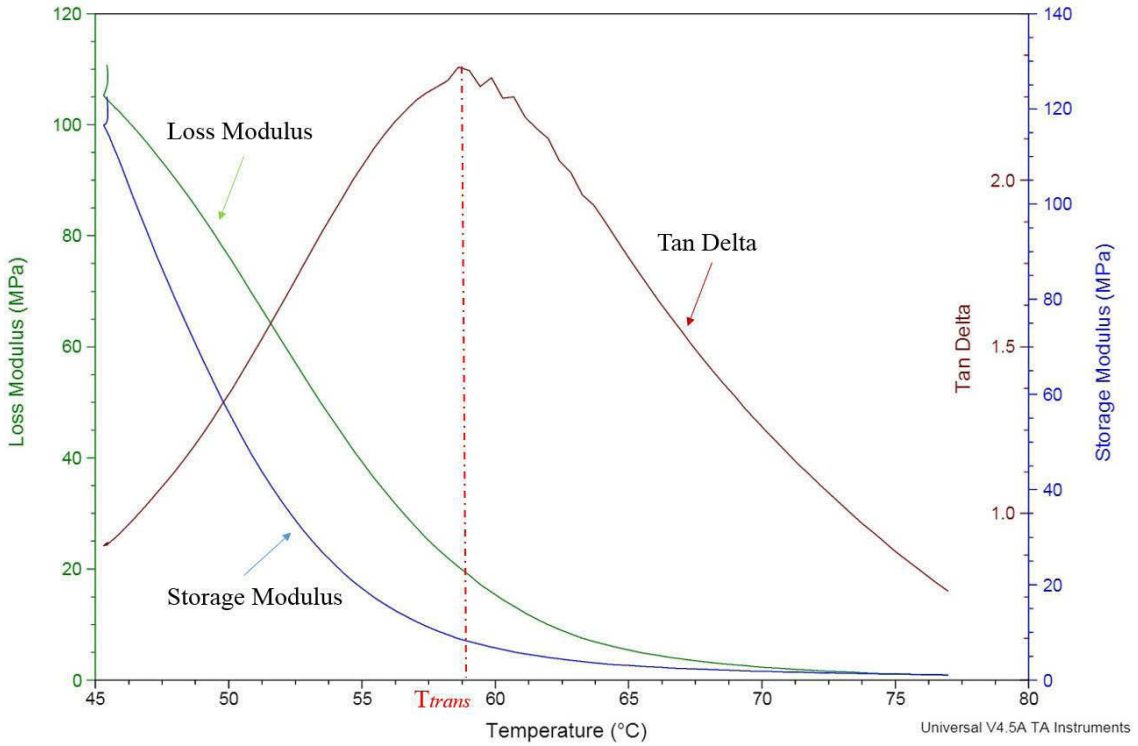

Figure 2.3: Change of storage modulus, loss modulus, and Tan Delta of acrylate-based SMP with temperature increase.

2.2 Bidirectional Folding Actuators

2.2.1 SMA-Based Bidirectional Folding Actuators

As mentioned in Section 1.2.2, people developed bidirectional folding actuators based on SMAs or SMPs, which would be discussed below in detail.

In 2012, Paik et al.[33] presented and characterized a low-profile bidirectional folding actuator based on annealed SMA sheets which could produce two opposing 180° motions derived from the recovery of SMA in response to heat. Figure 2.4 illustrates two modes of the bidirectional actuator where selective heating enables the user to actuate one or two opposing sides simultaneously. In order to overcome the challenge of multiple thermal activation regions in a single actuator, they designed a structure which had two regions thermally isolated from each other so that the SMAs in this two regions could response separately from each other to produce bidirectional motions. To activate the folding action, a laser-patterned nickel alloy heater is also developed to localize the actuation area (Figure 2.5) as well as to create selective heating that allowed the actuator to produce two distinct torques within a single actuator. The actuator is suitable for use in self-folding based robot due to its thin ($\leq$ 1 mm) and compact profile, and bidirectional rotational motions. In addition, the actuator also shares the advantages of SMA: high strain, silent operation, and mechanical simplicity. However, it needs complex design considerations and fabrication processes to successfully make this kind of bidirectional SMA actuator, and additional cost is

introduced by the fabrication and design of the heater.

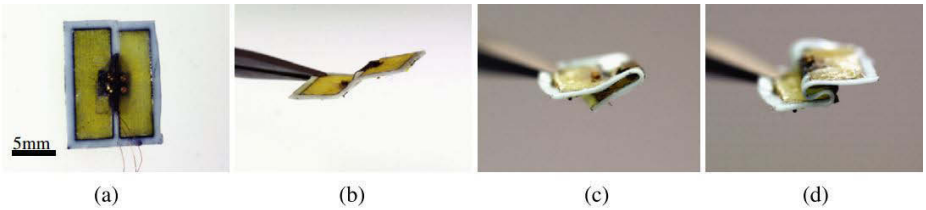

Figure 2.4: Bidirectional folding movement of the actuator: before activation (a) and (b), single axis activated (c) and both axes activated (d). Reprinted with permission from Reference.[33] ©2012 IOP Publishing Ltd.

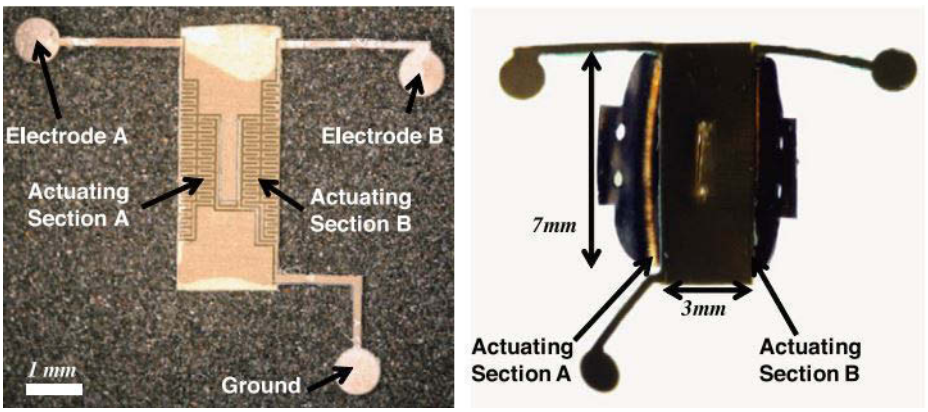

Figure 2.5: Inconel heater with an SMA actuator. Patterned Inconel heater with three electrodes, before (a) and after (b) mounting to an actuator. Reprinted with permission from Reference.[33] ©2012 IOP Publishing Ltd.

2.2.2 SMP-Based Bidirectional Folding Actuators

As discussed in 2.1, there exists one-way and two-way SMEs. The difference is whether the actuation is reversible or not. In the first case, the transition from the temporary shapes to memorized (permanent) shapes is not reversible by just reversing the external stimulus. One additional training step is necessary to realize the temporary shape again after recovery. In the second case, the transition from temporary

shapes to permanent shapes is reversible by simply reversing the external stimulus. Both of the SMEs are utilized to achieve bidirectional folding actuators[35,49,53] and will be introduced as follows.

In 2013, Ge et al.[34] reported a free-standing actuator composed of a trained (pre-strained) SMP strip embedded into an elastomeric matrix (PEGDMA/tBA), as shown in Figure 2.6a. The bidirectional folding action is realized by combination of the shape memory effect (SME) and different expansion extents of the SMP strip and the matrix once heated. At the early stage of heating, before the SME starts, the actuator will bend to the direction as shown in Figure 2.6b-(B) due to the different expansion extents of the SMP and the matrix. The effective coefficient of thermal expansion (CTE) of the SMP is higher than that of the matrix material so that the SMP strip expands more than the matrix material. Once the SME starts when the temperature is high enough, the SMP strip will contract due to the SME so that the actuator will bend to another direction, as shown in Figure 2.6b-(C). The authors also created an analytical model to successfully predict the performance of the actuator and help to have a better knowledge of the underlying phenomena during the actuation process. However, the fabrication process is complex due to the embedding of the SMP strip into the matrix.

In the previous paragraphs, we introduced different bidirectional folding actuators based on SMAs or SMPs. Both of the methods have their pros and cons. For SMPs, they are easier to be programmed, light weight, low cost, have large degree of flexibil-

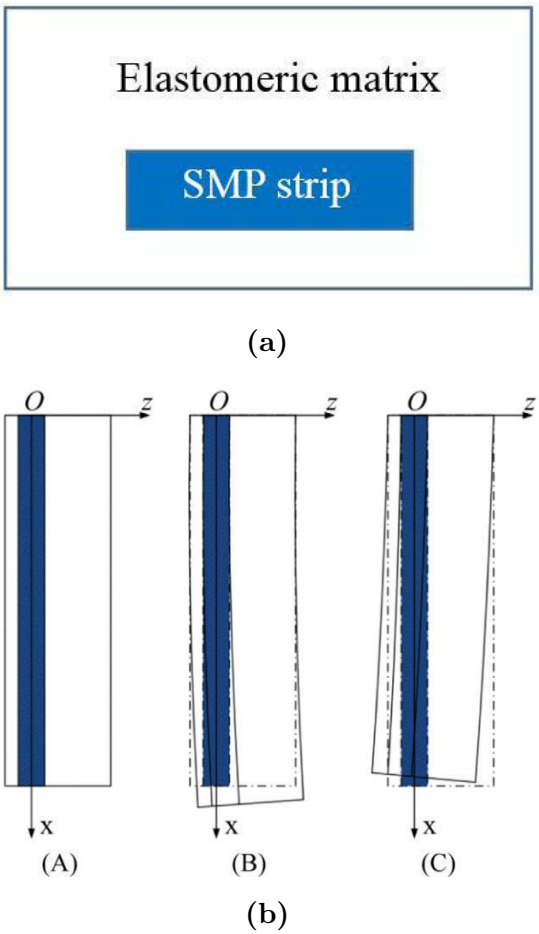

Figure 2.6: The cross section of the actuator (The blue part is the SMP strip, the white part is the matrix) (a) and the schematics of the actuation process of the actuator. (blue strip inside is the SMP strip and the white part around is the matrix): (A) original position of the actuator; (B) when the SMP strip expands more than the matrix, it is defined that the actuator bends in the negative direction; (C) as the SMP strip contracts due to the shape memory effect, it is defined that the actuator bends in the positive direction (b). Reprinted with permission from Reference.[34] ©2013 IOP Publishing Ltd.

ity in material design but the recovery stress and fatigue strength are less than those of SMAs. And the response time of SMPs is often longer than that of SMAs. Also, they lack some particular properties that prevent them from wider range of application such as good electric conductivity. In order to improve the performance or com-

pensate the disadvantages of SMPs, people also developed shape memory polymer composites (SMPCs), such as SMP-co-SMP, SMP-co-SMA,[49] SMP-co-CNTs, fiber reinforced SMP,[54] etc., which presented higher recovery stress or improved electric conductivity than pure SMPs. On the contrary, SMAs can provide larger recovery stress than SMPs but they are more expensive and complex to program. Detailed comparison of the properties of SMPs with SMAs is summarized in Table 2.1.[55]

2.3 Our Innovative Bidirectional Actuators

The universal application of the actuators described above is restricted by different drawbacks. In this thesis, we will report an innovative bidirectional folding SMPC actuator, which is composed of two layers of different SMPs (with different $T_g s$) with an angled permanent shape as shown in Figure 2.7b. Our actuator would realize bidirectional folding with adjustable folding angles θ_1 and θ_2, (defined in Figure 5.13) in response to temperature change. It has advantage over other bidirectional folding actuators in that it is easy to fabricate and program as well as it is low cost.

Each SMP layer of our SMPC can be synthesized by curing the mixture of monomer tert-Butyl acrylate (tBA) and crosslinker poly(ethylene glycol) dimethacrylate (PEGDMA) under UV light (cured in UVP, CL1000). The glass transition temperature of synthesized SMP can be controlled by changing the mass ratio between the monomers

Properties	SMP	SMA
Density (g cm^{-3})	$0.9 \sim 1.1$	$6 \sim 8$
Extent of Deformation	Up to 800%	<8%
Young's Modulus at $T<T_{trans}$/GPa	$0.01 \sim 3$	83 (NiTi)
Young's Modulus at $T>T_{trans}$/GPa	$(0.1 \sim 10) \times 10^{-3}$	$28 \sim 41$
Stress Required for Deformation/MPa	$1 \sim 3$	$50 \sim 200$
Stress Generated During Recovery/MPa	$1 \sim 3$	$150 \sim 300$
Transition Temperatures/°C	-10 ~ 100	-10 ~ 100
Recovery Speeds	<1 s ~ several min.	<1 s
Thermal Conductivity/W $m^{-1}K^{-1}$	$0.15 \sim 0.30$	18 (NiTi)
Programming Conditions	<200°C, low pressure	>1000°C and high pressure required
Cost	<$10 per lb	~ $250 per lb

Table 2.1: Comparison of the properties of SMPs with SMAs. Reprinted with permission from Reference.[55] ©2007 Royal Society of Chemistry.

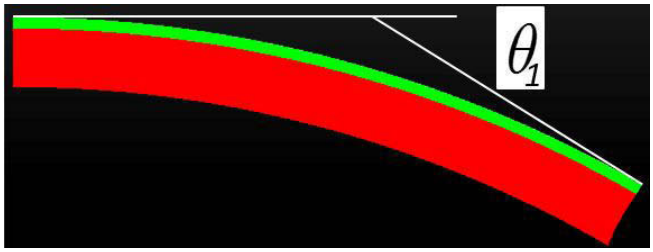

(a)

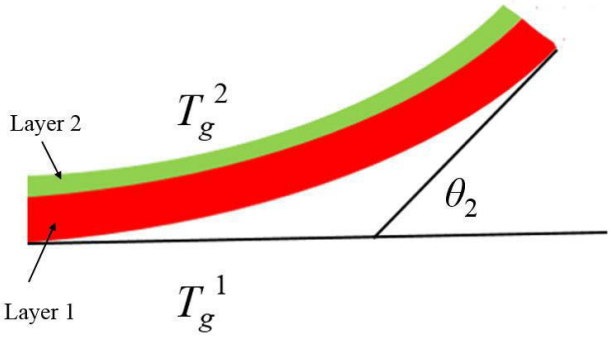

(b)

Figure 2.7: Schematic and the definition of the folding angles. Fold downward. θ_1 is the non-predetermined folding angle (a) and schematic of the permanent shape of our bidirectional folding actuator. The actuator is composed of two layers of SMPs with different Tgs and has an angled permanent shape. θ_2 is the predetermined folding angle (b).

and crosslinkers. The bilayer structure can be achieved by synthesizing the second layer of SMP on top of the first layer of SMP in a mold and the angled permanent shape can be realized by using a clamp to fix the desired angled shape during cure process in oven under high temperature. Then, the SMP composite is programmed by stretching to desired extent under a temperature above T_g^1. The detailed fabrication and programming processes will be described and visualized in Chapter 4.

The actuator is activated once the ambient temperature is over the T_g of the SMP and can realize bidirectional folding movement in a single device as shown in Figure

2.8. At first, we need to program the actuator by stretching it to some extent at the temperature T_H which is higher than both of the $T_g s$ (T_g^1 and T_g^2), then we cool down to T_L which is lower than both of the $T_g s$ so that the temporary shape can be fixed. If we increase the ambient temperature to T_C which is higher than T_g^1 but lower than T_g^2, due to the shape memory effect, the bottom SMP layer tends to recover the permanent shape (by shrinking) but the top layer tends to keep the temporary shape (T_C is lower than T_g^2) so that the strain mismatch is produced, causing the actuator folding downward. If the ambient temperature continues increasing to the temperature which is higher than both of the $T_g s$, both layers of SMPs recover the permanent shapes and the actuator would fold upward. Actually there exists partial recovery, meaning the SME would start when the temperature is still lower than but near T_g of shape memory material. Considering that, the difference between the $T_g s$ should be big enough (T_g^2-$T_g^1 \geq 10°$C) to produce enough strain mismatch.

Then in order to have a clear knowledge of the ability and the application area of the actuator, we need to characterize it, including stress-strain curve, storage modulus, etc. Two of the most important properties of the actuator will be the maximum recovery force it can provide and the maximum folding angle it can reach. We care more about the maximum angle θ_1 (Figure 2.7a) when folding downward since θ_2 (Figure 2.7b) is predetermined from the permanent shape. These two properties depend on two parameters-the prestrain determined by the programming process and the thickness ratio between the two layers.

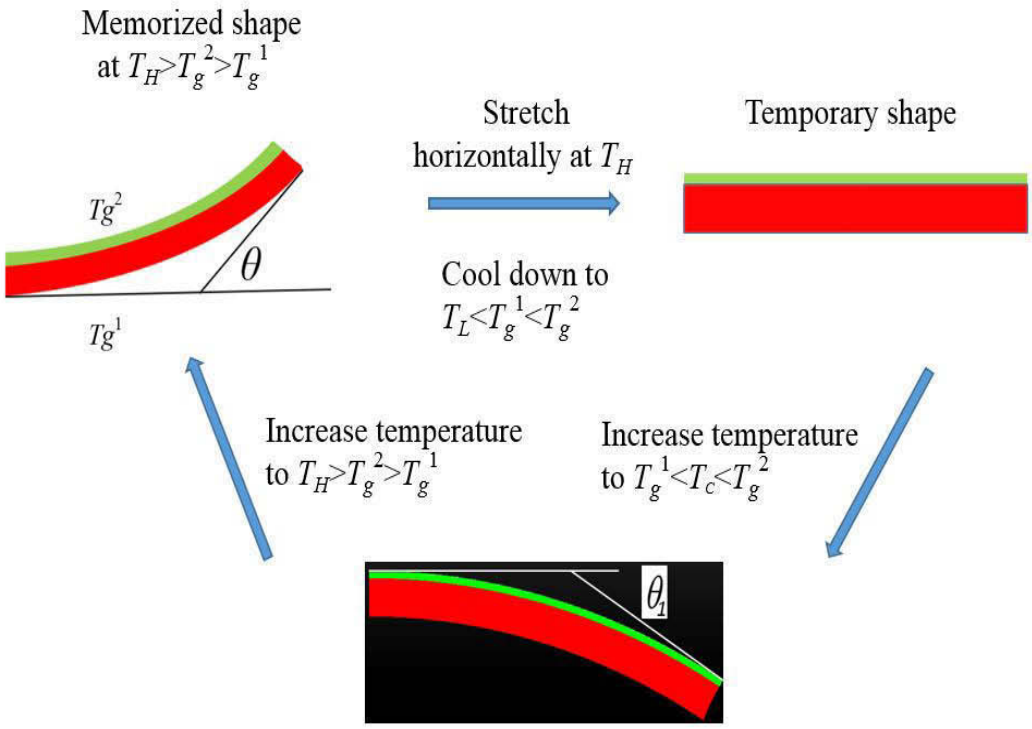

Figure 2.8: Schematic of the bidirectional folding movement of the actuator.

This hypothesis is derived from the following strain energy theory of curved cantilever beam. Consider the process that the programmed actuator folds downward and reaches its maximum folding angle (shown in Figure 2.9). Here, we regard the bilayer SMP composite as a cantilever beam and we assume the material has a linear elastic behavior, also we assume that the displacement is small and the only energy form of the system is strain energy. There is no energy loss and Young's modulus remains constant during the whole folding process. Then we can get the following relations.

If we consider the stretch process from state 1 to state 2 (which happens at T_H,

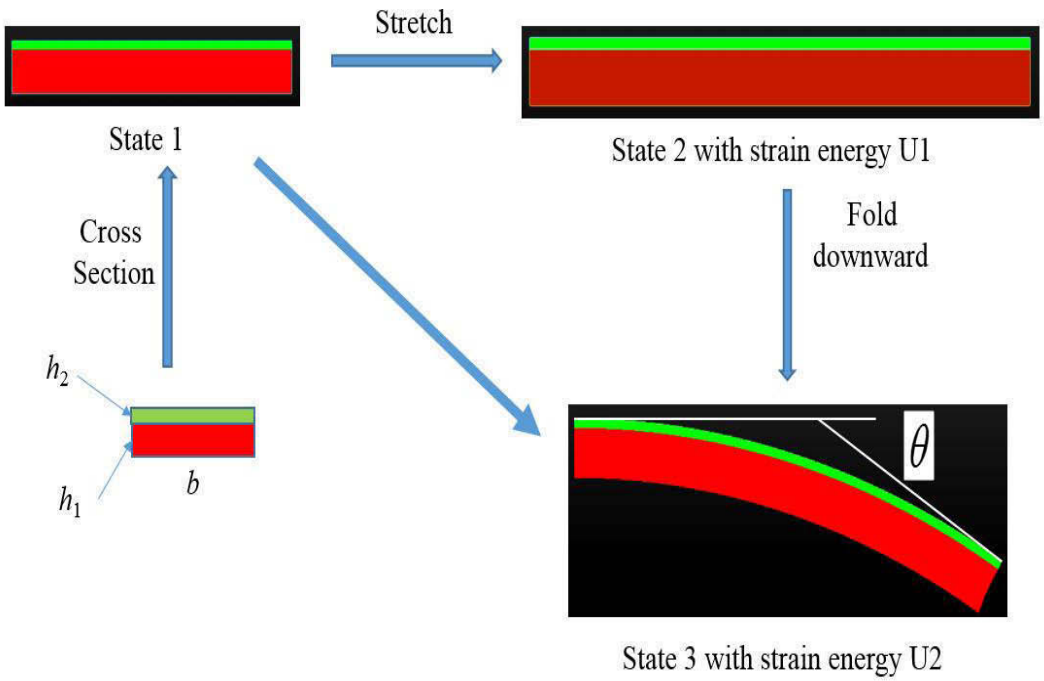

Figure 2.9: Schematic of the process used to derive the folding angle equation. The thicknesses of top and bottom layers are h_2 and h_1, respectively. The width of both layers is b.

here we set it to 65°C), since we regard it as one linear elastic model, we can calculate the strain energy of the system (U_1) from a linear elasticity theory:[56]

$$U_1 = \frac{1}{2}(k_1 + k_2)\Delta x^2 \tag{2.1}$$

where k_1 and k_2 are spring constants of the elastic model, Δx is the elongation of the model due to prestretch. Then, we have the following relations:

$$k_1 = \frac{E_1^H S_1}{L} \qquad k_2 = \frac{E_2^H S_2}{L} \qquad S_1 = h_1 b \qquad S_2 = h_2 b \qquad \Delta x = L\varepsilon \tag{2.2}$$

E_1^H and E_2^H are Young's modulus of the bottom and top SMP layers at 65°C, respectively. ε is the prestrain and L is the original length of both layers. S_1 and S_2 are the cross section area of each layer (as shown in Figure 2.9).

By substituting the above expressions into equation 2.1, we have:

$$U_1 = \frac{b(E_1^H h_1 + E_2^H h_2)}{2} L\varepsilon^2 \tag{2.3}$$

Now we assume the cantilever beam in pure bending by couples of moment M (which is constant along the beam) and rotation is small at the state 3. Also, the normal stress varies linearly from the neutral axis. Then, the stored strain energy of one bending cantilever beam (U) can be written as:[56]

$$U = \frac{M^2 L}{2EI}$$

By substituting $\theta = \frac{ML}{EI}$, we get:

$$U = \frac{\theta^2 EI}{2L}$$

So at the state 3 (which happens at T_C, here we set it to 54°C), the total stored strain energy of the bilayer SMP (U_2)can be described as:

$$U_2 = \frac{\theta^2 E_1^C I_1}{2L} + \frac{\theta^2 E_2^C I_2}{2L} \tag{2.4}$$

where I_1, I_2 are moment of inertia of each layer, and E_1^C and E_2^C are Young's modulus of the bottom and top SMP layers at 54°C, respectively. We also have following relations:

$$I_1 = \frac{bh_1^3}{12} \qquad I_2 = \frac{bh_2^3}{12} \tag{2.5}$$

By substitute the two equations above into equation 2.4, we can get:

$$U_2 = \frac{\theta^2 E_1^C b h_1^3}{24L} + \frac{\theta^2 E_2^C b h_2^3}{24L} \tag{2.6}$$

As we assumed there is no loss of stored strain energy of the system (strain energy conservation), we can get $U_1 = U_2$. Then we can get an expression for θ as equation 2.7:

$$\theta = \sqrt{\frac{12(E_1^H + E_2^H \eta)}{h_1^2(E_1^C + E_2^C \eta^3)}} L\varepsilon \tag{2.7}$$

where $\eta = \frac{h_2}{h_1}$ is the thickness ratio between two layers. For our experimental condition, we set $0<\eta<1$.

From equation 2.7, we can see that the maximum folding angle (θ, shown in Figure 2.9) is only related to the prestrain ε and thickness ratio η under the condition that the Young's modulus, the original length L and the thickness of the bottom layer

h_1 remain constant. In order to visualize the relation among angle, prestrain and thickness ratio, for typical experimental conditions we set $L = 18$ mm, $h_1 = 2$ mm, η ranges from 0.1 to 0.5 and ε ranges from 0.1 to 0.3. We can measure Young's modulus E_1^H, E_2^H, E_1^C and E_2^C using the TA Q800 Dynamic Mechanical Analyzer (DMA) as 7.35 MPa, 12.27 MPa, 51.19 MPa and 138.06 MPa, respectively. Then, we can plot the 3D plot of the folding angle as shown in Figure 2.10.

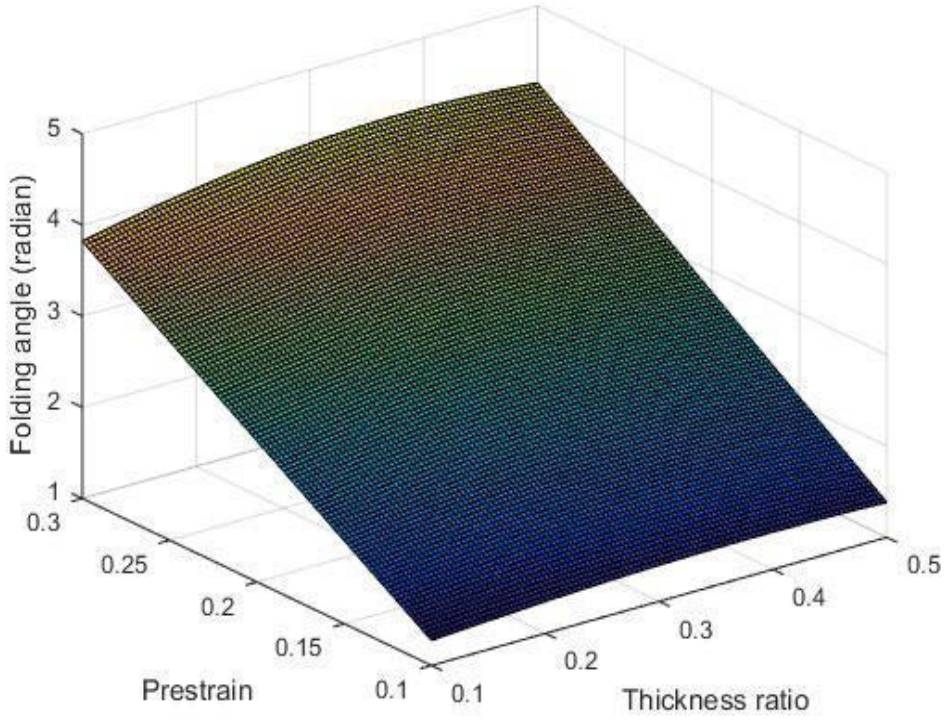

Figure 2.10: Folding angle as a function of prestrain and thickness ratio. For this specific case, we set $L = 18$ mm, $h_1 = 2$ mm, η ranges from 0.1 to 0.5 and ε ranges from 0.1 to 0.3. E_1^H, E_2^H, E_1^C and E_2^C are 7.35 MPa, 12.27 MPa, 51.19 MPa and 138.06 MPa, measured by DMA.

From the figure and equation, we can easily conclude that the maximum folding angle depends on prestrain (ε) as well as thickness ratio (η) and the folding angle will

increase with the increase of ε.

We still adopted the parameter values mentioned above and plotted Figure 2.11 to visualize the relation between the maximum folding angle θ and thickness ratio η ($0.1<\eta<0.5$) for a fixed prestrain value. From the figure, we can have a clear understanding of the relation between θ and η.

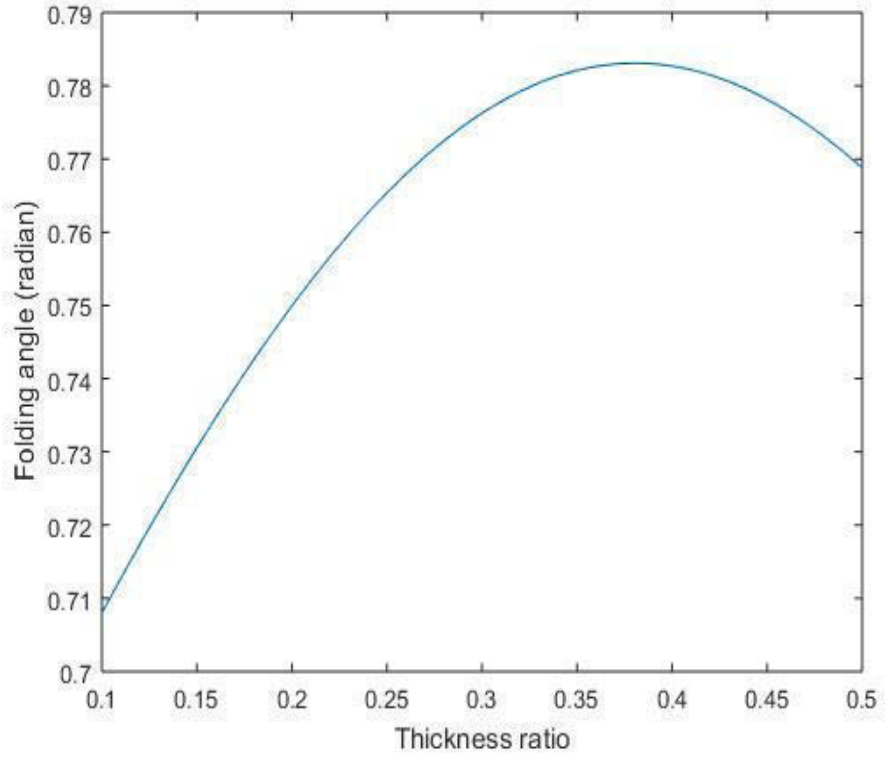

Figure 2.11: Folding angle as a function of thickness ratio (η) with fixed prestrain. For this specific case, we set $h_1 = 2$ mm, η ranges from 0.1 to 0.5. E_1^H, E_2^H, E_1^C and E_2^C are 7.35 MPa, 12.27 MPa, 51.19 MPa and 138.06 MPa, measured by DMA.

In terms of the recovery force, we can get inspiration from the deflected cantilever beam subject to concentrated load. We know that for a cantilever beam subject to concentrated load P at the free end (Figure 2.12), the relation between the folding

angle θ and P can be written as:

$$\theta = \frac{Pl^2}{2EI} \tag{2.8}$$

where E, l and I are the Young's modulus, the original length and the moment of inertia of the beam, respectively. θ is the folding angle of the beam and its definition agrees with the one we made in 2.7a.

From equation 2.8, we can see that the load P is positively proportional to the folding angle θ, which helps us to make the hypothesis that the recovery force is positively correlated to the folding angle so that the prestrain and thickness ratio will have similar influence on recovery force as they have on folding angle.

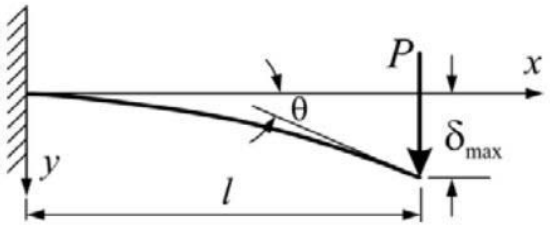

Figure 2.12: One cantilever beam subject to concentrated load P at the free end. l is the original length of the beam, θ is the folding angle and δ_{max} is the maximum deflection at the free end.

The above derivations are only rough estimates since the system should not be isolated thus will interact with external energy, and the stored strain energy may lose partially due to partial recovery. Also, the SMP is viscoelastic material and should not be seen as a linear elastic model. However, the relation among thickness ratio, prestrain and folding angle could give us a hint of the factors affecting the final folding

angle and recovery force thus guide our simulation and experiment.

The equations 2.7 and 2.8 can be regarded as the guidance and used to explain why we care about the two parameters-prestrain and thickness ratio-and give us some sense of how to adjust the magnitute of the folding angle by controlling the two parameters. The detailed characterization processes in simulation and experiment will be discussed in Chapters 3 and 5, respectively.

2.4 Conclusion of the Chapter

In the first part of this chapter, we described different bidirectional folding actuators based on shape memory effects. The applications of these actuators are limited due to various factors such as complex fabrication and programming processes. In order to address these issues, we come up with one novel SMPC actuator that can realize bidirectional folding movement with adjustable angles. The fabrication and programming processes are simple and details will be described in the following chapters. Through strain energy analysis during actuation, we found that the two important properties of the actuator (the maximum non-predetermined folding angle θ shown in Figure 2.9 and corresponding maximum recovery force) depend on prestrain and the thickness ratio between the two SMP layers. We will validate the analytical expression by finite element method simulation in Chapter 3 and experiment in Chapter 5, respectively.

Chapter 3

The Modeling of Bidirectional Folding Actuators

In this chapter we modeled the folding process of the bilayer shape memory polymer composite and output the values of folding angle and recovery force in *Tahoe* to investigate the relation among the maximum non-predetermined folding angle and corresponding maximum recovery force of the actuator, and the prestrain (ε) and the thickness ratio (η) between the two SMP layers.

Since we cared more about the non-predetermined folding angle and the corresponding recovery force, here we simulated the process of folding to the maximum non-predetermined folding angle only. We will use the model developed by Profs. Xiao and Nguyen in 2013,[57] which will be briefly introduced in this chapter.

3.1 Overview of the Model

We used the thermomechanical constitutive model developed by Xiao et al.[57] to model the performance of SMPC actuator in response to temperature change. The model focused on time-dependent behaviors of the glass transition of amorphous networks and used multiple discrete relaxation processes to describe the distribution of relaxation times for structural relaxation, stress relaxation, and stress-activated viscous flow. They introduced a non-equilibrium thermodynamic framework to demonstrate the thermodynamic consistency of the constitutive theory. The theoretical foundation of the model was described by Nguyen et al.[58] in detail. The model could be applied to study the effects of deformation temperatures and physical aging on the shape-memory behavior of amorphous networks. Altogether, the model demonstrates that an understanding of the time-dependent behaviors of the glass transition can be used to tailor the temperature and deformation history of the shape-memory programming process.

3.2 Modeling Methods

The modeling process is composed of three steps: the creation of the geometric model, the thermomechanical programming process and the recovery process.

3.2.1 Geometric Model Creation

Here, we consider the bilayer SMPC structure as one 2D cantilever beam composed of two layers rectangles merged together. In order to comply with the realistic dimensions of the experimental testing samples in Chapter 5 (the length of stretched part is 18 mm and the thickness of the bottom layer is 2 mm), here, we created the cantilever beam with length of 180 units and the height of bottom layer rectangle 20 units length by *Cubit*. Then we can get the desired thickness ratio by adjusting the height of the top layer. Next we meshed the model and set nodesets which would help to set boundary conditions and get desired output values. Figure 3.1 illustrates two meshed geometric models with thickness ratios 0.2 and 0.5, respectively. We set 6 nodesets for each model.

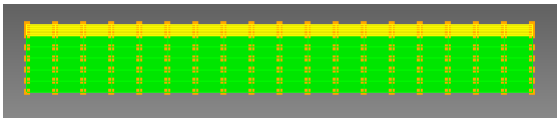

(a)

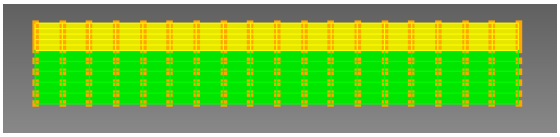

(b)

Figure 3.1: The meshed geometric model of bilayer SMPs with thickness ratio 0.2 (a) and the meshed geometric model of bilayer SMPs with thickness ratio 0.5 (b). The yellow block is the top layer and the green block is the bottom layer.

3.2.2 Thermomechanical Programming Process

In the thermomechanical programming process, we can apply the desired prestrain to the model. The detailed procedure is described as follows:

First, at $t = 0$ s, we set ambient temperature T to 76°C, which is higher than $T_g s$ of two SMP layers ($T_g^1 = 47$°C and $T_g^2 = 60$°C in our case). And maintained the temperature for a while to make sure the model could be heated completely (here we chose 20 seconds). Then, we fixed the left side of the geometric model, corresponding to one nodeset we set in geometric model creation step, as shown in Figure 3.2a.

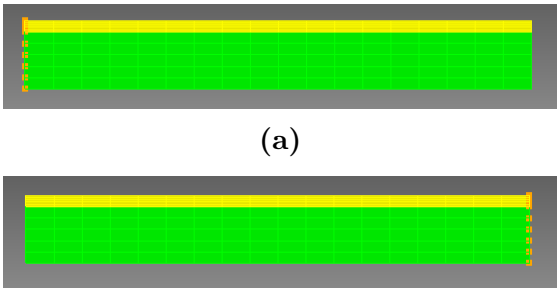

(a)

(b)

Figure 3.2: Boundary condition of thermomechanical programming step: the left side of the model is fixed during programming process (a) and the prestrain step: move the right side of the model to obtain desired prestrain value (b). The yellow block is the top layer and the green block is the bottom layer.

And under this temperature, we moved the right side of the model horizontally to some displacement value, corresponding to another nodeset (Figure 3.2b), to obtain the specific prestrain we desired. Next we slowly cooled down to 16°C (lower than both $T_g s$) at $t = 200$ s linearly and keep the temperature for 120 seconds, during which the position of the right side was fixed so that the SMPC could fix one temporary

shape. The detailed programming parameters are listed in Table 3.1 to obtain 10% prestrain.

Time t (s)	Temperature T (°C)	Prestrain ε (%)
0	76	0
20	76	10
200	16	10
320	16	10

Table 3.1: Detailed parameter values for thermomechanical programming process to get 10% prestrain.

We can check the result of the thermomechanical programming from the coordinate change of the point on the top right corner of the model. As we mentioned in Section 2.3 that for typical experimental conditions η and ε range from 0.1 to 0.5. So for the following example, the thickness ratio is set to 0.2 (the heights of the top and bottom layers are 4 and 20) and prestrain is 10% (stretched by 18 units length, relevant to the original length 180 units length). Then, we check the coordinate change as a function of time for the point with coordinate (180, 24) (units length) as shown in Figure 3.3:

From the figure 3.3, we can see that the coordinate change in x direction is 18 at $t = 320$ s. The negative coordinate change in y direction indicates the shrinkage due to the positive Possion ratio of the material. The result indicates successful prestrain (10%) storage inside the geometric model after the thermomechanical programming process.

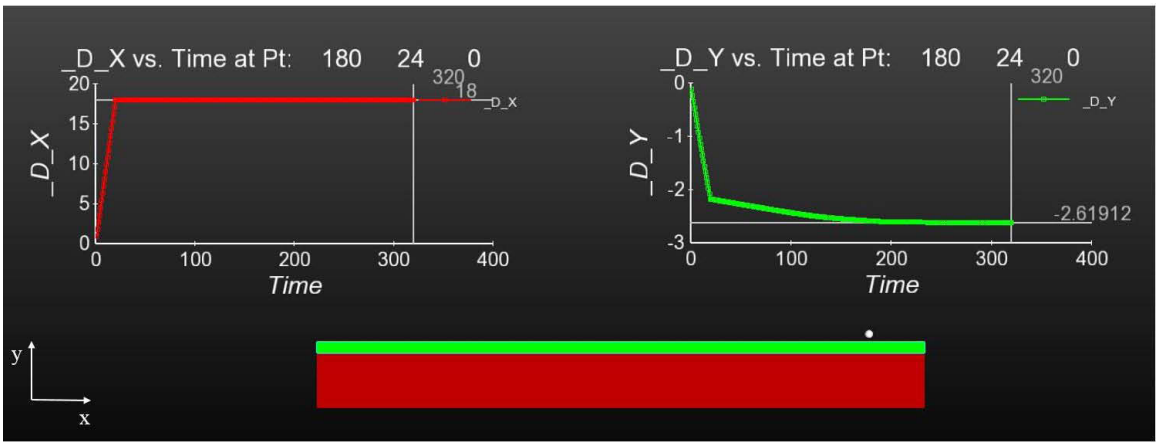

Figure 3.3: Coordinate change in x and y directions of the point on the top right corner of the model. The unit of x axis is second, and the unit of y axis is unit length. The green block is the top layer and the red block is the bottom layer.

3.2.3 Recovery Process

After the programming procedure, we would apply a recovery process to estimate the maximum non-predetermined folding angle and recovery force described as follows:

At $t = 320$ s, we started to slowly increase ambient temperature from 16°C to a temperature higher than the lower T_g with a rate of 2.88°C/min and kept the temperature for over 600 seconds to guarantee that the maximum non-predetermined folding angle can be reached. And during the recovery process, the left side of the model remain fixed.

3.3 Folding and Unfolding in Simulation

Here we show the whole folding and unfolding process of bilayer SMPs with thickness ratio 0.2 and prestrain 30% in finite element method (FEM) simulation as shown in Figure 3.4. The case corresponds to the definition of one directional folding actuators instead of bidirectional folding actuators, as mentioned in Section 1.2.1.

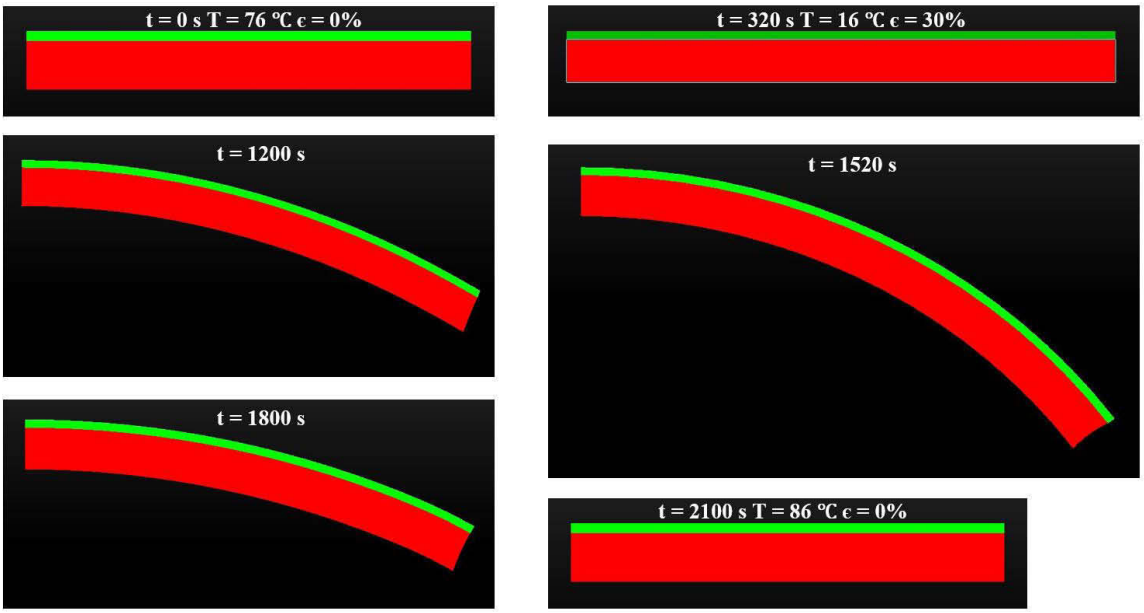

Figure 3.4: Folding and unfolding process of bilayer SMPs in FEM simulation.

From the simulation, we can clearly understand the folding/unfolding process of the SMPC actuator. The actuator will start folding once the ambient temperature reaches T_g^1 and continue folding to reach the maximum folding angle given enough time. Then, the SMP will start unfolding once the ambient temperature reaches T_g^2. Finally, the SMPC actuator will go back to the initial flat configuration without any stored prestrain inside as the ambient temperature reaches 86°C.

3.4 Modeling Results

In this section, we would output the maximum non-predetermined folding angle and corresponding recovery force values to validate the hypothesis we made in Chapter 2.

3.4.1 Recovery Force

3.4.1.1 Calculation Method

We conducted the block force measurement via FEM simulation to output the maximum recovery force of the model during the folding and unfolding process as described in Section 3.3. Here we will monitor the recovery force of the nodeset at the end of the bottom surface and use this force to approximate the recovery force of the model.

We used the geometric model with original length 180 units, thickness ratio 0.2 and prestrain 10% as an example. And in order to monitor the recovery force of the nodeset (with coordinate (180, 0)) at the end of the bottom surface (as shown in Figure 3.5a), we put an infinite horizontal wall with x coordinate 0 to restrict the movement of the model in y direction. Then by outputting the force (unit: 0.01 N) applied to the nodeset by the wall (Figure 3.5b), we can indirectly measure the maximum recovery force of the nodeset during the folding and unfolding process, in this case $0.51 \times 10^{-2} N$.

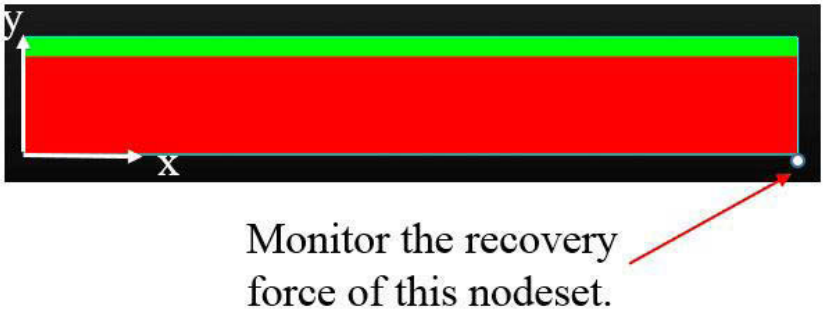

(a)

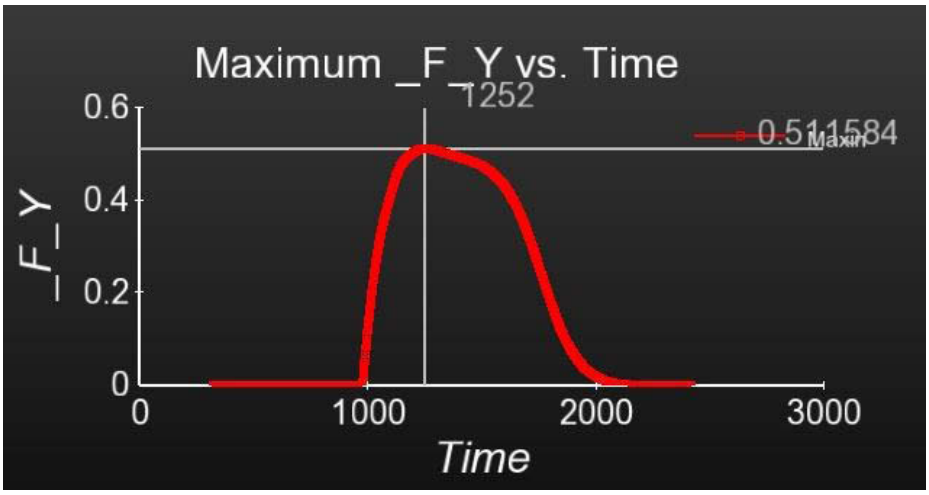

(b)

Figure 3.5: We monitored the recovery force of the nodeset with coordinate (180, 0) during the folding and unfolding process. The nodeset with coordinate (180, 0) at the end of the bottom surface (a) and simulation results tracking the recovery force of the nodeset with coordinate (180, 0) on the bottom as a function of time (Unit of y: 0.01 N; unit of x: second) (b).

3.4.1.2 Result

By using the above method, we output a series of maximum recovery force in Newton (N) and plotted versus prestrain with thickness ratios η=0.2 and 0.5 in Figure 3.6 by *R Studio*. The data follow a trend of increasing maximum recovery force with

the increase of thickness ratio (η) and prestrain (ε), which agrees with the hypothesis we made in Section 2.3.

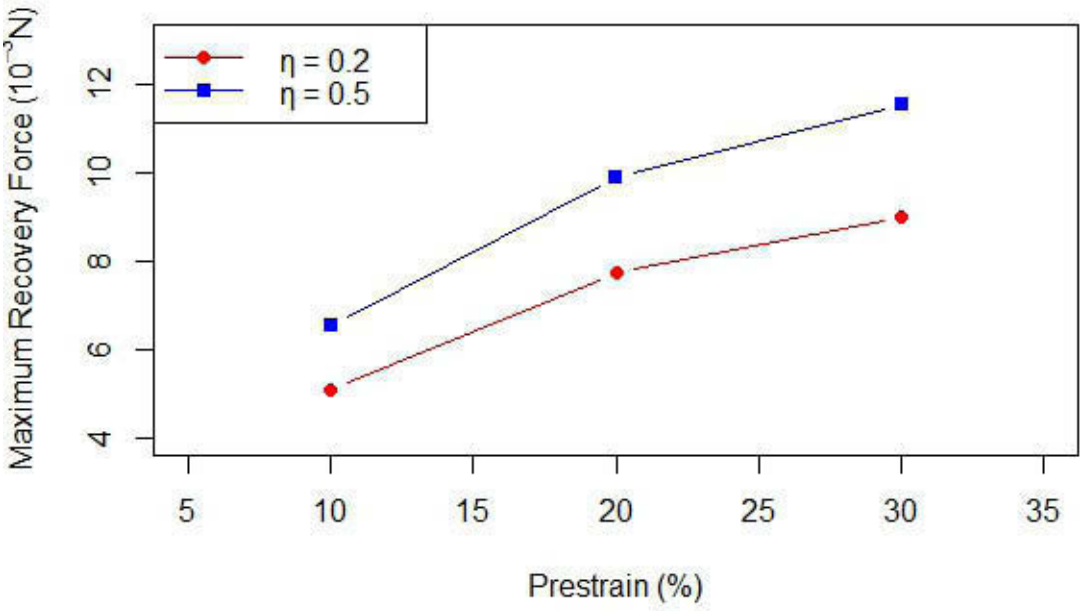

Figure 3.6: Maximum recovery force vs. prestrain obtained by simulation for models with different thickness ratios.

3.4.2 Folding Angle

3.4.2.1 Calculation Method

In Chapter 2, we defined the maximum non-predetermined folding angle as Figure 2.7a.

Here, we approximate the folding angle θ by drawing a straight line passing the last

two neighboring points (with integer x coordinates) of the top surface of the geometric model when reaching maximum folding angle configuration, as shown in Figure 3.7.

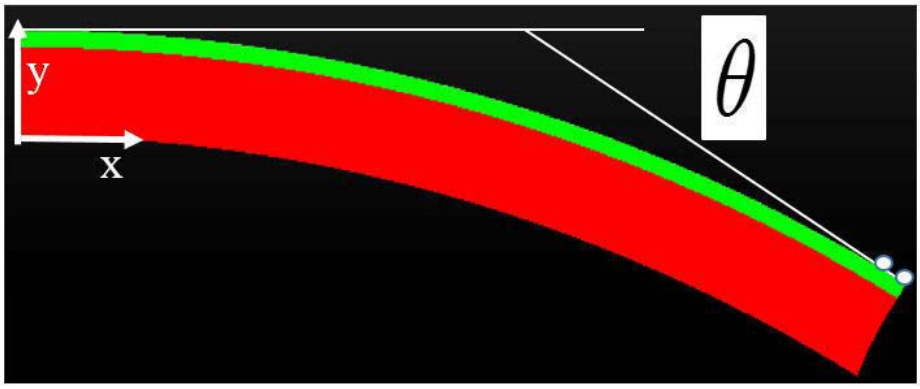

Figure 3.7: Folding angle approximation by calculating the slope of the last two neighboring points on the top surface.

Then, in order to calculate the slope of the tangent line, we need to output the coordinates of these two neighboring points when reaching maximum angle. Here we use the geometric model with original length 180 units, thickness ratio 0.3 and prestrain 30% as an example. The height of the top layer will be 6 (units length) in order to obtain 0.3 thickness ratio. Thus, the initial coordinates of the last two neighboring points of the top surface would be (180, 26) and (179, 26) (units length), then we output the increment of the x and y coordinates (D_X and D_Y) of these two points as shown in Figure 3.8a and Figure 3.8b, respectively.

We can obtain the coordinate changes of point with original coordinate (180, 26) in x and y direction from the Figure 3.8a: D_X = 45.9, D_Y = -57.1.

Similarly, we can get D_X and D_Y of point with original coordinate (179, 26): D_X = 45.7, D_Y = -56.6. It is noticed that the coordinate changes of the two points must

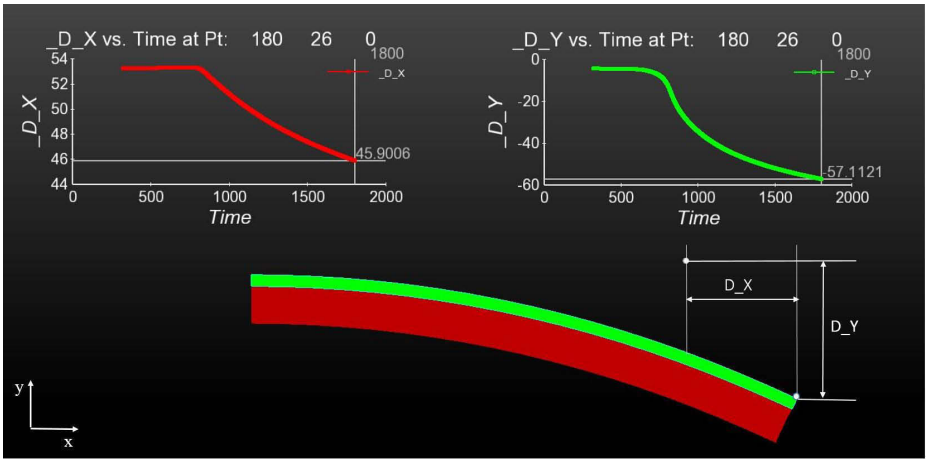

(a)

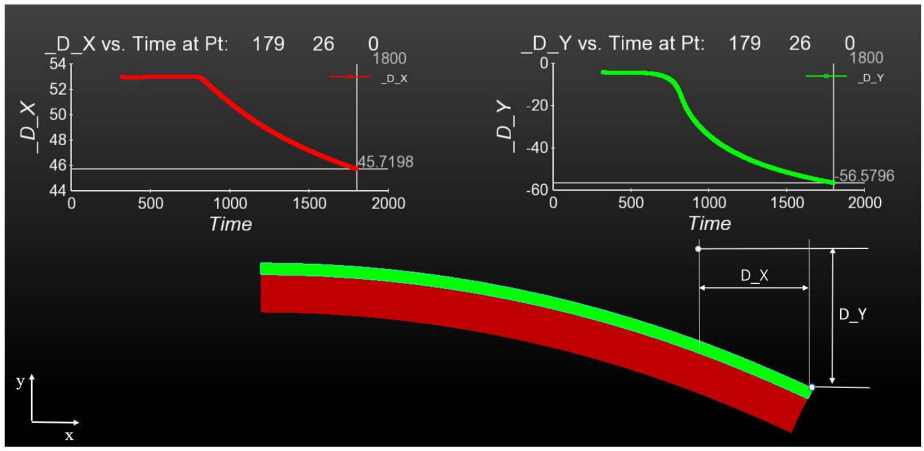

(b)

Figure 3.8: Simulation results tracking the coordinate change of the last point with coordinate (180, 26) on the top surface as a function of time (thickness ratio=0.3) (a) and the second last point with coordinate (179, 26) on the top surface as a function of time (thickness ratio=0.3) (b).

be obtained at the same time ($t = 1800$ s in this case). Thus, we can get the updated coordinates of the two points corresponding to maximum angle configuration: (225.9, -31.1) and (224.7, -30.6). Then, we can calculate the slope as:

$$tan\theta = \frac{-30.6 - (-31.1)}{|224.7 - 225.9|} = 0.42$$

So, we can calculate the maximum folding angle θ:

$$\theta = 22.8^{\circ}$$

3.4.2.2 Result

By using this method, we calculated a series of maximum non-predetermined folding angles in degree (°) and plotted versus prestrain with thickness ratios η=0.2, 0.3 and 0.5 in Figure 3.9. The data follow a trend of increasing maximum folding angle with increasing prestrain, which agrees with the prediction of the equation 2.7. However, the maximum folding angle will increase with the decrease of the thickness ratio, which does not agree with the trend we can see from Figure 2.11.

The calculation method above only involved two points of the maximum folding angle configuration. Next, we turned to the mean curvature of the configuration in simulation to express bending extent. First, we obtained the snapshot from simulation as shown in Figure 3.10, and then we rotated and transferred it into binary image, illustrated in Figure 3.11. Refer to Appendix A for the calculation of the mean curvature.

Then, we did curve fitting (polynomial regression) and calculated the corresponding curvature κ of the point on the curve with coordinate (x, y) as:[56]

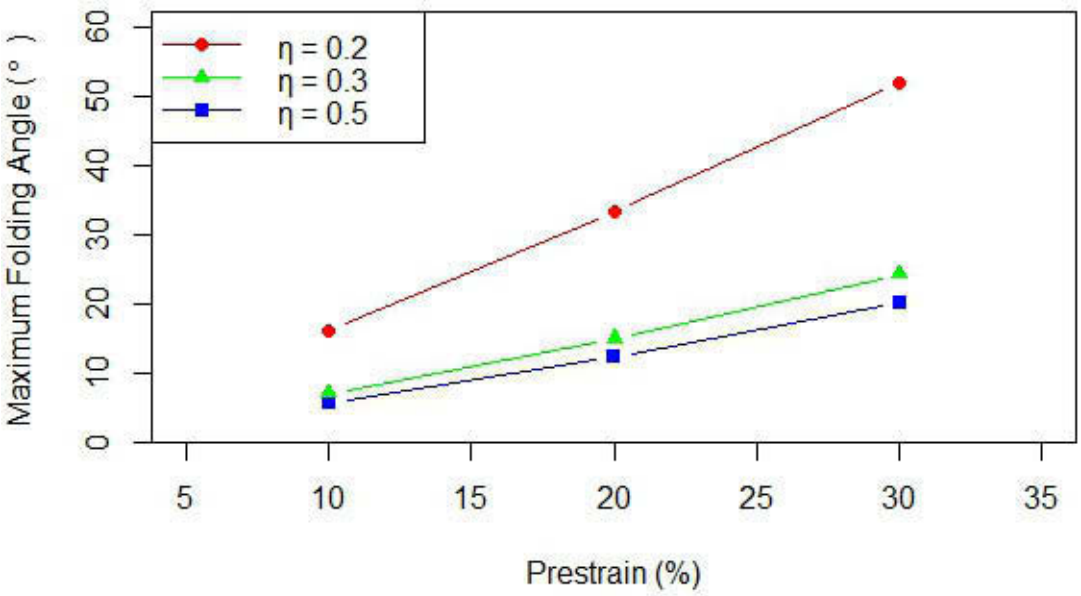

Figure 3.9: Maximum non-predetermined folding angle vs. prestrain obtained by simulation for actuators with different thickness ratios.

$$\kappa = \frac{y''}{(1 + y'^2)^{3/2}}$$

And, we calculated the mean curvature of all the points on the fitting curve and plotted against prestrain as shown in Figure 3.12.

The mean curvature also has the increasing trend with the increase of prestrain and decrease of thickness ratio, which agrees with the maximum non-predetermined folding angle result in Figure 3.9.

Next, we plotted the stored strain energy of folded configurations (calculated using the mean curvature) against prestrain as Figure 3.13a by using equation 3.3. The

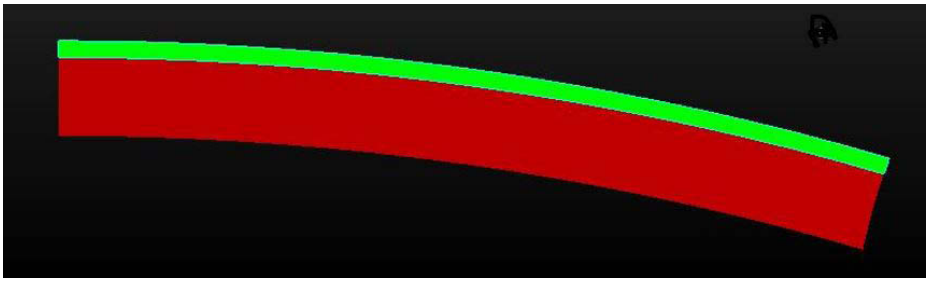

Figure 3.10: The original image for curvature calculation.

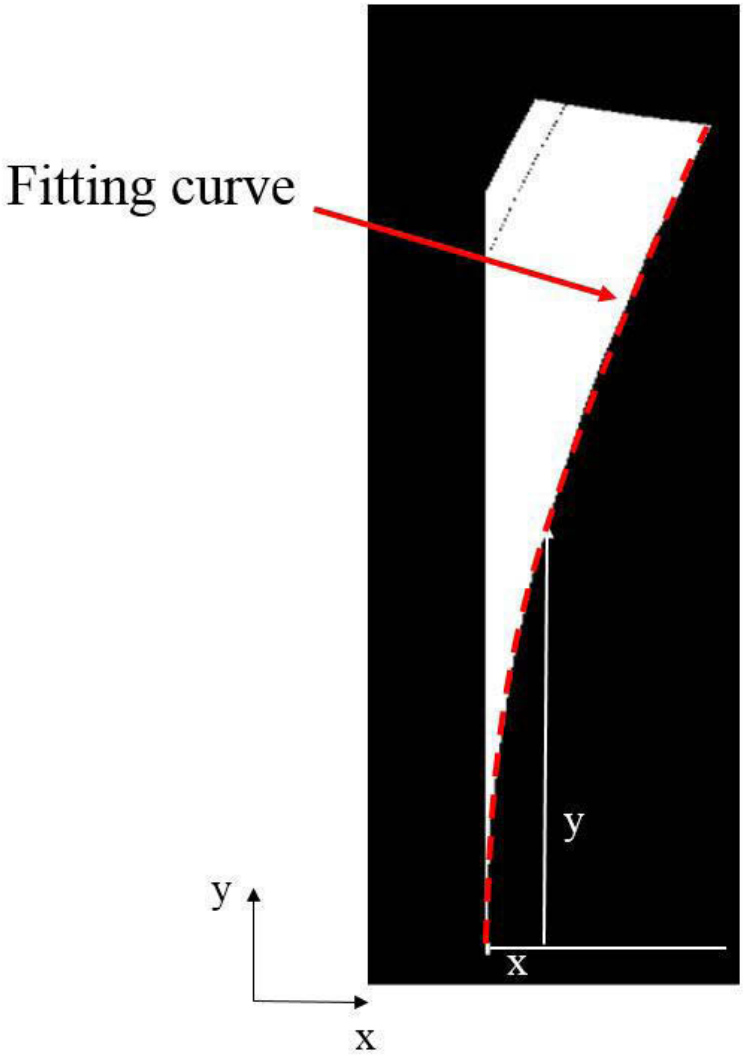

Figure 3.11: Transfer the orginal image into binary image.

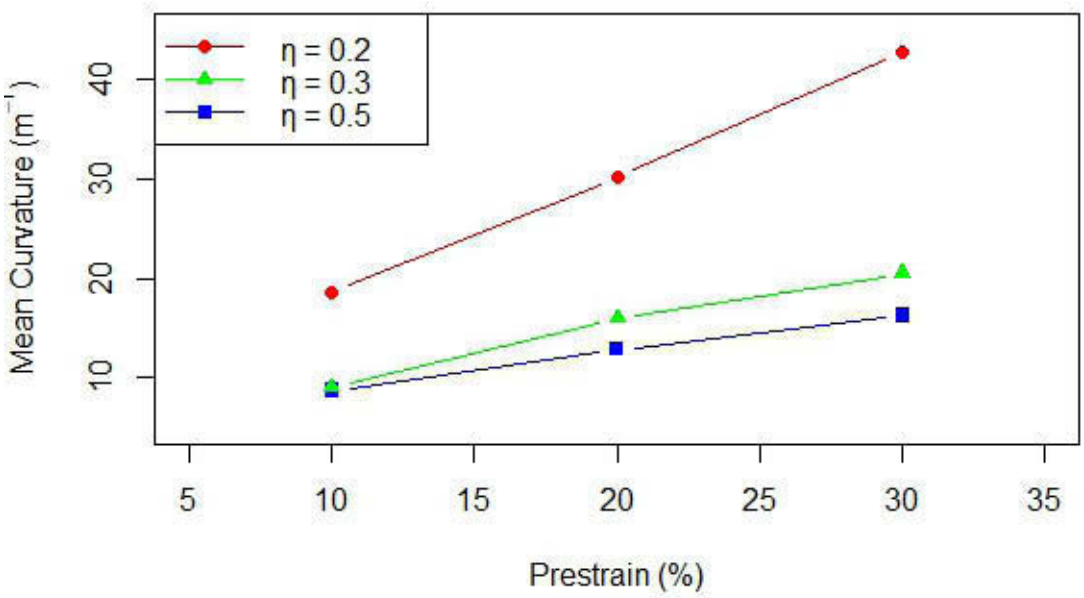

Figure 3.12: Mean curvature vs. prestrain for folding test in simulation.

derivation of the equation is shown as follows:

First of all, for an elastic bending beam, the curvature κ is related to the resisting moment M_r by:

$$\kappa = \frac{M_r}{EI} \tag{3.1}$$

where E is the modulus of elasticity of the beam material, I is the second moment of area for the cross section of the beam. Note that M_r, E and I may be functions of the coordinate x.

Also, the stored strain energy U of a bending beam is:

$$U = \int_0^L \frac{M_r^2}{2EI} dx$$

where L is the length of the beam in x direction.

Then by substituting equation 3.1 into it, we have:

$$U = \frac{1}{2} EI \int_0^L \kappa^2 dx \tag{3.2}$$

Considering that our model is bilayer structure, we can calculate the strain energy of the bilayer system as:

$$U = \frac{1}{2} E_1 I_1 \int_0^L \kappa^2 dx + \frac{1}{2} E_2 I_2 \int_0^L \kappa^2 dx \tag{3.3}$$

where E_1, E_2, I_1 and I_2 are the modulus of elasticity and the second moment of area for the cross section of two layers.

We can then calculate the stored strain energy of the folded configurations of the model by equation 3.3. Also refer to Appendix A for the Matlab code implementing equation 3.3 to calculate the stored strain energy.

We also calculated the stored strain energy using the combination of the maximum non-predetermined folding angle θ and equation 2.6, as Figure 3.13b. We can see that the calculated strain energy is higher than the case calculated by mean curvature. However, we believe the energy obtained by mean curvature is more reasonable than maximum non-predetermined folding angle since it is based on the overall deformation

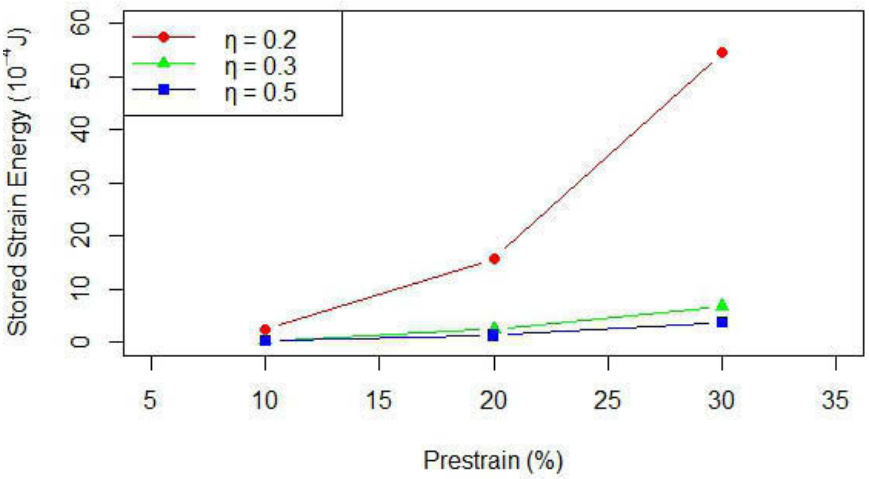

(a)

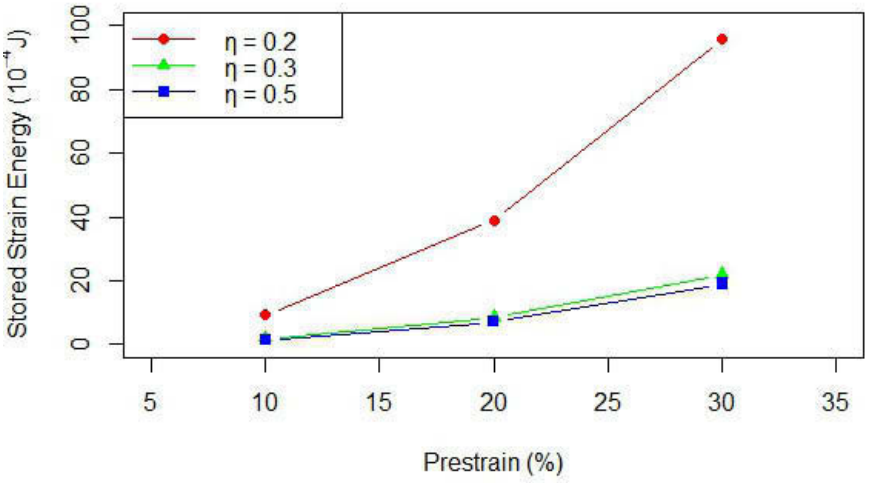

(b)

Figure 3.13: Stored strain energy vs. prestrain calculated by using mean curvature (a) and the maximum non-predetermined folding angle (b).

of the bilayer structure, whereas the maximum folding angle is localized only at the end of the beam.

3.5 Conclusion of the Chapter

A constitutive model for amorphous polymers developed by Xiao et al.[57] was used to explore the behavior of SMPC actuator and the performance of folding angle and recovery force generated during the folding process.

Based on the simulation results, we validated the hypothesis we made in Chapter 2 that the two important properties of the actuator (the maximum non-predetermined folding angle and corresponding maximum recovery force) depend on prestrain and the thickness ratio between the two SMP layers. The folding angle and recovery force, as well as the mean curvature of the folded configuration, have an increasing trend with the increase of the prestrain. We also calculated the stored strain energy corresponding to the maximum folded configuration and found that the stored strain energy also agreed with the trend described above. However, the thickness ratio has an opposite influence on the folding angle compared with what we can predict from Figure 2.11.

Although the simulation results only agreed with the analytical expression 2.7 partially, the results showed us the trend of the two important properties with changes of prestrain and thickness ratio so that it guided us how to adjust the properties of

the system for desired actuator performance. And experiment is necessary to validate the equation 2.7 so that in Chapter 5, we will conduct experiments and provide the values of folding angle and recovery force from measurements.

Chapter 4

The Fabrication of Bidirectional Actuators

In this chapter, we will describe the detailed fabrication process of the shape memory polymer composite actuators as well as present the bidirectional folding movement of the actuator after fabrication.

4.1 The Fabrication of Mold

4.1.1 Materials and Methods

In order to fabricate the bilayer SMP composite actuator, we need to make a proper mold. The mold fabrication procedure is described as follows and also shown in Figure 4.1:

- Use a laser cutter (Universal Laser System) to cut the acrylic bar purchased from McMaster-Carr into 40 mm × 15 mm × 6.4 mm specimens. Rinse specimens with DI water and dry. Place one specimen into the Karter Scientific 206D2 Plastic Petri Dish (diameter: 60 mm).

- Mix 20 g Sylgard 184 base with 2 g Sylgard 184 curing agent (available from Dow Chemical) with Mazerustar planetary mixer for 90 seconds. (prepolymer-to-curing agent ratio of 10:1).

- Pour PDMS mixture into the petri dish and cover the acrylic specimen completely. Place the petri dish into a vacuum desiccator for 1 h to eliminate air bubbles.

- Place the petri dish in the 60°C oven for 90 minutes or room temperature for 24 hours for curing PDMS.

- After curing, gently take out the solid PDMS block from the petri dish, and remove the embedded acrylic specimen from the PDMS so that we can get a negative mold. The mold is then cleaned extensively with ethanol, acetone and isopropanol sequentially, and dried.

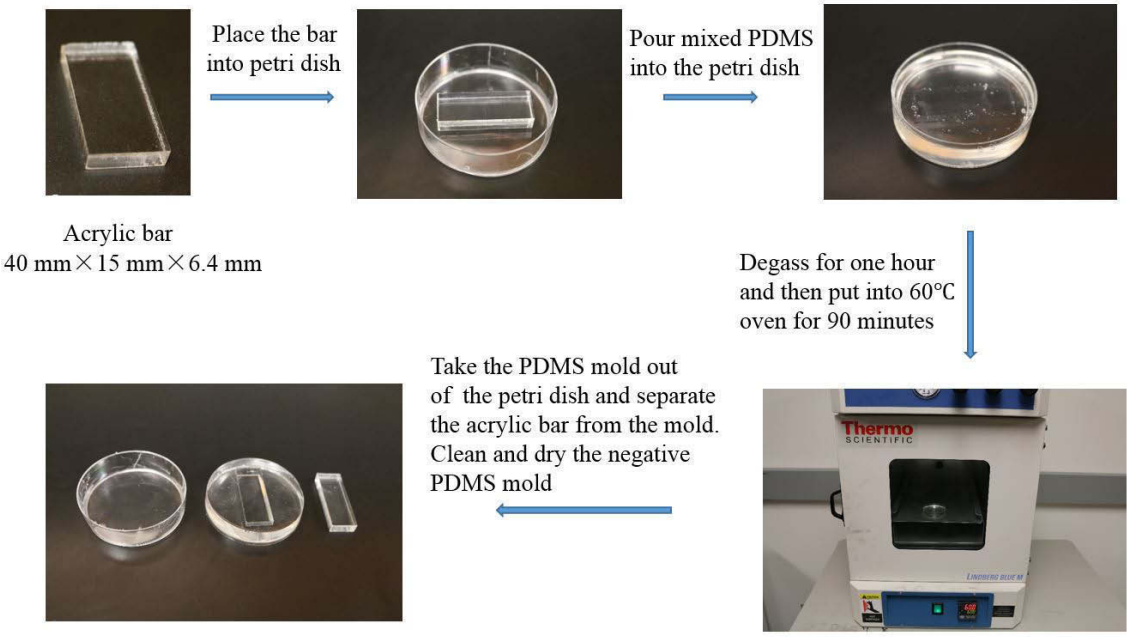

Figure 4.1: Mold fabrication process.

4.1.2 Surface Treatment

In our initial experiments, we found that the UV cured SMP composites synthesized into the mold would stick tightly to the bottom of the mold. Thus, the mold would be destroyed if we took the SMP composite out from the mold imperatively. In order to reuse the mold and decrease the fabrication cost, we need to do surface treatment to the PDMS mold for preventing the SMP composite sticking to the mold.

The surface treatment is composed of two steps - plasma cleaning and silane coating described as follows (Figure 4.2):

- Clean and dry the PDMS mold completely.
- Treat the mold with Oxygen plasma for 1 minute in a plasma cleaner (Harrick

Plasma). The aim of plasma cleaning is to activate the -OH groups of the PDMS to facilitate the bond formation with silane molecules.

- Place the PDMS mold in a vacuum desiccator overnight with a vial having 0.1 ml (tridecafluoro-1,1,2,2-tetrahydrooctyl)-trichlorosilane (available from Gelest, Inc.).

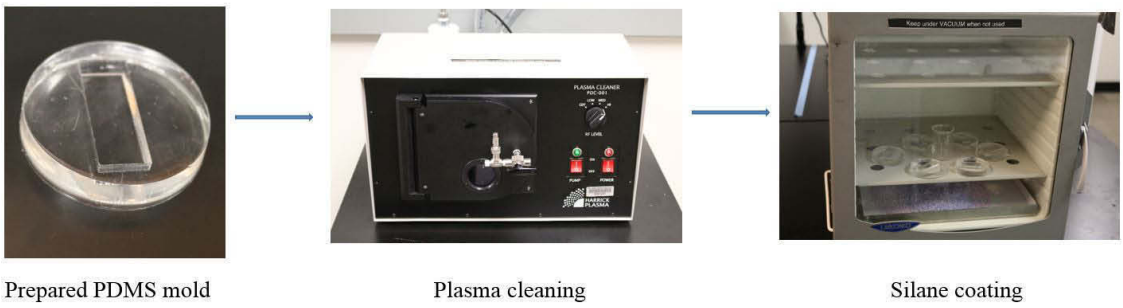

Figure 4.2: Procedures for surface treatment of the PDMS mold.

The surface energy of the PDMS mold is decreased after the silane coating treatment so that we can easily take out the cured SMPC from the mold without damaging the mold (Figure 4.3). However, considering that the UV may damage the silane coating during curing, it is recommended to redo the surface treatment after each curing cycle.

4.2 The Fabrication of Actuators

Then we can synthesize our SMP composite actuators using the mold. But, first of all, we need to address important parameters of synthesized SMPC including T_g,

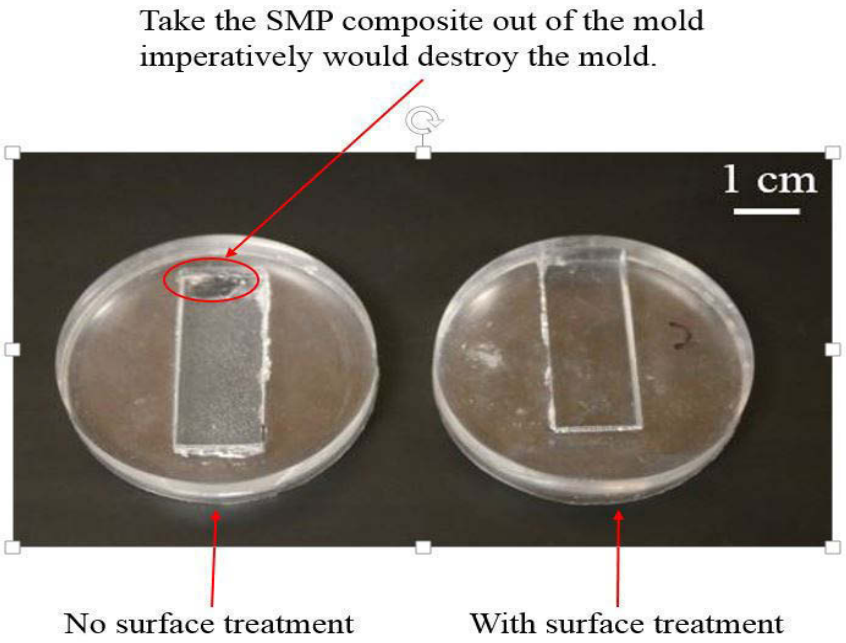

Figure 4.3: Effect of the surface treatment. *Left* The mold is easily destroyed without surface treatment due to strong adhension of the SMPC to the mold. *Right* We can easily take out the cured SMPC from the mold without damaging the mold.

thickness ratio, and prestrain, and figure out the way to control them because these parameters will determine the performance of our actuators.

4.2.1 Parameters Control

As we discussed in Chapter 2, the two parameters that determine the folding angle and recovery force are thickness ratio between two layers and prestrain. In addition, we introduced that, the difference between $T_g s$ of the two SMP layers should be large enough to produce enough strain mismatch for realizing the folding movement. Also, considering there exists partial recovery even when ambient temperature is still lower

than the $T_g s$ of the polymers, T_g^1 should be significantly higher than room temperature so that the partial recovery of SMP is negligible at room temperature. Thus, we have following two conditions to satisfy:

$$T_g^2 - T_g^1 \geq 10^\circ C$$

$$T_g^1 - T_{room} \geq 20^\circ C$$

The T_g of the SMP can be adjusted by changing the mass ratio of PEGDMA to tBA.[59] The T_g of cured SMP decreases with the increasing weight percent of PEGDMA in tBA-PEGDMA mixture, as shown in Figure 4.4 (data collected by using TA Q800 Dynamic Mechanical Analyzer (DMA)). In order to decrease the partial recovery of the cured SMP and guarantee that the difference between $T_g s$ is high enough, we decided to synthesize bilayer SMPC with two layers of 20 wt% PEGDMA ($T_g \approx$ 47°C) and 5 wt% PEGDMA ($T_g \approx$ 60°C), respectively.

Next, we can control the thickness ratio between the two layers by controlling their volume ratio considering that the two layers share same bottom area so that the thickness ratio equals their volume ratio. Although the thickness may change due to swelling or shrinkage after curing, the amount of change of two layers are almost the same. To control volume ratios, we need the density data of different weight percent of PEGDMA in tBA-PEGDMA mixture as shown in Table 4.1 to determine the mass of each layer. In our fabrication process, we fix the thickness of the bottom layer (20

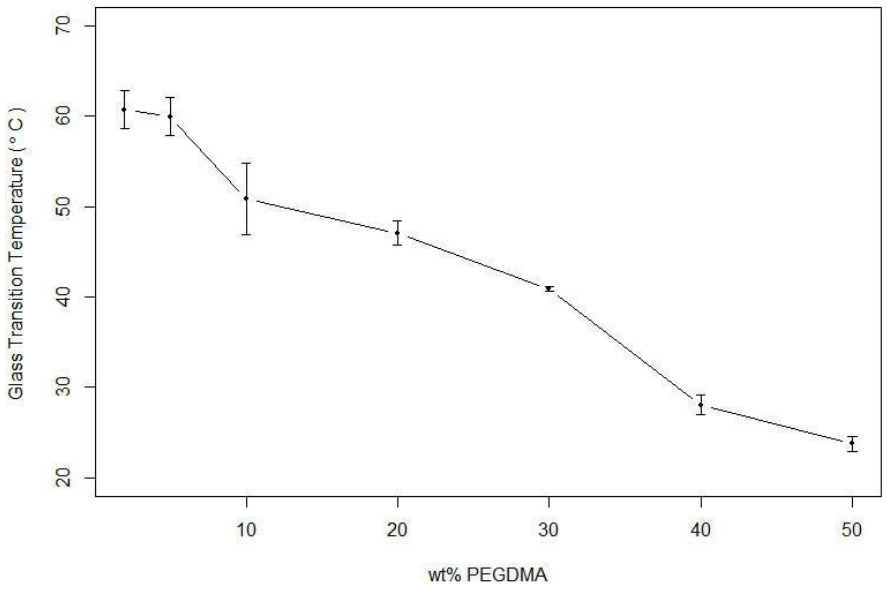

Figure 4.4: T_g as a function of wt% of PEGDMA in tBA-PEGDMA mixture. (N=5, error bars represent the standard deviation.)

wt% PEGDMA) to 2 mm (1.0946 g) and only change the thickness of the top layer (5 wt% PEGDMA) to get different thickness ratio bilayer structures. The mass of the top layer corresponding to different thickness ratios are shown in Table 4.2.

In addition, we need to determine a reasonable range of the desired thickness ratio. After experiments, we decided to choose thickness ratio (η) ranging from 0.2 to 0.5. If η was less than 0.2, it was difficult to form a uniform layer of 5 wt% PEGDMA SMP on top of 20 wt% PEGDMA SMP layer (fixed to 2 mm thickness). If η was higher than 0.5, it was hard to activate both SMP layers by heating considering that SMP was not a good heat conductor, and hard to program the actuator by stretching due to the high stiffness.

In order to validate the described method can provide desired thickness ratios, we can measure the thickness ratio between two layers of cured SMP precisely using the image captured under microscope as shown in Figure 4.5. The image analysis result is shown in Table 4.3. To get satisfactory microscope image, the sample should be well prepared using polish paper and cleaned completely.

wt% PEGDMA	ρ (g/ml)
5	0.8840
10	0.8932
20	0.9122
30	0.9320
40	0.9527

Table 4.1: Densities of tBA-PEGDMA mixture with different wt% of PEGDMA.

Thickness Ratio	Mass of Top Layer (g)
0.2	0.2122
0.3	0.3183
0.4	0.4244
0.5	0.5304

Table 4.2: The mass of the top layer corresponding to different thickness ratios.

Thickness *top* (μm)	Thickness *bottom* (μm)
622	2105
613	2087
594	1996
Average (std)	Average (std)
610 (14)	2063 (58)
Thickness Ratio:	0.3

Table 4.3: Thickness ratio measurement under microscope.

Finally, we can control the amount of prestrain precisely by using Mechanical Test-

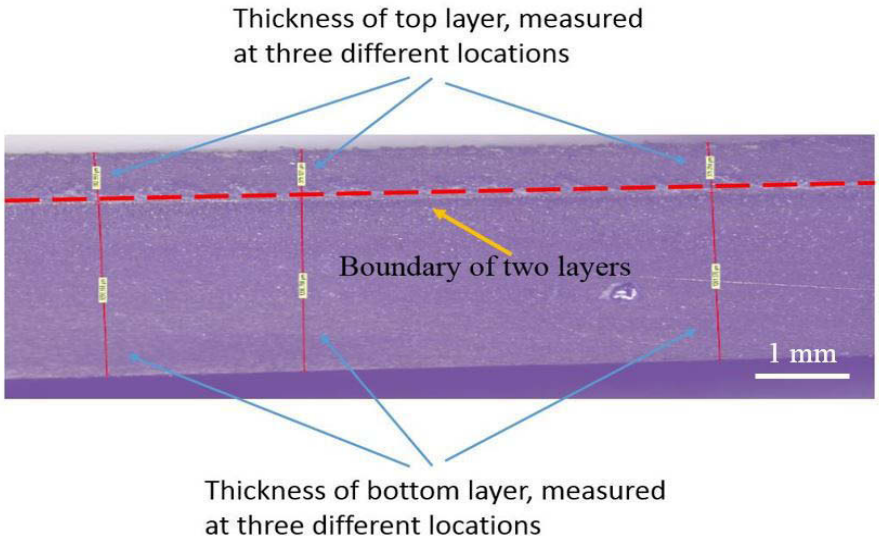

Figure 4.5: Measure thickness ratio between two layers precisely under microscope.

ing System (MTS), the detailed operation procedure will be described in next chapter. A summary of the control methods for three parameters is shown in Table 4.4.

Parameters	Control Method
T_g	wt% of PEGDMA
Thickness Ratio (η)	Mass Ratio
Prestrain (ε)	MTS

Table 4.4: The methods we use to control parameters.

4.2.2 Fabrication Process

Based on the methods introduced above, the fabrication process of an actuator is described as follows (Figure 4.6):

- Purchase tert-Butyl acrylate (tBA), poly(ethylene glycol)$_n$ dimethacrylate (PEGDMA)

with molecular weight of M_n=550, and photoinitiator 2,2-dimethoxy-2-phenylacetophenone (DMPA) from Aldrich and use as-received conditions.

- Mix tBA and PEGDMA in a 4 : 1 mass ratio (20 wt% PEGDMA), then add 0.5 wt% DMPA into the tBA-PEGDMA mixture. Inject the polymer mixture into the mold and polymerize the mixture in a UV oven (UVP, CL1000) for 7 minutes.

- Mix tBA and PEGDMA in a 19 : 1 mass ratio (5 wt% PEGDMA), then add 0.5 wt% DMPA into the tBA-PEGDMA mixture. Add specific weight (depends on the thickness ratio we need) of the polymer mixture onto the top of the previous cured layer. Place the mold into the UV oven for another 6 minutes to polymerize the top layer.

- Following UV curing, peel off the bilayer SMP specimen from the mold and use a clamp and tapes to fix an angled shape of the specimen as shown in Figure 4.6. Then, place the specimen in an oven at 70°C for one hour post curing. By using this method, we can synthesize SMP with an angled permanent shape as shown in Figure 4.6.

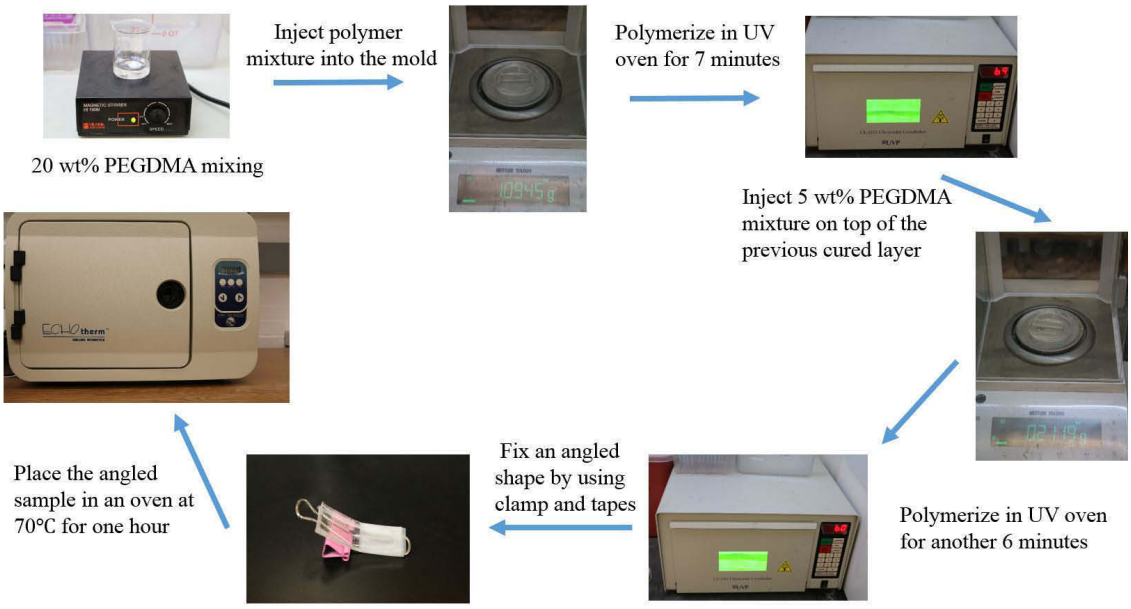

Figure 4.6: The fabrication process of the actuator.

4.3 Bidirectional Folding Performance of the Fabricated Actuators

In Chapter 2, we have introduced that the bidirectional folding mechanism of the actuator is the combination of shape memory effect and strain mismatch between two layers. Here, we show its bidirectional folding performance as follows (Figure 4.7). The sample used for test is a bilayer SMP composite, composed of 5 wt% PEGDMA SMP layer (T_g=60°C) and 20 wt% PEGDMA SMP layer (T_g=47°C), with thickness ratio of 0.3 and 30 % prestrain. The sample was fabricated based on the fabrication process introduced above and was actuated by a heat gun (set to 93.3°C).

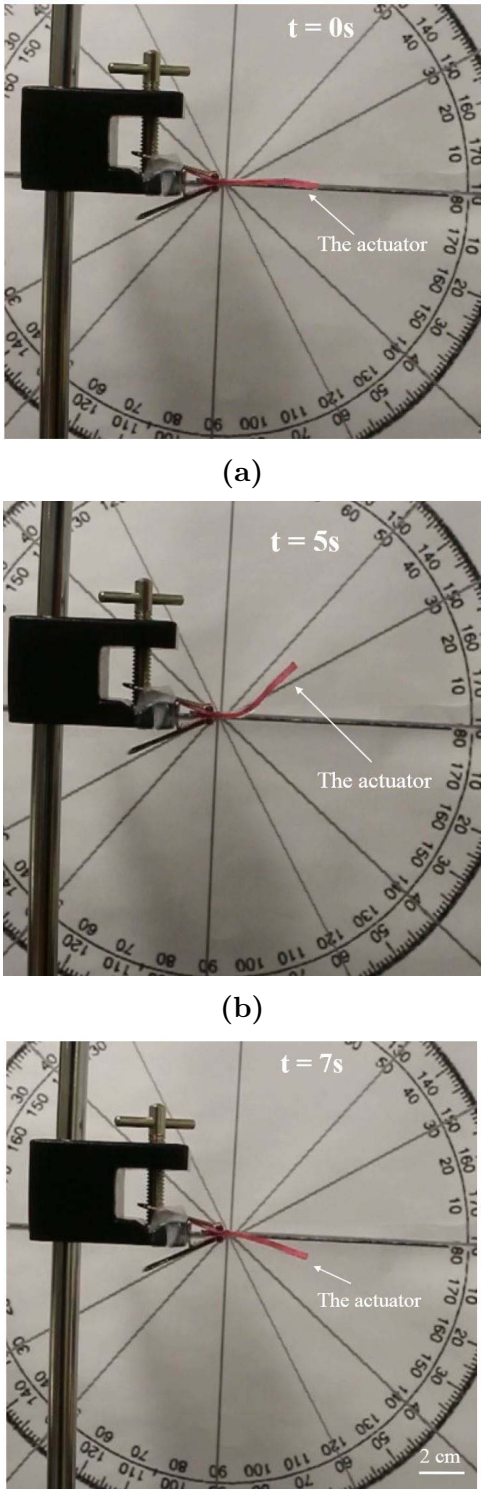

Figure 4.7: Bidirectional folding performance of the fabricated actuator. Initial state of the actuator (a) and the actuator folds upward (b) and the actuator folds downward (c).

4.4 Conclusion of the Chapter

In this chapter, we described the fabrication and surface treatment processes of the PDMS mold, in which we synthesized our SMPC actuator. The surface treatment should be conducted after each curing cycle to avoid adhension of SMP to the bottom of the mold. Next, we described the fabrication process of bidirectional folding actuators and the specific methods we adopted to control important parameters of the actuators, including thickness ratio (η), prestrain (ε) and glass transition temperature (T_g). In order to realize bidirectional folding movement, the SMPC should have an angled permanent shape which is achieved by using clamp and tapes during post curing in oven. Finally, we showed the bidirectional folding movement of the actuator to validate our design and fabrication.

In next chapter, we will discuss the characterization methods and performance of the actuator, including two important properties-maximum non-predetermined folding angle and corresponding maximum recovery force-to prove our previous hypothesis that these two properties can be controlled by adjusting thickness ratio between two layers and prestrain.

Chapter 5

The Characterizations of Bidirectional Folding Actuators

In this chapter, we will conduct characterizations of the actuator so that we can verify the hypothesis we made in Chapter 2 that two important properties of our actuator-the maximum non-predetermined folding angle and the corresponding maximum recovery force-can be adjusted by controlling thickness ratio (η) between two layers and the prestrain (ε). The hypothesis is based on equation 2.7, which was derived in Section 2.3.

Here, we will describe sample preparation methods, characterization methods and results of recovery force and folding angle of the actuator.

5.1 Sample Preparation

As we presented in Section 4.2.1, we decided to synthesize bilayer shape memory polymer composite with weight percent of PEGDMA 20% ($T_g \approx$ 47°C) and 5% ($T_g \approx$ 60°C) for each layer, respectively. Also, we decided to choose thickness ratio η ranging from $0.2 \sim 0.5$ after experiments, which was controlled by controlling the volume ratio between two layers. Next, we need to determine a suitable range of polymer prestrain and tensile test is necessary.

5.1.1 Tensile Testing and Prestrain Range

We chose universal testing machine (MTS Insight 5) to conduct tensile testing due to limitations in sample size and applied load (18 N) of Dynamic Mechanical Analyzer (DMA). Figure 5.1 illustrates the experimental setup. The original dimensions of the samples were recorded before mounting on the machine for testing. In order to avoid slipping of samples during stretch, a pair of clamps with anti-slipping surfaces were used to fix the SMP composite samples vertically. The samples should not be clamped very tightly to prevent damage of the sample. Parameters used for tensile testing are listed in Table 5.1.

Strain Rate (s^{-1})	Stretched Area Length (mm)	Isothermal Temperature (°C)	Soak Time (min)	Load Cell (N)
0.0028	18	43	5	500

Table 5.1: Parameters used for tensile testing.

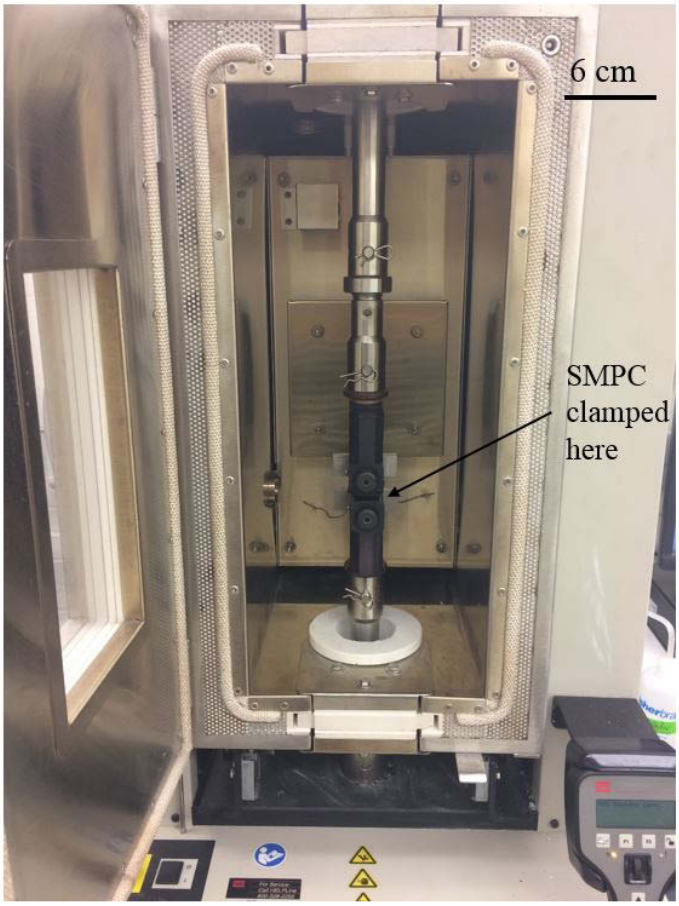

Figure 5.1: The picture of a SMPC sample mounted on a universal testing machine for tensile testing.

The reason of the choice of some of these parameters for tensile testing is explained as follows:

- Stretched area length was set to 18 mm because the minimum distance of the upper and lower clamps used to fix SMP is about 18 mm, below which the universal testing machine cannot work.

- Isothermal temperature was set to 43°C. Since as we can see from Figure 2.3, the storage modulus and loss modulus of SMP would decrease sharply once the

ambient temperature is near T_g so that the SMP is soft and the stretchability of the SMP is poor. Moreover, we need to reach a temperature around T_g so that we can program a new temporary shape for SMP. Considering both conditions, we decided to stretch SMPC actuator at 43°C, which is 10% lower than the T_g of the 20 wt% PEGDMA SMP layer ($T_g \approx$ 47°C) after several tests.

- Soak time is 5 minutes, meaning that we need to keep SMP in 43°C isothermal environment for five minutes before stretching to guarantee the thermal equilibrium is reached.

Based on the parameters for tensile test introduced above, we tested the stretchability of SMPC actuator with thickness ratio (η) 0.2 (the least thickness ratio) to get the safe range of the prestrain to prevent the failure of the actuator during stretching process. We tested actuators with thickness ratio 0.2 to obtain the safe range of prestrain because the stretchability of SMPC actuator is better with higher thickness ratio (η), considering the elastic modulus of 5 wt% PEGDMA SMP layer is higher than that of 20 wt% PEGDMA layer at the same temperature.

Figure 5.2 shows the test results. From the results, we can conclude that the maximum prestrain that we can apply to the SMPC with η 0.2 should be about 30%, which would also be safe for the actuators with thickness ratios $\eta \geq$ 0.2.

Based on the tensile testing results above, we would use the universal testing machine to stretch samples with thickness ratios 0.2 and 0.5, to prestrains 10%, 20% and 30%. The samples were stretched using the same parameters for tensile testing

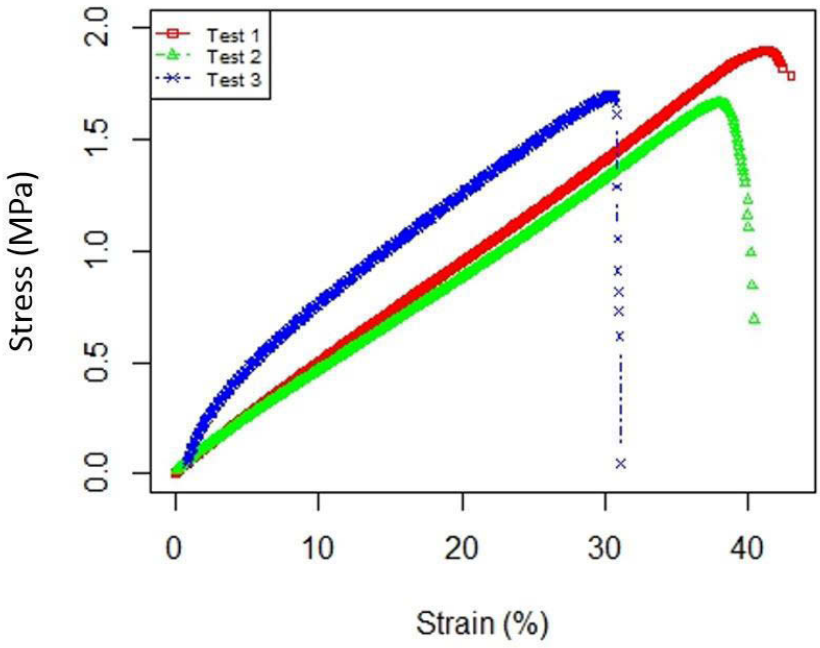

Figure 5.2: Tensile test result of the SMPC actuator with thickness ratio (η) of 0.2. The strain rate is 0.0028 s^{-1}.

in Table 5.1 and then were used for recovery force and folding angle measurement, which will be described in next section.

As a conclusion of this section, we summarize the discussion above in Table 5.2:

Sample Composition	Thickness Ratio η	Prestrain ε
20 wt% PEGDMA and 5 wt% PEGDMA	$0.2 \sim 0.5$	$0.1 \sim 0.3$

Table 5.2: Choices of sample parameters, including sample composition, thickness ratio between two layers and the prestrain of the sample.

5.2 Characterization Results

5.2.1 Recovery Force Measurement

5.2.1.1 Setup & Procedures

The maximum recovery force is one of the most important performance measures of the SMPC actuator which determines the range of application of the actuator. Here we measured the maximum recovery force of the actuator in two folding directions. We constructed the apparatus shown in Figure 5.3a to explore the influence of thickness ratio η and prestrain ε on the recovery force of the SMPC actuator during its folding process. The apparatus is composed of a platform where the actuator was clamped to and a load cell to measure the recovery force. The SMPC actuator was clamped on the platform and put close but not in contact with the probe of the load cell (Figure 5.3b). In order to activate the actuator, we used one 5 Ω resistor as a heating element and Arduino (5V output pin) as a power source. Measured by thermocouple at room temperature, once connected with the Arduino, the resistor can quickly increase the temperature of the actuator around 100°C in 30 seconds and provide the stable temperature around 145°C in 120 seconds, which are above the $T_g s$ of both SMP layers. In order not to interfere the folding action of the actuator, we held the resistor close to the actuator to provide heat but did not touch it.

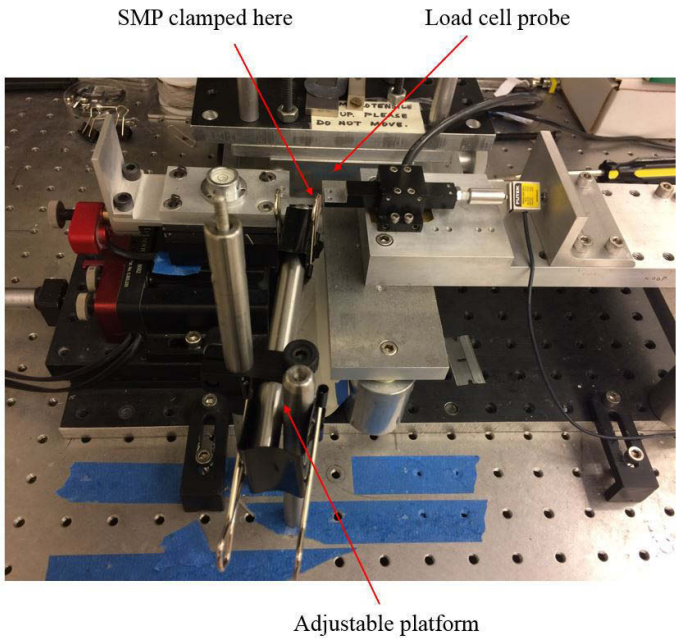

(a)

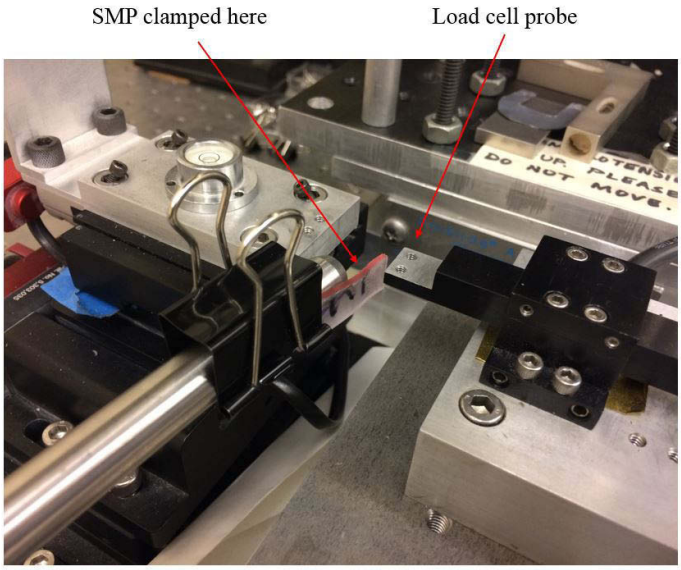

(b)

Figure 5.3: The apparatus used for measuring the recovery force of a SMPC actuator (a) and the zoom-in vision that the SMPC actuator was clamped close but not contact with the probe of the load cell (b).

5.2.1.2 Results

We then analyzed the collected data from the load cell and obtained the maximum recovery force in Newton (N) of each testing SMP composite sample versus prestrain, as plotted in Figure 5.4. For each actuator with determined thickness ratio and prestrain, we collected data from five samples.

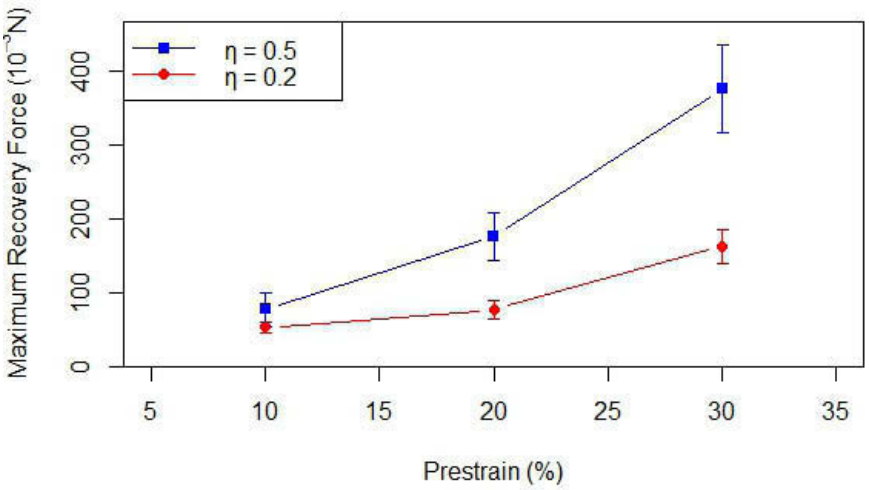

Figure 5.4: The maximum recovery force of a SMPC actuator in rightward folding direction as a function of a prestrain value. (N = 5, error bars represent the standard deviation)

We also measured the maximum recovery force when the SMPC actuator folded in the other direction (corresponding to the predetermined folding angle direction) using the same method and apparatus, as shown in Figure 5.5. For each SMP composite actuator with determined thickness ratio and prestrain, we collected data from three samples.

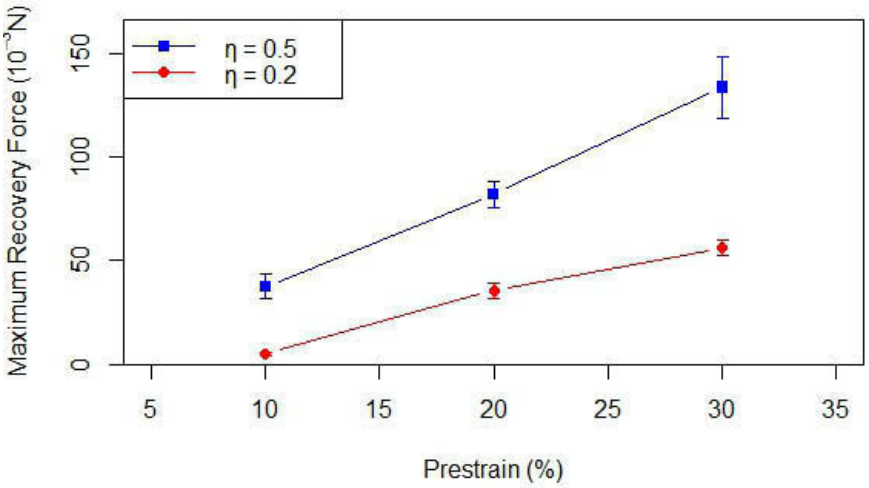

Figure 5.5: The maximum recovery force of a SMPC actuator in leftward folding direction as a function of a prestrain value. (N = 3, error bars represent the standard deviation)

From the figures, we can conclude that both maximum recovery force of SMPC actuator during its bidirectional folding action have increasing trend with the increase of thickness ratio (η) and prestrain (ε), which agrees with the hypothesis we made in Section 2.3.

5.2.2 Folding Angle Measurement

5.2.2.1 Setup & Procedures

Here we only introduce the methods and results of maximum non-predetermined folding angle measurement. In order to measure the maximum non-predetermined folding angle that a SMPC actuator with specific thickness ratio (η) and prestrain

(ε) can reach, we constructed the apparatus shown in Figures 5.6a. The apparatus includes a platform where the SMP actuator was clamped to, a camera to record videos of the folding process, and an angle-division paper as the background. In order to activate the folding process, we fixed a 5 Ω resistor to the bottom of the actuator and used Arduino (5V output pin) as a power source. The maximum folding angle was measured from the snapshot of the video recorded by the camera. In order to measure the folding angle precisely, the camera, actuator and the angle-division paper should be aligned collinearly, illustrated in Figure 5.6b.

5.2.2.2 Results

The maximum non-predetermined folding angle is plotted versus prestrain for the actuators of thickness ratios η=0.2 and 0.5 in Figure 5.7, respectively. For each SMPC actuator with determined thickness ratio and prestrain, we collected data from five samples. The measured folding angle values range from 41° to 102°. The data follow a trend of increasing maximum folding angle with increase of prestrain and decrease of thickness ratio, which agrees with what we can predict from equation 2.7 and Figure 2.11.

We also measured the mean curvature of the folded configuration to express the folding extent as we did in Chapter 3. First, we obtained the snapshot as shown in Figure 5.8a, and then we rotated and transferred it into binary image, illustrated in Figure 5.8b. Next, we conducted curve fitting (polynomial regression) and calculated

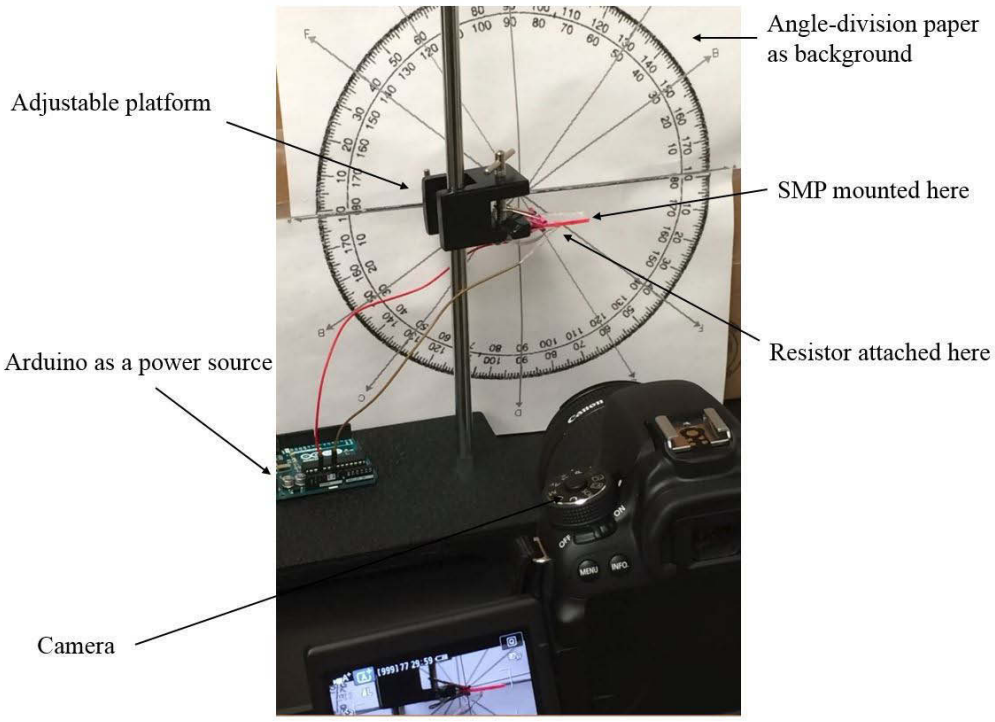

(a)

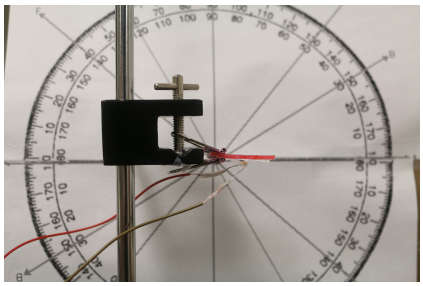

(b)

Figure 5.6: The apparatus used for measuring the folding angle of a SMPC actuator (a) and the image of the SMPC in camera (b).

the corresponding curvature κ of the point on the curve with coordinate (x, y) as:[56]

$$\kappa = \frac{y''}{(1 + y'^2)^{3/2}}$$

Then, we calculated the mean curvature of all the points on the curve and plotted

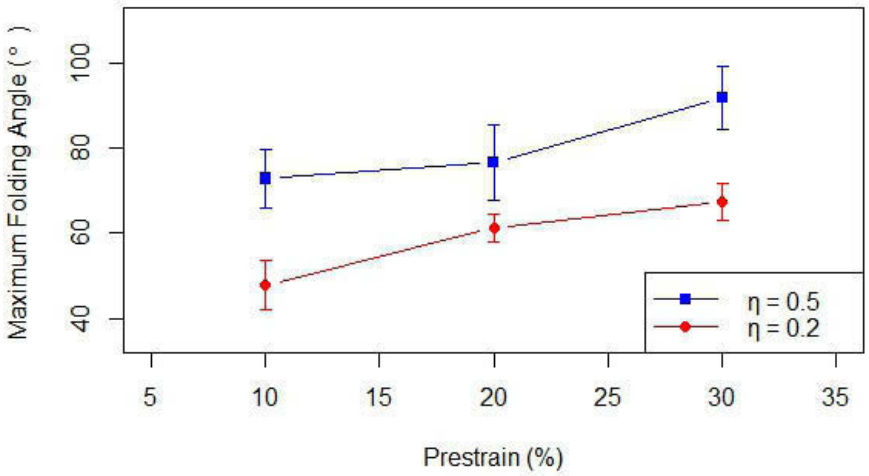

Figure 5.7: The maximum folding angle of a SMPC actuator in downward folding direction as a function of a prestrain value. (N = 5, error bars represent the standard deviation)

the mean curvature versus prestrain in Figure 5.9. For each SMPC actuator with determined thickness ratio and prestrain, we collected data from five samples. We observed that the mean curvature also had the increasing trend with the increase of prestrain and thickness ratio.

Next, we calculated the stored strain energy of the folded configurations using equation 3.3 mentioned in Section 3.4.2.2, and plotted against prestrain as Figure 5.10. Refer to Appendix A for the Matlab code I used to calculate the store strain energy of the curved configurations by using mean curvature.

We also calculated the stored strain energy using the combination of maximum non-predetermined folding angle θ obtained from experiment and equation 2.6, and plotted as Figure 5.11. We can see that the energy is higher than the case calculated

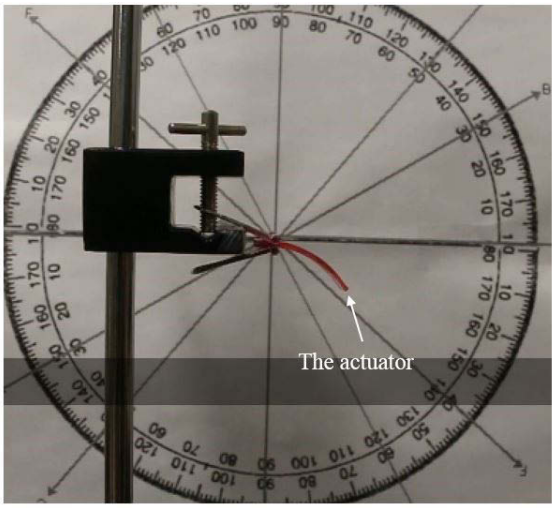

(a)

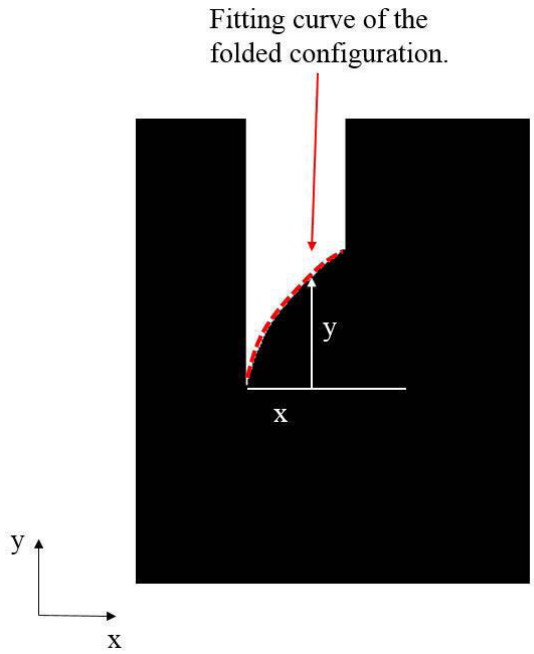

(b)

Figure 5.8: Images used to calculate the mean curvature. The original image (a) and the binary image (b).

by mean curvature. However, we believe the energy obtained by mean curvature is more reasonable than maximum non-predetermined folding angle since it is a global

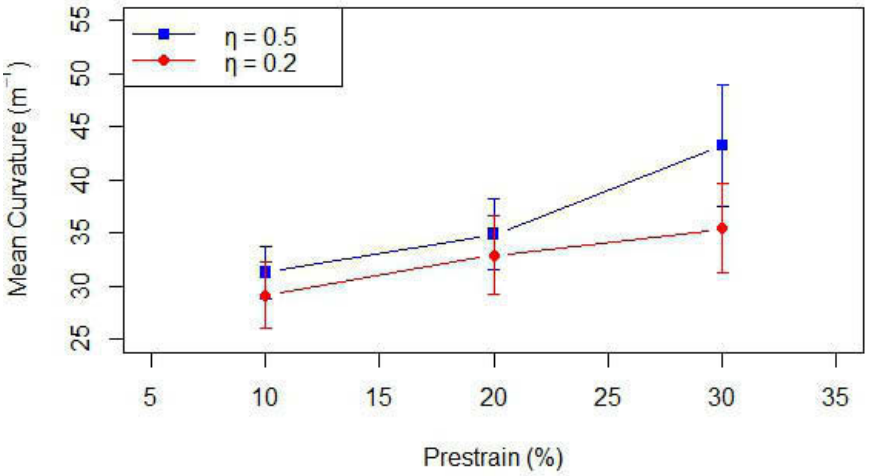

Figure 5.9: The mean curvature vs. prestrain value for the SMPC actuators with different thickness ratios (η). (N = 5, error bars represent the standard deviation)

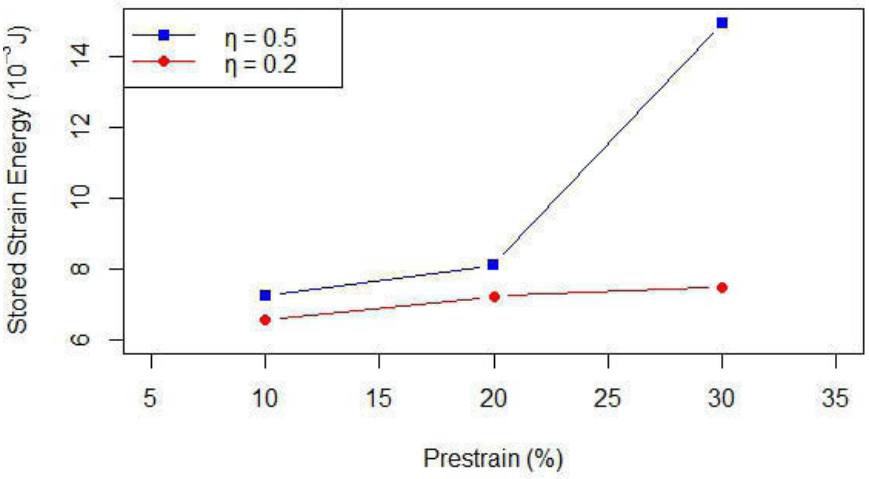

Figure 5.10: Stored strain energy vs. prestrain calculated by using mean curvature.

consideration, whereas the maximum folding angle is localized only at the end of the beam.

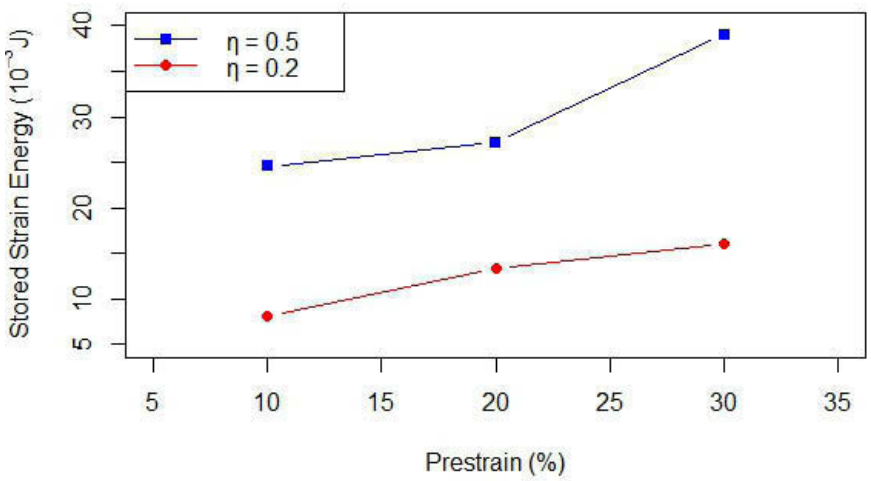

Figure 5.11: Stored strain energy vs. prestrain calculated by using maximum non-predetermined folding angle.

Then, we plotted the mean curvature against maximum non-predetermined folding angles of the same SMPC actuator in Figure 5.12a and Figure 5.12b, with thickness ratios η=0.2 and 0.5, respectively. As can be seen from these figures, the curvature is positively correlated to the maximum folding angle value. The coefficient of determination (R^2) values for the linear regression of these data are 0.6148 and 0.7389.

From the information above, we can see that the thickness ratio (η) and the prestrain (ε) have similar effect on the maximum recovery force and folding angle: both of them will increase with the increase of η and ε. In order to validate another prediction we made in Chapter 2 that the maximum recovery force is positively correlated to the maximum non-predetermined folding angle, we also plotted the maximum recovery force versus maximum folding angle of the same SMPC actuator as shown in

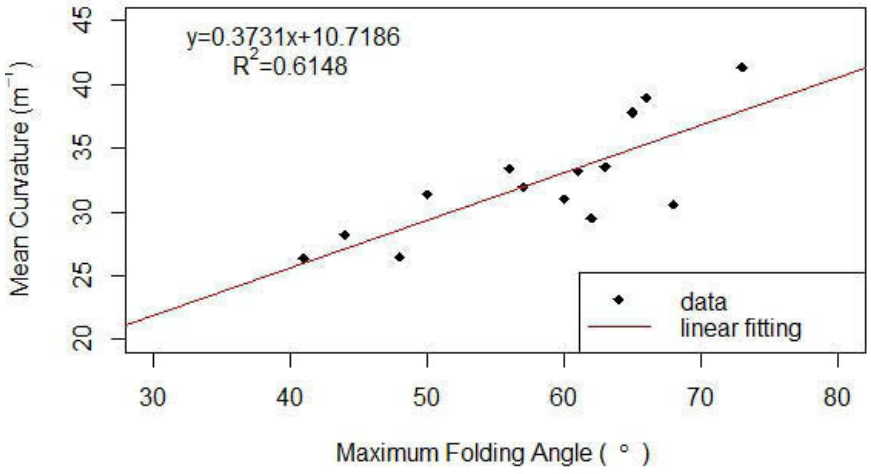

(a)

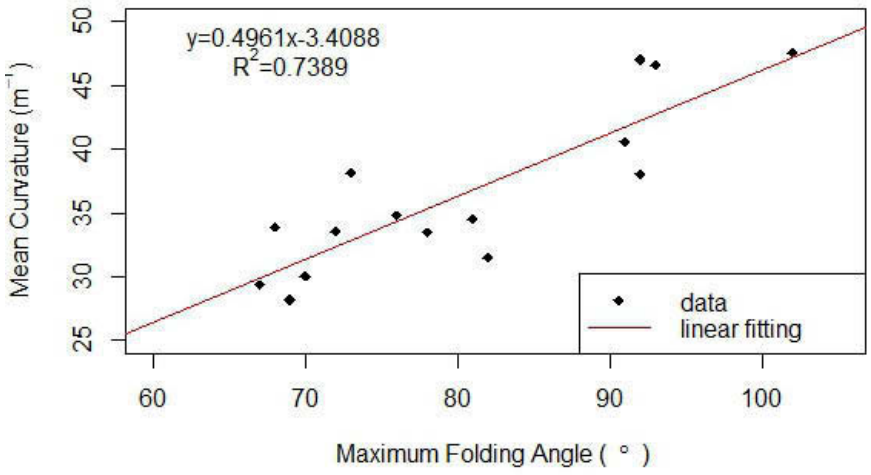

(b)

Figure 5.12: The mean curvature versus the maximum non-predetermined folding angle for the actuators with thickness ratios of 0.2 (a) and 0.5 (b).

Figure 5.13a and Figure 5.13b. The coefficient of determination (R^2) values for the linear regression of these data are 0.5732 and 0.6944, suggesting a correlation between the maximum recovery force and the maximum folding angle.

5.3 Comparison

In this section we will compare the values of the maximum non-predetermined folding angle obtained by the analytical equation 2.7, the numerical model introduced in Chapter 3 and the experimental measurements described in this chapter.

5.3.1 Folding Angle

We compared the maximum non-predetermined folding angle values obtained via the three methods (analytical, numerical, and experimental analysis) versus prestrain and plotted as shown in Figure 5.14.

From Figure 5.14, we can see that the three methods all agree that the maximum non-predetermined folding angle would increase with the increase of the prestrain. However, there exists discrepancy among them that the analytical method tends to overestimate the folding angles while the numerical simulation underestimates them. Although discrepancy exists, we can prove the previous hypothesis that the maximum non-predetermined folding angle can be controlled via adjusting the thickness ratio between two layers and their prestrain.

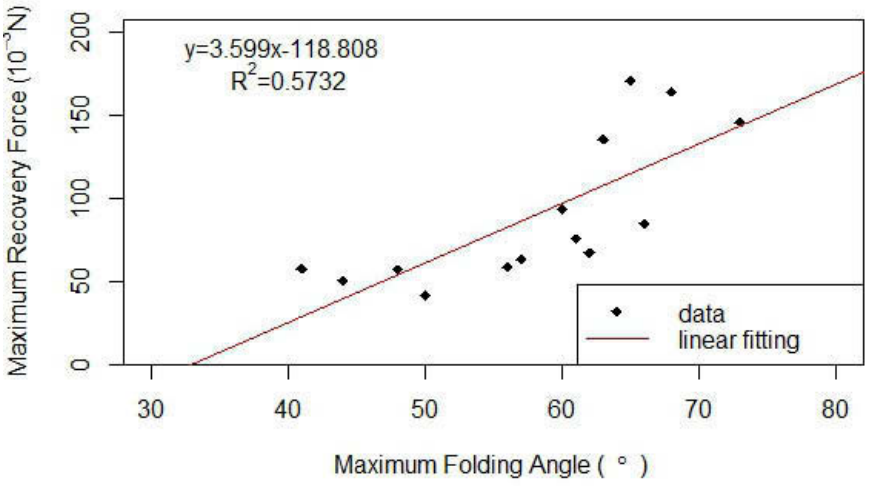

(a)

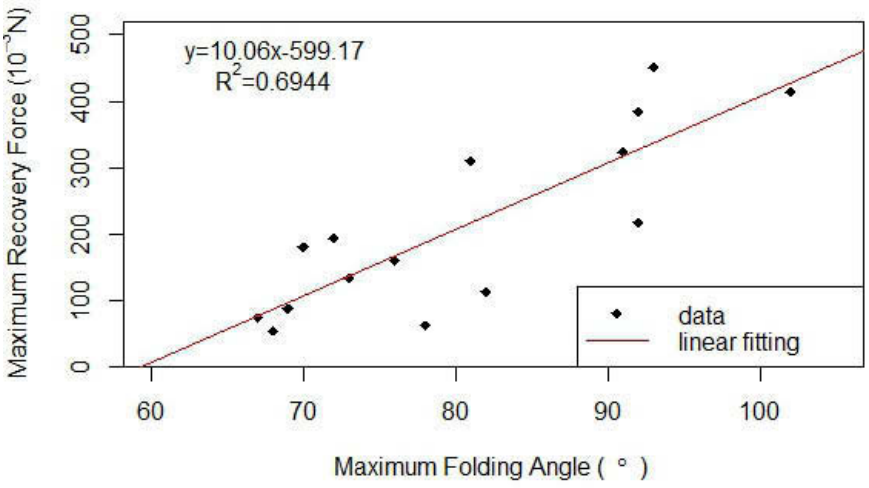

(b)

Figure 5.13: The maximum recovery force versus the maximum non-predetermined folding angle for actuators with thickness ratios of 0.2 (a) and 0.5 (b).

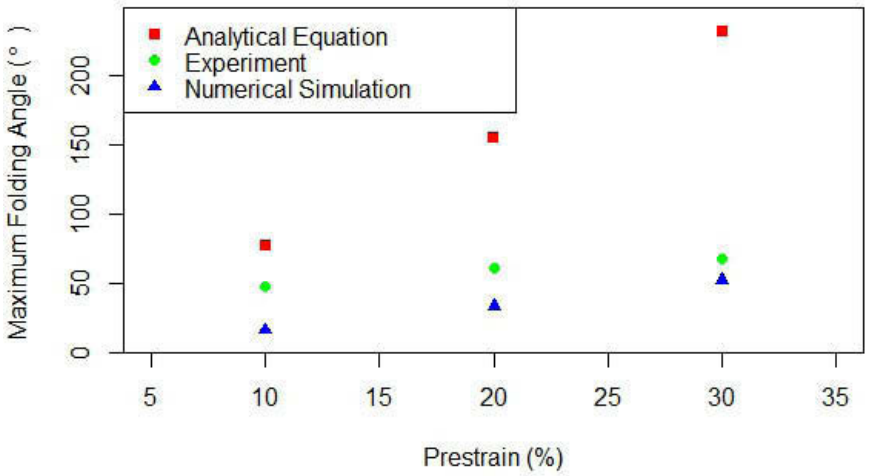

(a)

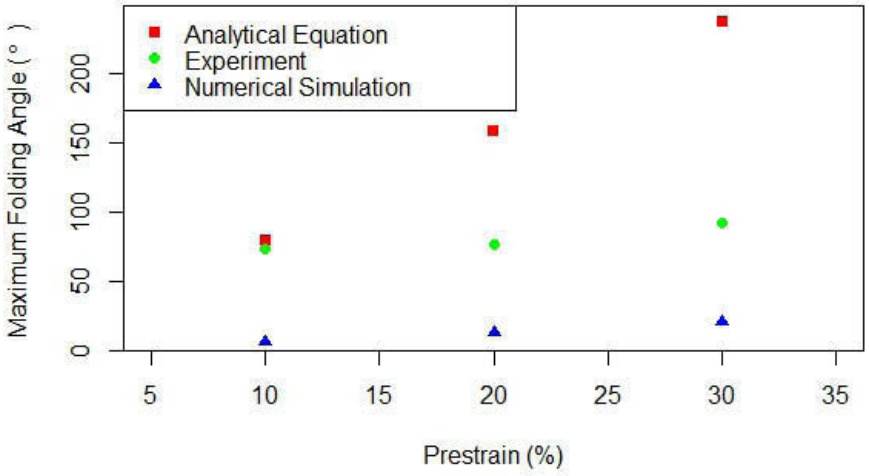

(b)

Figure 5.14: The maximum non-predetermined folding angle values (obtained via analytical, numerical, and experimental analysis) for actuators with thickness ratios of 0.2 (a) and 0.5 (b).

We did not show the comparison result of recovery force here due to large discrepancy. The discrepancy may result from the limitations of the analytical model related to bending beams introduced in Section 2.3. The model is based on a small deflection assumption and linear elasticity while in the real experiment, the folding angle θ is large ($>40°$) and shape memory polymer is not a linear elastic material.

5.4 Conclusion of the Chapter

In this chapter, we described the detailed sample characterization methods, including apparatus and procedures, of the maximum non-predetermined folding angle and recovery force of our actuators. The characterization results indicate that both maximum recovery force and folding angle would increase with the increase of the thickness ratio and prestrain, which agrees with the prediction we can make from equation 2.7 and the trend shown in Figure 2.11. We also compared the maximum non-predetermined folding angle values obtained via analytical equation, numerical simulation, and experimental analysis. Based on the comparison, we can validate the hypothesis in Chapter 2 that the maximum non-predetermined folding angle of the actuator can be tuned by adjusting the thickness ratio between two layers and their prestrain. In addition, we validated another hypothesis that the maximum recovery force was positively correlated to the maximum non-predetermined folding angle.

Chapter 6

The Performance of the Transformer Robot Based on Bidirectional Actuators

In this chapter, we will present the practical application of the bilayer SMPC actuators, that is, by making a self-folding transformer robot which can self-fold from 2D sheet into 3D configuration and then transform between different 3D shapes with the help of the actuators. The robot will also present its practical application including self-navigation task such as obstacle avoidance. We will use the actuator with thickness ratio of 0.5 and prestrain 30% since it can provide us with the maximum folding angle as well as recovery force (over 0.3 N, as shown in Figure 5.4) according to the characterization results.

6.1 Inspiration: Transformer Robot

As we discussed before, the advantages of our actuator over other similar actuators are that it is low-cost, easy-to-fabricate and can realize bidirectional folding movement with adjustable folding angles. In order to show an innovative practical application of the bidirectional folding ability of the actuator, we have investigated a transformer robot that would first self-fold from a 2D base into a 3D boat and then transform into a 3D car. To realize this goal, we need to design a 2D base with specific crease pattern so that SMPC actuators attached to the creases can activate the folding action. Other necessary electronic parts such as batteries, motors and microcontroller would be mounted on the 2D base as well. The activation of the actuators would be achieved by Joule heating, and the navigation of robot during its car state would be controlled by the open-source microcontroller, Arduino.

6.2 Robot Assembly

6.2.1 Design of Crease Patterns

Origami is the concept based on which we designed our crease pattern on the 2D base. The crease pattern needs to be carefully designed to fold the 2D base into the desired 3D shapes. In order to simplify the design and fabrication processes, our desired 3D configurations were tentatively set to car and boat, with the corresponding

2D crease pattern shown in Figure 6.1a.

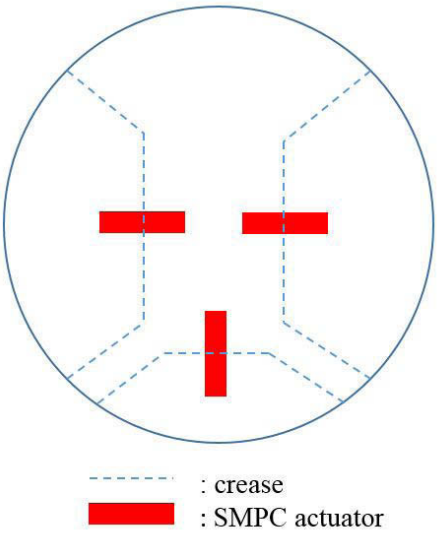

(a)

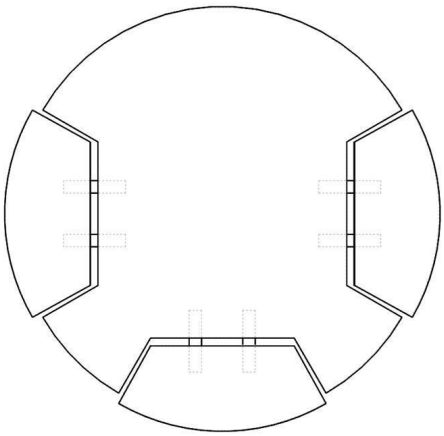

(b)

Figure 6.1: The 2D base that is not separated (a) and the separated 2D base (b). The 2D base must be separated in order not to interfere the folding action of SMP composite actuators. The actuators were attached to the bottom of the base and were denoted by dotted lines. (Image credit: Lichen Fang)

In order to realize the folding action of the 2D base, we attached our SMP composite actuators to the creases on the 2D base and used Joule heating to activate the

actuators. After several initial trials, we found that there must exist gaps between creases, resulting the 2D base separated instead of a whole part, considering the actuators would shrink during the folding process. The width of the gap should be no less than 6 mm (30% prestrain of 18 mm length equals 5.4 mm) to guarantee that the stored strain energy inside SMPC can be released completely. Thus, we cut the 2D base into several parts, as shown in Figure 6.1b. Here SMPC actuators were attached to the bottom of the base and would act as bridges to connect separated parts together. As we mentioned before, we will use the actuator with thickness ratio 0.5 and prestrain 30% since it can provide us with the maximum recovery force according to the characterization results in Chapter 5. The Figure 6.2 shows the anticipated folding and transformation process of the transformer.

The anticipated transformation process is described as follows:

- The transformer starts with the 2D base with actuators attached, as shown in Figure 6.2a. One wheel and one gear motor will be mounted on both left and right wings, and one propeller and one gear motor will be mounted on the tail part, which are not shown in the figure.

- The left and right wings fold upward whereas the tail part folds downward via the attached actuators so that the propeller can immerse into water, resulting the boat state of the transformer, as shown in Figure 6.2b.

- The left and right wings fold downward so that the wheels (not shown in figure)

attached on the two wings can touch the ground, whereas the tail part folds upward via the bidirectional folding ability of the actuators, resulting the car state of the transformer, as shown in Figure 6.2c.

6.2.2 Base Design and Fabrication

Based on the crease pattern design and anticipated transformation process above, we need to figure out suitable materials for base fabrication. The requirements of the materials are light weight and stiff considering the relatively low recovery force of the actuator and the weight of electronic components on the base. After several trials, we decided to use common hard copy paper covered by cured PDMS as the material for base fabrication. As shown in Figure 6.3, we cut the cured PDMS with embedded hard copy paper into four parts: one foundation, two wings and one tail. The wing and tail parts would fold up and down via bidirectional folding actuators during the transformation process whereas the foundation part would keep its flat configuration. The fabrication process is illustrated in Figure 6.3. The Table 6.1 lists the weight of each part.

Foundation	Left Wing	Right Wing	Tail
40 g	5.1 g	5.6 g	4.7 g

Table 6.1: The weight of each separated part of the base.

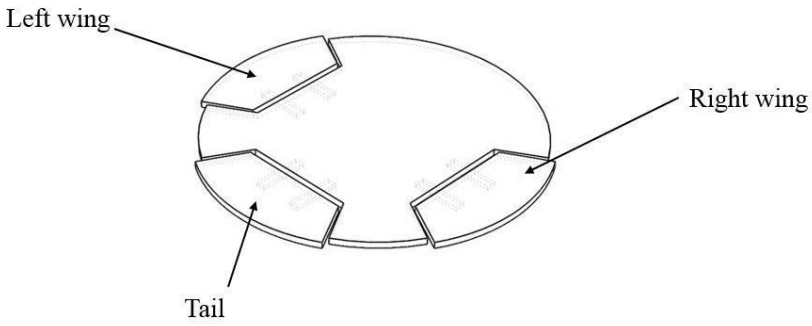

(a)

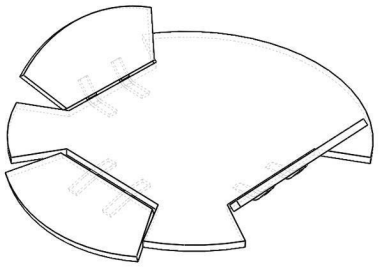

(b)

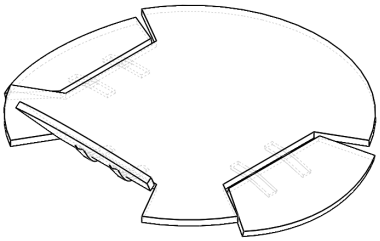

(c)

Figure 6.2: The anticipated transformation process of the transformer. The original 2D base (a), the boat state (b) and the car state (c) of the transformer. (Image credit: Lichen Fang)

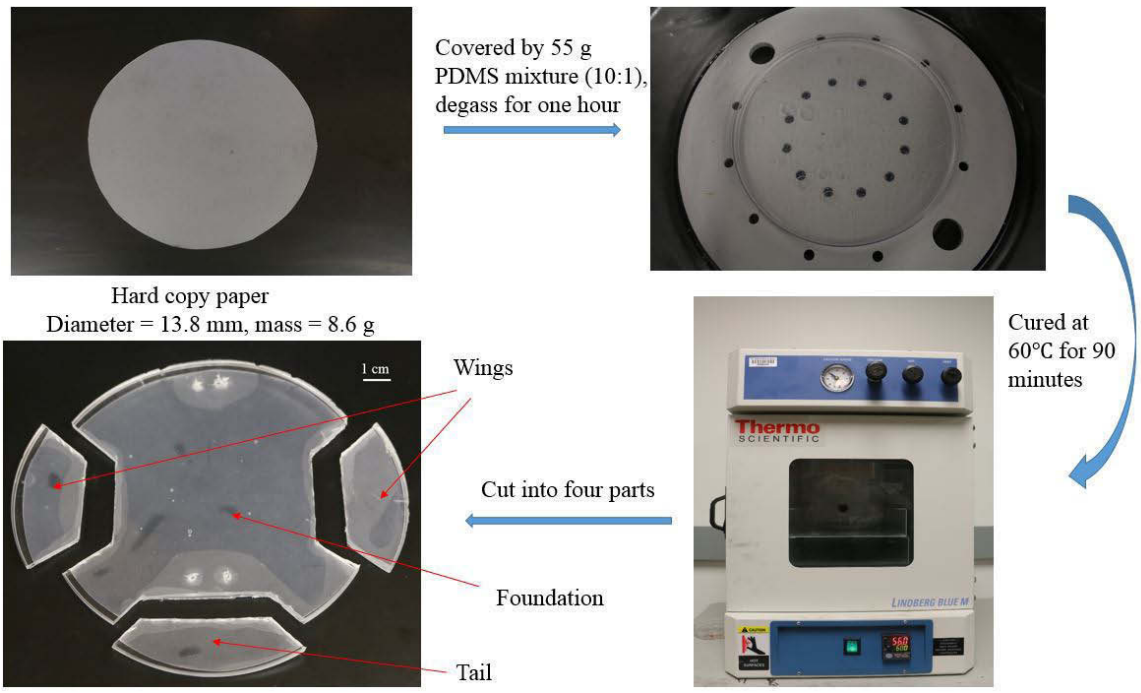

Figure 6.3: Base fabrication process.

6.2.3 Assembly Process

Besides the fabricated base, there are additional necessary components for the complete assembly of the robot: electronics such as sensors, motors, microcontroller and motor shield, etc., and mechanical parts such as screws, nuts, and caster wheels, etc. Refer to Appendix B for the key components inventory for robot assembly. We also 3D printed a propeller, connected with a gear motor and mounted them on the tail part to provide driving force during the boat state of the robot. Refer to Appendix C for the CAD model we used for the 3D printing of the propeller. We fixed the ultrasonic sensor, mini breadboard, Arduino and motor shield on the foundation part whereas we mounted the three gear motors, wheels, and the propeller on wing and

tail parts, respectively.

In order to connect two wing parts and one tail part with the foundation part and guarantee the SMP composite actuators could provide enough force to lift wing and tail parts up and down, we used three groups of actuators with two for each group. The selected SMPC actuators have thickness ratio 0.5 and prestrain 30% since this kind of actuator would provide more than 0.3 N (about 30 grams) recovery force, which is higher than the weight of each part plus the gear motor and wheel/propeller.

Figure 6.4 and Table 6.2 show the robot after assembly and its physical information. We attached two caster wheels to the bottom of the robot to help the robot with the rotational movement, which were not shown in the figure.

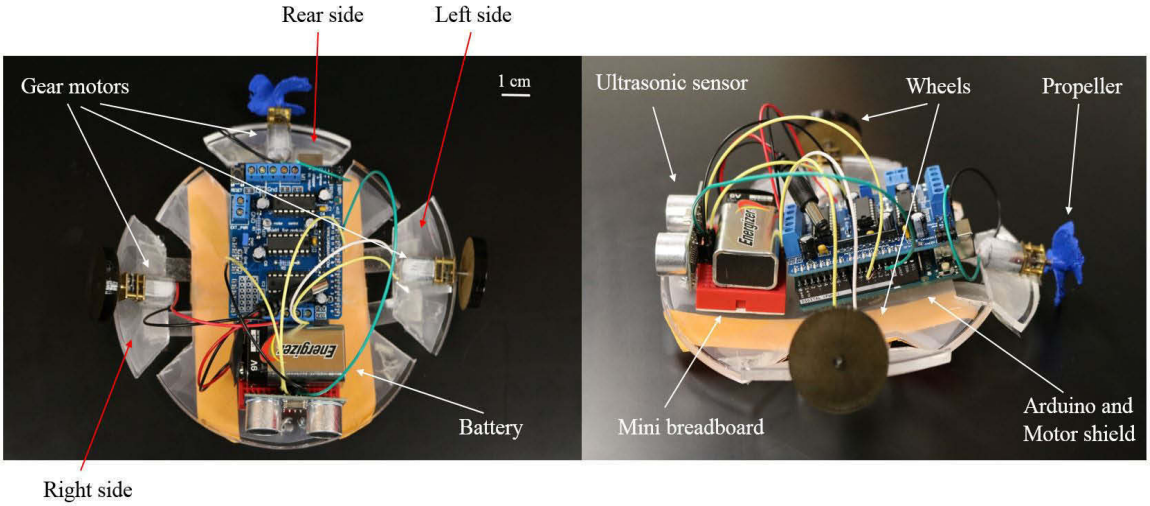

Figure 6.4: The robot after assembly.

Dimension (W*L) (cm)	Left Side (g)	Right Side (g)	Rear Side (g)	Foundation (g)
18*17	21.2	22.4	17.5	143.7

Table 6.2: Physical characteristics of the robot after assembly.

6.3 Robot Performances

In this section we will present the performances of the robot in self-folding and transformation, as well as obstacle avoidance during the car state. Arduino mounted on the robot would be used as the controller to realize the robot navigation.

6.3.1 Self-Folding and Transformation

In order to activate the folding action, we used Arduino 5V output pin and a 5 Ω resistor as a heating element. Initially we decided to attach resistor onto SMP composite directly to provide heat considering SMP is not a good heat conductor. However, the actuator could not provide enough recovery force if attaching resistor directly onto it since SMP would become very soft when ambient temperature is much higher than its glass transition temperature. Also, considering that the resistor is kind of one localized heating element (small size compared to actuator) but the stored strain energy is distributed into the whole stretch area, thus attaching the resistor onto the SMP composite directly cannot release the stored strain energy thoroughly. In addition, the attachment of resistor may interfere the folding of SMP.

Based on the discussion above, the key is to provide a relatively high temperature

"globally". After several trials, one dependable method is to hold the resistor close to the actuator without physical contact and "scan" the stretched part. Considering the power that Arduino can provide is limited and the high number of the actuators, external power source is necessary besides Arduino such as a portable heater. We need to carefully adjust the distance from the heater to the robot to get the desired temperature.

Figures 6.5 and 6.6 illustrated the transformation process from the 2D base into a 3D boat via the activation method described above, and the front and lateral views of the boat, respectively. The "boat state" configuration was realized by the folding upward of both left side and right side, and folding downward of the rear side sequentially. In this configuration, the rear side folded downward so that the propeller can contact water and provide propulsion to move the boat. However, in our experiments we found it was hard to provide enough buoyant force to support the weight of the robot (204.8 g in total) so that we did not show the movement of the boat here.

Then, we continued activating the SMPC actuators to achieve the "car state" as shown in Figure 6.7. In this configuration, both the left side and right side folded downward so that the two wheels can contact the ground, whereas the rear side folded up so that the propeller would not interfere the movement of the car.

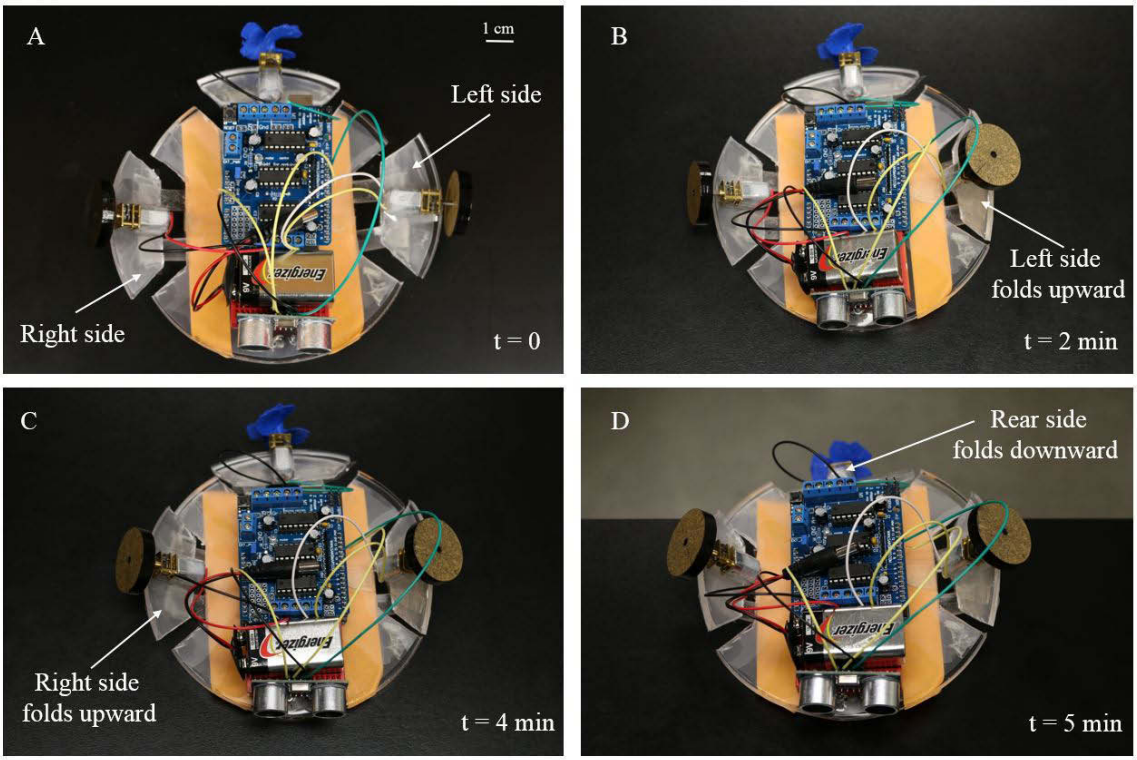

Figure 6.5: The transformation process from the 2D base into a 3D boat. (A) The original 2D base. (B) The left side folds upward. (C) The right side folds upward. (D) The rear side folds downward.

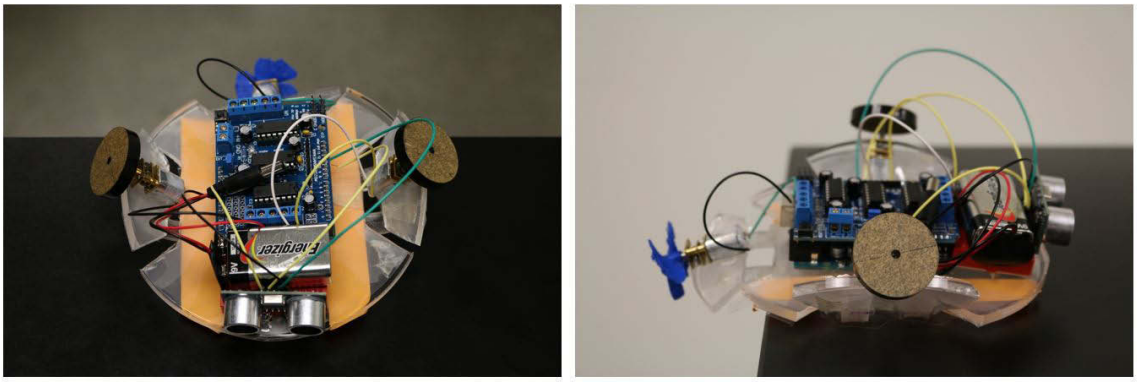

Figure 6.6: *left* The front view of the "boat state" of the robot. *right* The lateral view of the "boat state" of the robot.

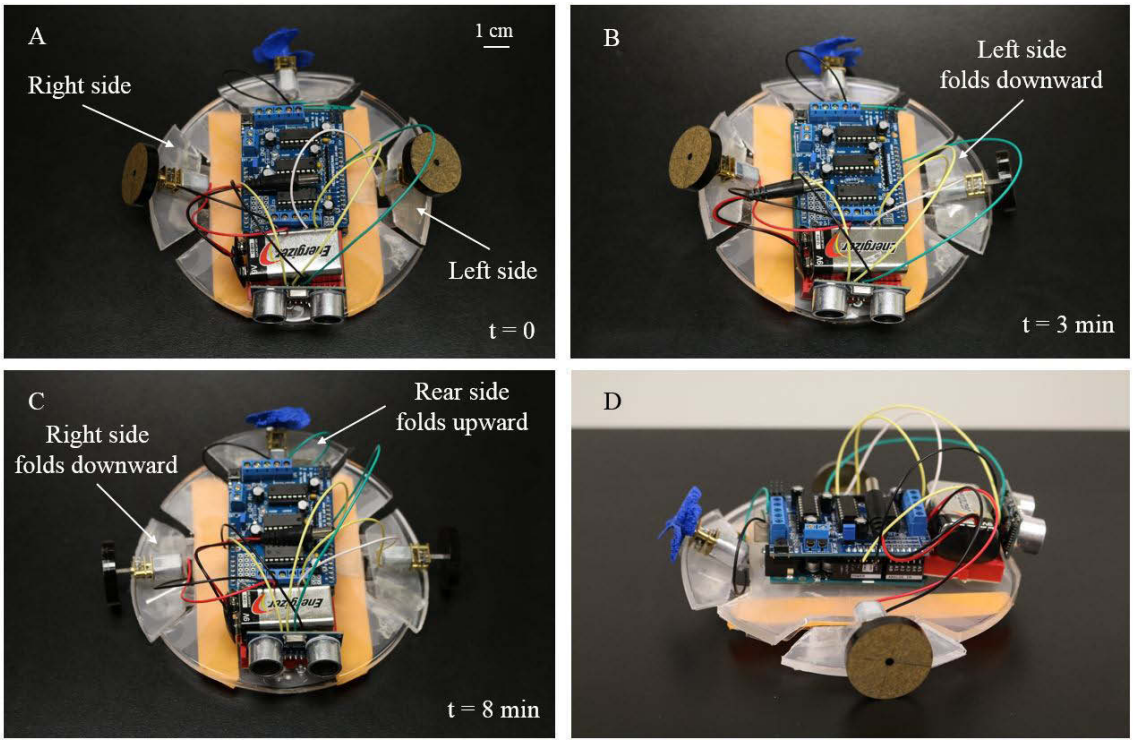

Figure 6.7: The transformation process from the boat into a car. (A) The boat state. (B) The left side folds downward. (C) The right side folds downward whereas the rear side folds upward. (D) The lateral view of the "car state" of the robot.

6.3.2 Obstacle Avoidance

After achieving the "car state", we will present one practical application example of the robot car by controlling the robot to do obstacle avoidance. Obstacle avoidance is a means of navigating a robot in an environment without colliding with surrounding objects. The sonar (HC-SR04 Ultrasonic Sensor) mounted on the robot detects the distance between itself and the obstacles in front of the robot. If the distance is less than 15 centimeters, the microcontroller will control the robot to:

- First move backward for 0.5 s.

- Turn left for 0.5 s and measure distance of the obstacles in front of it.
- Turn right for 1 s and measure distance of the obstacles in front of it.
- Choose the better way to move forward.

Figure 6.8 illustrated one cycle of the obstacle avoidance process described above. Three obstacles were involved in this environment: obstacle A (the air tap), obstacle B (the wall) and obstacle C (on the right side but not shown in the figure). At $t =$ 0.5 s, the robot detected obstacle B within 15 centimeters distance in front of itself and would move backward for 0.5 s. Then at $t = 1$ s, it turned left for 0.5 s and right for 1 s sequentially and measured the corresponding distance from obstacles A and C to itself (d_A and d_C), and it turned left back at $t = 3.5$ s and moved forward to start another cycle because d_A is bigger than d_C. Refer to Appendix D for the code to achieve the obstacle avoidance.

6.4 Conclusion of the Chapter

In this chapter, we showed one practical application example of the bidirectional folding actuators by making a robot that can fold itself from a 2D sheet into different 3D configurations controlled by one microcontroller mounted on the robot. The robot can actively conduct obstacle avoidance controlled by the microcontroller Arduino. We also validated our choice of actuators and the characterization results in Chapter

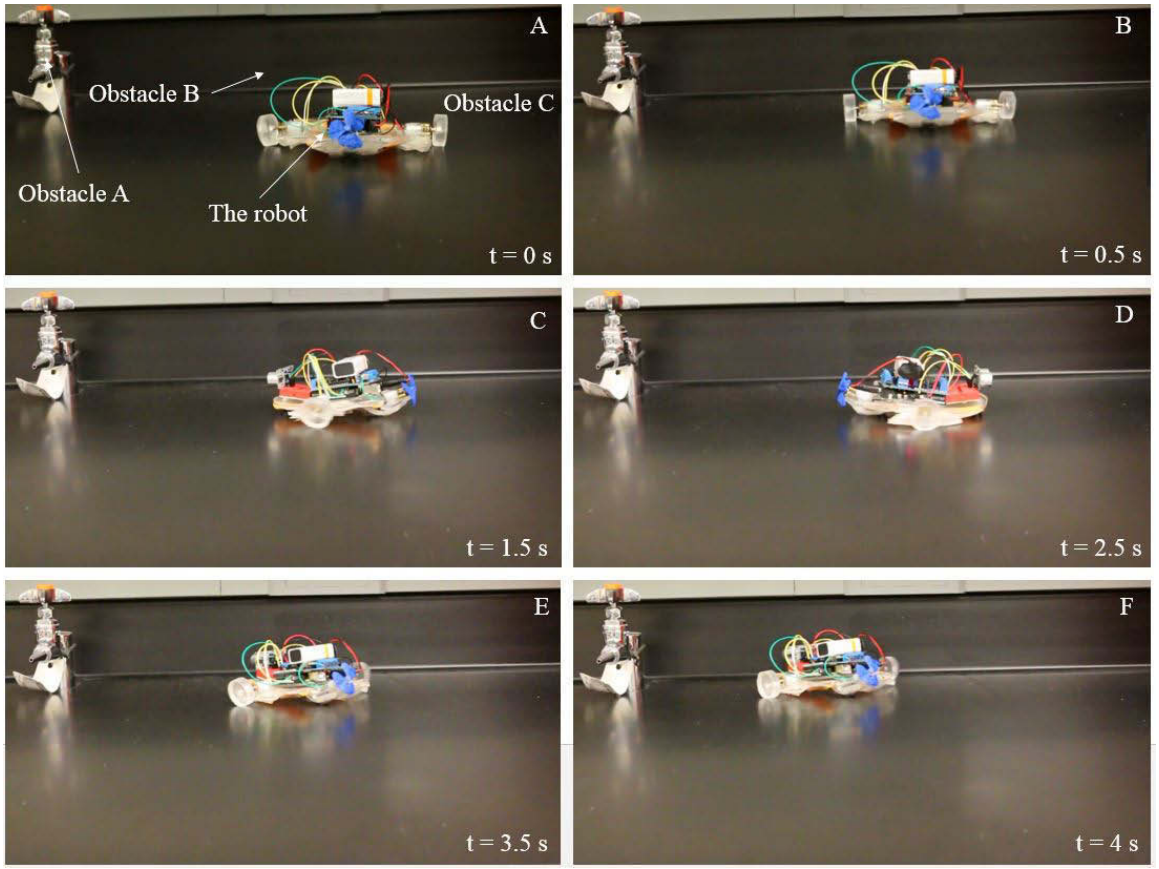

Figure 6.8: The obstacle avoidance performance of the robot. (A) The robot moves forward. (B) The robot starts to move backward. (C) The robot turns left for 0.5 s and measures the distance from obstacle A to itself (d_A). (D) The robot turns right for 1 s and measures the distance from obstacle C to itself (d_C). (E) The robot turns left back after comparing d_A and d_C. (F) The robot moves forward to enter another obstacle avoidance judgment cycle.

5 by showing that the actuators could provide enough force to lift wings and tail parts up and down. We can further explore the potential of the applicability of the actuators in the future, as well as the application of the transformer robot after assembly.

However, there also exists space for improvement. For instance, we can explore better material candidates for the base fabrication and more complex crease patterns

to produce highly complex 3D shapes. Also we can design more advanced structures to provide enough buoyant force to support the robot. In addition, it is possible that we can produce higher recovery force using the SMPC actuators with higher prestrain (more than 30%). All of these and other potential future work would be discussed in next chapter.

Chapter 7

Conclusions and Future Work

In this thesis we reported a novel bidirectional folding actuator based on shape memory polymer (SMP) composite for the self-folding and its application for a transformer robot. The actuator could realize bidirectional folding with adjustable angles (could reach over 90°) and has advantages over other bidirectional folding actuators in the sense that it is easy-to-fabricate and low-cost. We characterized two important properties of the actuator-the maximum recovery force and the folding angle. The characterization results indicate that both maximum recovery force and the folding angle would increase with the increase of the thickness ratio (η) between two SMP layers and prestrain (ε). In order to show the bidirectional folding ability and explore the applicability of this actuator, we introduced a self-folding transformer robot which could self-fold from 2D base to a 3D boat, then transform from a boat to a car and conduct obstacle avoidance.

Two parallel tracks are suggested for the future work: one for scientific research and the other for applications. The first track can investigate how to improve the properties of the actuator such as reversibility and conductivity. In our current design, the stored strain energy inside the actuator would be lost after folding. As a result, the actuator cannot be used repeatedly unless stretching is exerted again, which hinders its further application. So, the next step can be to come up with more advanced designs which could realize repeatable bidirectional folding without stretching repeatedly. Also, we can make composites by combination of shape memory polymers and other materials to improve the properties of the actuator. For example, in our experiment, we used resistor as the heating element, which would introduce complexity in design and assembly. Thus, it would be promising to fabricate SMP/carbon nanotubes (CNTs) composite with low resistance value so that no external heating element is needed. We can also fabricate SMP/fibers composite to increase the stiffness and recovery force of the actuator. Furthermore, the current analytical model assumes linear elastic material model while SMP follows a hyperelastic material model. For more accurate prediction, we need to improve our model by using more advanced material model.

The second track can further explore the applicability of the actuator. The novelty of the actuator is its bidirectional folding ability. We reported one self-folding transformer robot to present this ability. We believe more complex 3D objects can be made by designing more complex crease patterns. Although we only showed the

navigation (obstacle avoidance) of the robot after assembly in this thesis, more complex navigation tasks such as Simultaneous Localization and Mapping (SLAM)[60] can be conducted. So, the application of the robot after assembly is also worthwhile to be further explored.

This work can be regarded as a combination of findings from polymer science and robotics. We envision that our bidirectional actuator-based robot can provide new opportunities for various applications by enabling transformation and self-navigation so that a robot can change its shape and movement depending on the surrounding environments.

Bibliography

[1] F. Haas and R. J. Wootton, "Two basic mechanisms in insect wing folding," *Proceedings of the Royal Society of London B: Biological Sciences*, vol. 263, no. 1377, pp. 1651–1658, 1996.

[2] H. Kobayashi, B. Kresling, and J. F. V. Vincent, "The geometry of unfolding tree leaves," *Proceedings of the Royal Society B: Biological Sciences*, vol. 265, no. 1391, pp. 147–154, 1998.

[3] P. Todd, "A geometric model for the cortical folding pattern of simple folded brains," *Journal of theoretical biology*, vol. 97, no. 3, pp. 529–538, 1982.

[4] M. T. Tolley, S. M. Felton, S. Miyashita, D. Aukes, D. Rus, and R. J. Wood, "Self-folding origami: shape memory composites activated by uniform heating," *Smart Materials and Structures*, vol. 23, no. 9, p. 094006, 2014.

[5] D. E. D and D. M. L, "Recent results in computational origami," *Proc. of the 3rd Int. Meeting of Origami Science, Math, and Education*, pp. 3–16, 2001.

[6] R. J. Lang, "The science of origami," *Physics World*, vol. 20, no. 2, p. 30, 2007.

[7] [Online]. Available: https://www.youtube.com/watch?v=30Lv8JjCqhU

[8] S. Felton, M. Tolley, E. Demaine, D. Rus, and R. Wood, "A method for building self-folding machines," *Science*, vol. 345, no. 6197, pp. 644–646, 2014.

[9] X. Guo, H. Li, B. Yeop Ahn, E. B. Duoss, K. J. Hsia, J. A. Lewis, and R. G. Nuzzo, "Two- and three-dimensional folding of thin film single-crystalline silicon for photovoltaic power applications," *Proceedings of the National Academy of Sciences*, vol. 106, no. 48, pp. 20 149–20 154, 2009.

[10] J. Rogers, Y. Huang, O. G. Schmidt, and D. H. Gracias, "Origami mems and nems," *MRS Bulletin*, vol. 41, pp. 123–129, 2 2016.

[11] E. Gultepe, S. Yamanaka, K. E. Laflin, S. Kadam, Y. Shim, A. V. Olaru, M. A. Khashab, A. N. Kalloo, D. H. Gracias, and F. M. Selaru, "Biologic tissue sampling with untethered microgrippers," *Gastroenterology*, vol. 144, no. 4, pp. 691–693, 2013.

[12] S. Miyashita, L. Meeker, M. T. Tolley, R. J. Wood, and D. Rus, "Self-folding miniature elastic electric devices," *Smart Materials and Structures*, vol. 23, no. 9, p. 094005, 2014.

[13] Wikipedia. James webb space telescope. [Online]. Available: https://en.wikipedia.org/wiki/James_Webb_Space_Telescope

[14] D. H. Gracias, "Stimuli responsive self-folding using thin polymer films," *Biological engineering / Materials engineering*, vol. 2, no. 1, pp. 112–119, 2013.

[15] Y. Yi and C. Liu, "Magnetic actuation of hinged microstructures," *Microelectromechanical Systems, Journal of*, vol. 8, no. 1, pp. 10–17, 1999.

[16] N. Bassik, G. M. Stern, and D. H. Gracias., "Microassembly based on hands free origami with bidirectional curvature," *Applied Physics Letters*, vol. 95, no. 9, p. 091901, 2009.

[17] E. Hawkes, B. An, N. M. Benbernou, H. Tanaka, S. Kim, E. D. Demaine, D. Rus, and R. J. Wood, "Programmable matter by folding," *Proceedings of the National Academy of Sciences*, vol. 107, no. 28, pp. 12 441–12 445, 2010.

[18] B. An, N. Benbernou, E. D. Demaine, and D. Rus, "Planning to fold multiple objects from a single self-folding sheet," *Robotica*, vol. 29, pp. 87–102, 2011.

[19] B. An and D. Rus, "Programming and controlling self-folding robots," *2012 IEEE International Conference on Robotics and Automation*, 2012.

[20] Y. Liu, J. K. Boyles, J. Genzer, and M. D. Dickey, "Self-folding of polymer sheets using local light absorption," *Soft Matter*, vol. 8, no. 6, pp. 1764–1769, 2011.

[21] Y. Mao, K. Yu, M. S. Isakov, J. Wu, M. L. Dunn, and H. J. Qi, "Sequential self-folding structures by 3D printed digital shape memory polymers," *Scientific Reports*, vol. 5, no. 13616, 2015.

[22] E. M. Ahmed, "Hydrogel: Preparation, characterization, and applications: A review," *Journal of Advanced Research*, vol. 6, no. 2, pp. 105–121, 2015.

[23] J. Guan, H. He, D. J. Hansford, and L. J. Lee, "Self-folding of three-dimensional hydrogel microstructures," *The Journal of Physical Chemistry*, vol. 109, no. 49, pp. 23 134–23 137, 2005.

[24] F. Carpi, D. D. Rossi, R. Kornbluh, R. Pelrine, and P. Sommer-Larsen, *Dielectric Elastomers as Electromechanical Transducers: Fundamentals, Materials, Devices, Models and Applications of an Emerging Electroactive Polymer Technology*. Elsevier Science, 2008.

[25] Z. Suo, "Theory of dielectric elastomers," *Acta Mechanica Solida Sinica*, vol. 23, no. 6, pp. 549–578, 2010.

[26] S. Shian, K. Bertoldi, and D. R. Clarke, "Dielectric elastomer based grippers for soft robotics," *Advanced Materials*, vol. 27, no. 43, pp. 6814–6819, 2015.

[27] J. Shintake, S. Rosset, B. Schubert, D. Floreano, and H. Shea, "Versatile soft grippers with intrinsic electroadhesion based on multifunctional polymer actuators," *Advanced Materials*, vol. 28, no. 2, pp. 231–238, 2016.

[28] S. E. Bakarich, I. Gorkin, M. Panhuis, and G. M. Spinks, "4D printing with mechanically robust, thermally actuating hydrogels," *Macromolecular rapid communications*, vol. 36, pp. 1211–1217, 2015.

[29] E. J. Pei, "4D printing: dawn of an emerging technology cycle." *Assembly Automation*, vol. 34, pp. 310–314, 2014.

[30] Q. Ge, C. K. Dunn, H. J. Qi, and M. L. Dunn, "Active origami by 4D printing," *Smart Materials and Structures*, vol. 23, no. 9, p. 094007, 2014.

[31] T. Chung, A. Romo-Uribe, and P. T. Mather, "Two-way reversible shape memory in a semicrystalline network," *Macromolecules*, vol. 41, pp. 184–192, 2008.

[32] M. Bothe and T. Pretsch, "Two-way shape changes of a shape-memory poly(ester urethane)," *Macromolecular Chemistry and Physics*, vol. 213, no. 22, pp. 2378–2385, 2012.

[33] J. K. Paik and R. J. Wood, "A bidirectional shape memory alloy folding actuator," *Smart Materials and Structures*, vol. 21, no. 6, p. 065013, 2012.

[34] Q. Ge, K. K. Westbrook, P. T. Mather, M. L. Dunn, and H. J. Qi, "Thermomechanical behavior of a two-way shape memory composite actuator," *Smart Materials and Structures*, vol. 22, no. 5, p. 055009, 2013.

[35] M. Behl, K. Kratz, J. Zotzmann, U. Nchel, and A. Lendlein, "Reversible bidirectional shape-memory polymers," *Advanced Materials*, vol. 25, no. 32, pp. 4466–4469, 2013.

[36] C. Li, A. O. Pullin, D. W. Haldane, H. K. Lam, R. S. Fearing, and R. J. Full, "Terradynamically streamlined shapes in animals and robots enhance traversabil-

ity through densely cluttered terrain," *Bioinspiration Biomimetics*, vol. 10, no. 4, p. 046003, 2015.

[37] R. Wood, S. Avadhanula, M. Menon, and R. Fearing, "Microrobotics using composite materials: the micromechanical flying insect thorax," in *Robotics and Automation. Proceedings. ICRA '03. IEEE International Conference*, vol. 2, 2003, pp. 1842–1849.

[38] G. Dudek, M. Jenkin, C. Prahacs, A. Hogue, J. Sattar, P. Giguere, A. German, H. Liu, S. Saunderson, A. Ripsman, S. Simhon, L.-A. Torres, E. Milios, P. Zhang, and I. Rekletis, "A visually guided swimming robot," in *Intelligent Robots and Systems*, 2005, pp. 3604–3609.

[39] S. Felton, M. Tolley, C. Onal, D. Rus, and R. Wood, "Robot self-assembly by folding: A printed inchworm robot," in *Robotics and Automation (ICRA), 2013 IEEE International Conference on*, 2013, pp. 277–282.

[40] S. Miyashita, C. D. Onal, and D. Rus, "Multi-crease self-folding by global heating," *Artificial Life*, vol. 21, pp. 398–411, 2015.

[41] P. White and M. Yim, "Scalable modular self-reconfigurable robots using external actuation," in *Intelligent Robots and Systems. IROS 2007. IEEE/RSJ International Conference*, 2007, pp. 2773–2778.

[42] S. Miyashita, S. Guitron, M. Ludersdorfer, C. R. Sung, and D. Rus, "An unteth-

ered miniature origami robot that self-folds, walks, swims, and degrades," *2015 International Conference on Robotics and Automation*, 2015.

[43] J. Kim, J. A. Hanna, M. Byun, C. D. Santangelo, and R. C. Hayward, "Designing responsive buckled surfaces by halftone gel lithography," *Science*, vol. 335, no. 6073, pp. 1201–1205, 2012.

[44] D. P. Holmes, M. Roch, T. Sinha, and H. A. Stone, "Bending and twisting of soft materials by non-homogenous swelling," *Soft Matter*, vol. 7, no. 11, pp. 5188–5193, 2011.

[45] D. Gracias, V. Kavthekar, J. Love, K. Paul, and G. Whitesides, "Fabrication of micrometer-scale, patterned polyhedra by self-assembly," *Advanced Materials*, vol. 14, no. 3, pp. 235–238, 2002.

[46] D. Stoeckel, "The shape memory effect-phenomenon, alloys and applications," pp. 1–13, 1995.

[47] Q. Zhao, H. J. Qi, and T. Xie, "Recent progress in shape memory polymer: New behavior, enabling materials, and mechanistic understanding," *Progress in Polymer Science*, vol. 49, pp. 79–120, 2015.

[48] J. K. Paik, E. Hawkes, and R. J. Wood, "A novel low-profile shape memory alloy torsional actuator," *Smart Materials and Structures*, vol. 19, no. 12, p. 125014, 2010.

[49] M. Taya, Y. Liang, O. C. Namli, H. Tamagawa, and T. Howie, "Design of two-way reversible bending actuator based on a shape memory alloy/shape memory polymer composite," *Smart Materials and Structures*, vol. 22, no. 10, p. 105003, 2013.

[50] A. Lendlein and S. Kelch, "Shape-memory polymers," *Angewandte Chemie International Edition*, vol. 41, no. 12, pp. 2034–2057, 2002.

[51] T. Xie and I. A. Rousseau, "Facile tailoring of thermal transition temperatures of epoxy shape memory polymers," *Polymer*, vol. 50, no. 8, pp. 1852–1856, 2009.

[52] H. Tobushi, S. Hayashi, Y. Sugimoto, and K. Date, "Two-way bending properties of shape memory composite with SMA and SMP," *Materials*, vol. 2, no. 3, pp. 1180–1192, 2009.

[53] M. Bothe and T. Pretsch, "Bidirectional actuation of a thermoplastic polyurethane elastomer," *Journal of Materials Chemistry A*, vol. 1, no. 46, pp. 14 491–14 497, 2013.

[54] X. Lan, Y. Liu, H. Lv, X. Wang, J. Leng, and S. Du, "Fiber reinforced shape-memory polymer composite and its application in deployable hinge in space," *Smart Mater. Struct.*, vol. 18, p. 024002, 2009.

[55] C. Liu, H. Qin, and P. T. Mather, "Review of progress in shape-memory polymers," *Journal of Materials Chemistry*, vol. 17, no. 16, pp. 1543–1558, 2007.

[56] W. Riley, L. Sturges, and D. Morris, *Mechanics of Materials*. John Wiley Sons, 2007.

[57] R. Xiao, J. Choi, N. Lakhera, C. M. Yakacki, C. P. Frick, and T. D. Nguyen, "Modeling the glass transition of amorphous networks for shape-memory behavior," *Journal of the Mechanics and Physics of Solids*, vol. 61, no. 7, pp. 1612–1635, 2013.

[58] T. D. Nguyen, C. M. Yakacki, P. D. Brahmbhatt, and M. L. Chambers, "Modeling the relaxation mechanisms of amorphous shape memory polymers," *Advanced Materials*, vol. 22, no. 31, pp. 3411–3423, 2010.

[59] D. L. Safranski and K. Gall, "Effect of chemical structure and crosslinking density on the thermo-mechanical properties and toughness of (meth)acrylate shape memory polymer networks," *Polymer*, vol. 49, no. 20, pp. 4446–4455, 2008.

[60] H. Durrant-Whyte and T. Bailey, "Simultaneous localization and mapping: part i," *IEEE Robotics Automation Magazine*, vol. 13, no. 2, pp. 99–110, 2006.

Appendix A

Matlab Code for Calculating Mean Curvature and Stored Strain Energy of Curved Beam

Note: the code was originally created by Dr. Santiago Orrego.

```
clc
clear all
close all

L=11.4e-2;  % beam length (real in meters)
px=358.2;  % how many pixels per beam length

```

APPENDIX A. MATLAB CODE FOR CALCULATING MEAN CURVATURE AND STORED STRAIN ENERGY OF CURVED BEAM

```
8  I='1_b.png';  % name of image file
9
10 pol=3;  % order of polynomial for regression
11
12 scale=L/px;
13
14 E=0.05119e9;  % Youngs Modulus (Pa)
15 h=1e-3;  % thickness (m)
16 w=12e-3;  % width (m)
17 v=0.3;  % Poisson's ratio
18 Ix=w*h^3/(12);  % inertia
19 B=Ix*E;  % Bendind Stiffness
20
21 % IMAGE PROCESSING
22 A=imread(I);
23 I = im2bw(A);
24
25 figure
26 subplot(2,2,1)
27 imshow(I)
28 axis on
```

```
29 axis tight
30
31 [fil col]=size(I);
32
33 i=fil;
34 j=1;
35 x=[];
36
37 flag=0;
38 flag_end=0;
39 a=1;
40 while flag_end==0
41
42     while flag==0
43
44         if I(i,j)==1
45             x(a)=j;
46             y(a)=fil-i;
47             flag=1;
48             a=a+1;
49         end
```

```
50              if  i==1 &&  I(i,j)==0
51                  flag=1;
52              end
53              i=i-1;
54          end
55
56          flag=0;
57          j=j+1;
58
59          i=fil;
60
61          if  j==col
62              flag_end=1;
63          end
64      end
65
66      y=y';
67      x=x';
68
69      subplot(2,2,2)
70      plot(x,y)
```

```
71
72 % FILTER
73 A=[x  y];
74 [UniXY,Index]=unique(A);
75 DupIndex=setdiff(1:size(A,1),Index);
76 A(DupIndex,:)=[];
77 x=A(:,1);
78 y=A(:,2);
79
80 x=x(:)-min(x);
81 y=y(:)-min(y);
82 x=x*scale;
83 y=y*scale;
84
85 yy=y;
86 y=smooth(x,y);
87 subplot(2,2,2)
88 plot(x*1000,y*1000,x*1000,yy*1000)
89 xlabel('x (mm)')
90 ylabel('y (mm)')
91
```

```
92
93 % FITTING
94 [P S]=polyfit(x,y,pol);  % generate 2th order polynomial
       approximation
95 yp=polyder(P);  % take first/second derivative of
       approximation
96 ypp=polyder(yp);
97
98 ypx=polyval(yp,x);  % evaluate the polynomial at all values
       of x
99 yppx=polyval(ypp,x);
100 ypx2=1+ypx.^2;
101 num=ypx2.^(3/2);
102
103 k=abs(yppx./num);  % find radius of curve at each value of x
104
105 Y = polyval(P,x);
106
107 k1=mean(k);
108
109 subplot(2,2,3);
```

```
110 plot(x*1000,y*1000,x*1000,Y*1000);
111 xlabel('Beam Length (mm)')
112 ylabel('Amplitude (mm)')
113
114 [r2 rmse] = rsquare(y,Y);
115
116 subplot(2,2,4)
117 plot(x*1000,k);
118 xlabel('Beam Length (mm)')
119 ylabel('Curvature (m)')
120
121 kk=k.^2;
122 Es=0.5*B*trapz(x,kk);
123
124 disp(sprintf('Curvature: %.2f',k1));
125 disp(sprintf('Strain Energy:  %8.2E',Es));
126
127
128 function [r2 rmse] = rsquare(y,f,varargin)
129 % Compute coefficient of determination of data fit model and
      RMSE
```

```
130 %
131 % [r2 rmse] = rsquare(y,f)
132 % [r2 rmse] = rsquare(y,f,c)
133 %
134 % RSQUARE computes the coefficient of determination (R-square
        ) value from
135 % actual data Y and model data F. The code uses a general
        version of
136 % R-square, based on comparing the variability of the
        estimation errors
137 % with the variability of the original values. RSQUARE also
        outputs the
138 % root mean squared error (RMSE) for the user's convenience.
139 %
140 % Note: RSQUARE ignores comparisons involving NaN values.
141 %
142 % INPUTS
143 %   Y         : Actual data
144 %   F         : Model fit
145 %
146 % OPTION
```

```
147 %    C        : Constant term in model
148 %               R-square may be a questionable measure of fit
    when no
149 %               constant term is included in the model.
150 %    [DEFAULT] TRUE : Use traditional R-square computation
151 %              FALSE : Uses alternate R-square computation for
    model
152 %                      without constant term [R2 = 1 - NORM(Y-F
    )/NORM(Y)]
153 %
154 % OUTPUT
155 %    R2       : Coefficient of determination
156 %    RMSE     : Root mean squared error
157 %
158 % EXAMPLE
159 %    x = 0:0.1:10;
160 %    y = 2.*x + 1 + randn(size(x));
161 %    p = polyfit(x,y,1);
162 %    f = polyval(p,x);
163 %    [r2 rmse] = rsquare(y,f);
164 %    figure; plot(x,y,'b-');
```

```
165 %    hold on; plot(x,f,'r-');
166 %    title(strcat(['R2 = ' num2str(r2) '; RMSE = ' num2str(
        rmse)]))
167 %
168 % Jered R Wells
169 % 11/17/11
170 % jered [dot] wells [at] duke [dot] edu
171 %
172 % v1.2 (02/14/2012)
173 %
174 % Thanks to John D'Errico for useful comments and insight
        which has helped
175 % to improve this code. His code POLYFITN was consulted in
        the inclusion of
176 % the C-option (REF. File ID: #34765).
177
178 if isempty(varargin); c = true;
179 elseif length(varargin)>1; error 'Too many input arguments';
180 elseif ~islogical(varargin{1}); error 'C must be logical (
        TRUE||FALSE)'
181 else c = varargin{1};
```

```
182 end

183

184 % Compare inputs

185 if ~all(size(y)==size(f)); error 'Y and F must be the same
      size'; end

186

187 % Check for NaN

188 tmp = ~or(isnan(y),isnan(f));

189 y = y(tmp);

190 f = f(tmp);

191

192 if c; r2 = max(0,1 - sum((y(:)-f(:)).^2)/sum((y(:)-mean(y(:))
      ).^2));

193 else r2 = 1 - sum((y(:)-f(:)).^2)/sum((y(:)).^2);

194     if r2<0

195     % http://web.maths.unsw.edu.au/~adelle/Garvan/Assays/
          GoodnessOfFit.html

196         warning('Consider adding a constant term to your
              model') %#ok<WNTAG>

197         r2 = 0;

198     end
```

```
199 end

200

201 rmse = sqrt(mean((y(:) - f(:)).^2));
```

Appendix B

Components for Robot Assembly

The checklist of the key components for robot assembly.

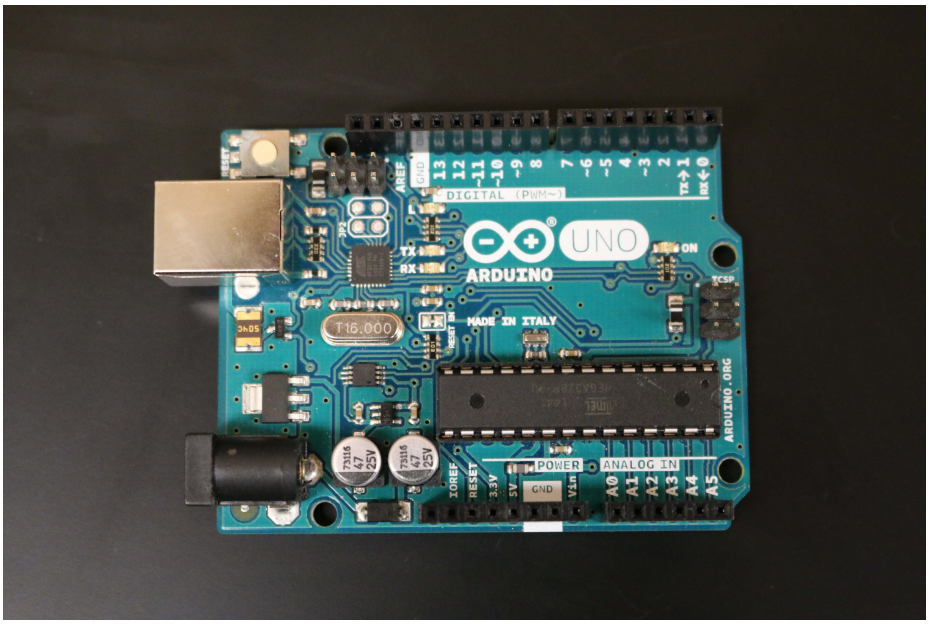

Figure B.1: Arduino Uno R3.

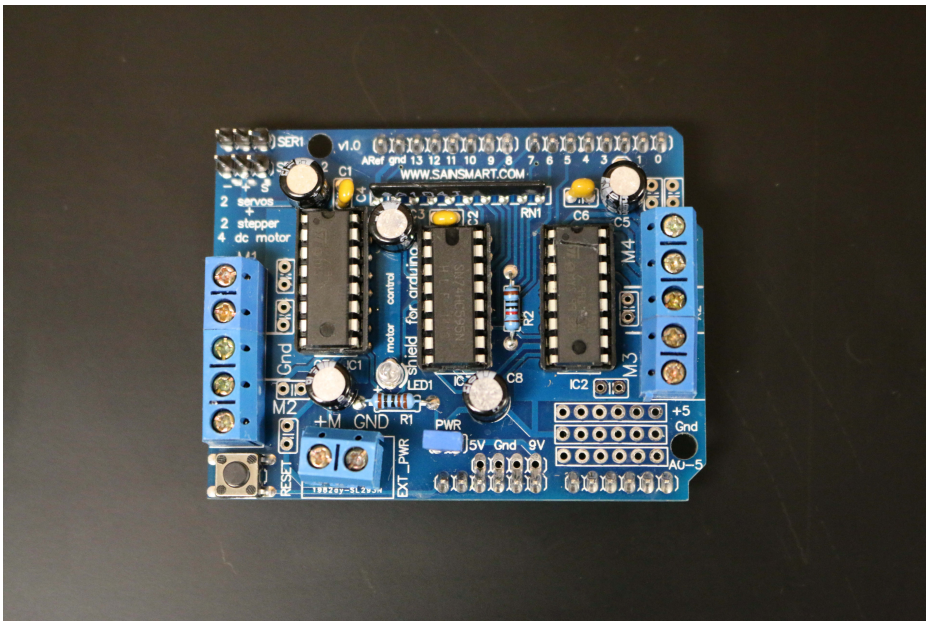

Figure B.2: SainSmart L293D Motor Drive Shield For Arduino Uno.

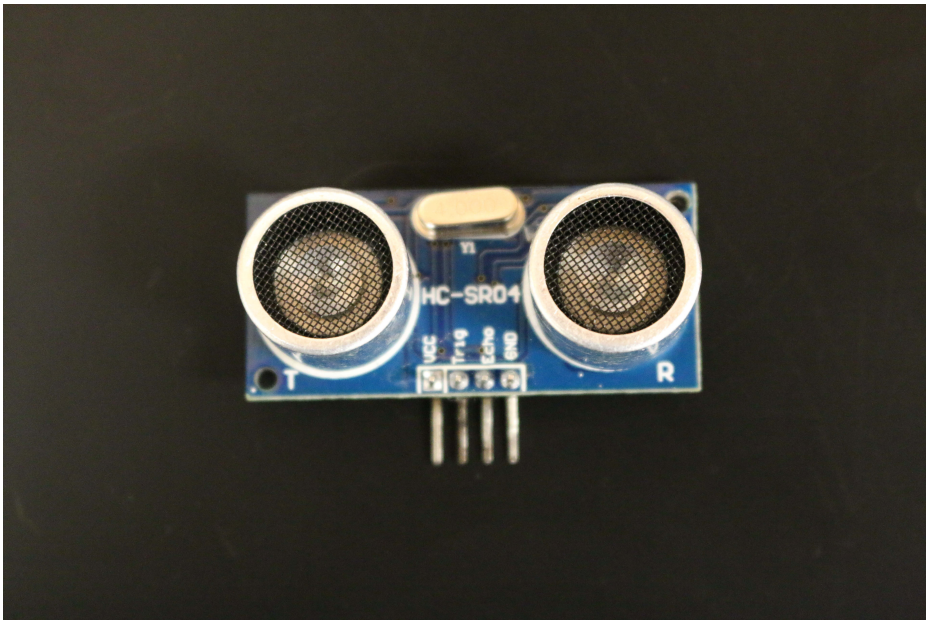

Figure B.3: HC-SR04 Ultrasonic Sensor.

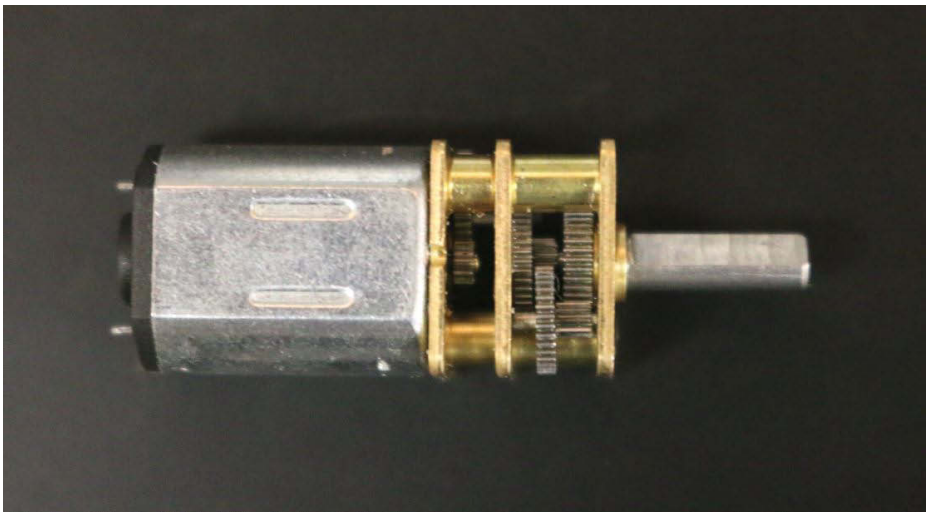

Figure B.4: DC 6V 100RPM Micro Speed Reduction Gear Motor.

Appendix C

3D Printing of a Propeller

- The source model (Figure C.1) was downloaded from *GRABCAD*, an open source CAD model community, and adjusted for our need.
- Then we exported the model into *.stl* format and imported it into *Slic3r* to generate G-code for 3D printing (Figure C.2).
- Finally we imported the generated G-code into *Pronterface* to control the 3D printer to print the propeller (Figure C.3).

Figure C.1: CAD model of the propeller. The diameter of the central hole is 3.6 mm.

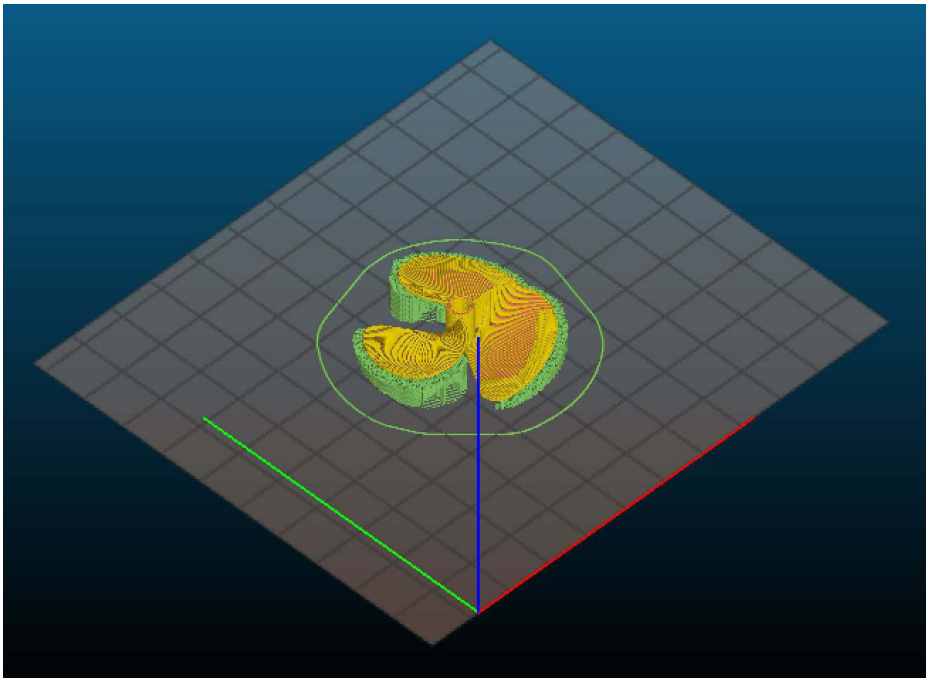

Figure C.2: Import CAD model into *Slic3r* to generate G-code for 3D printing.

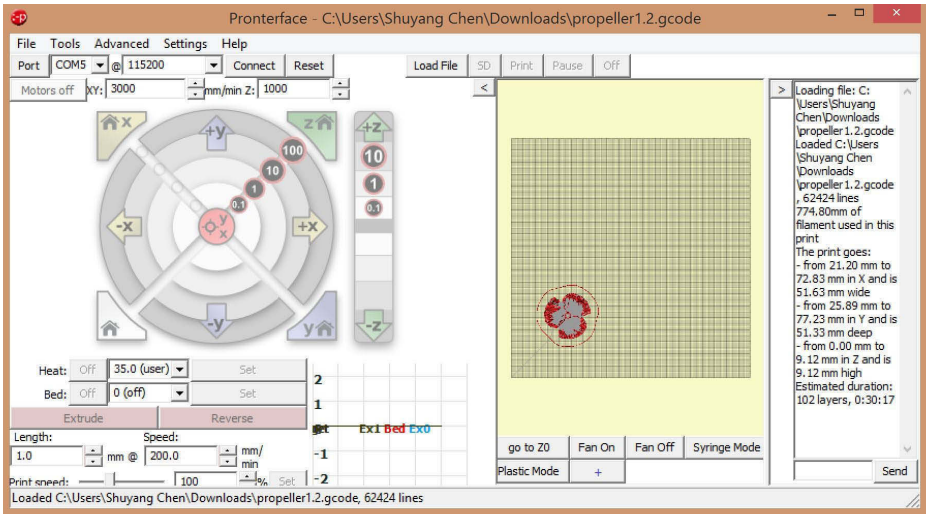

(a) Import G-code into *Pronterface* for printing.

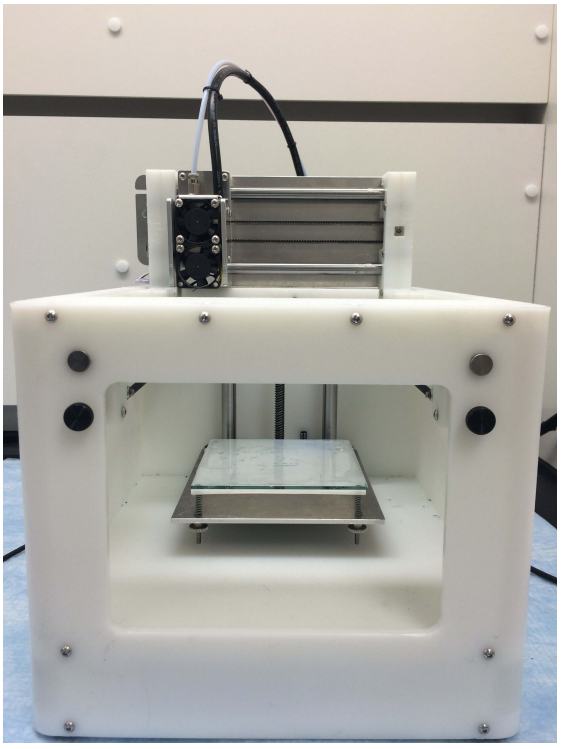

(b) The 3D printer used to print propeller.

Figure C.3: The 3D printer printed the propeller under control of *Pronterface*.

Appendix D

C++ Code for Robot Obstacle Avoidance Using Arduino

```
1  //Shuyang Chen
2
3
4  #include <AFMotor.h>  // load the motor drive library
5  #define trigPin 12  // define trigger pin
6  #define echoPin 13  // define echo pin
7
8    AF_DCMotor motor1(4, MOTOR34_1KHZ);  // create motors with 64KHZ
       PWM
9    AF_DCMotor motor2(3, MOTOR34_1KHZ);
10
11 void setup() {
```

```
12    Serial.begin(9600);
13    Serial.println("Motor test!");
14    pinMode(trigPin, OUTPUT);  // set the pinmode of each pin
15    pinMode(echoPin, INPUT);
16    motor1.setSpeed(200);  // set the speed of motors
17    motor2.setSpeed(200);
18 }
19
20 void loop() {
21    long distance, distance_left, distance_right;
22    distance = get_distance();
23
24 // if the obstacle is within 15 centimeters ahead, do the following
       :
25    if (distance < 15) {
26      Serial.println ("Obstacle detected!" );
27      Serial.print ("Obstacle distance is: " );
28      Serial.print (distance);
29      Serial.print ("cm");
30
31    /*robot will choose a better direction to move on*/
32      Serial.print (" Move back !");
33      move_backward(); // first moveback for 0.5s
34      delay(500);
35
```

```
36      turn_left();
37      delay(500);
38      distance_left = get_distance();
39      Serial.print (distance_left);
40
41      turn_right();
42      delay(1000);
43      distance_right = get_distance();
44      Serial.print (distance_right);
45
46      if(distance_left < distance_right){
47        move_forward();
48      }
49
50      else{
51        turn_left();
52        delay(1000);
53        move_forward();
54      }
55  }
56
57   else{
58      Serial.println ("No obstacle detected, going forward");
59      delay (15);
60      move_forward();
```

```
61    }
62  }
63
64    long get_distance(){
65      long distance_1, travel_time;
66      digitalWrite(trigPin, LOW);
67      delayMicroseconds(2);  // delays are necessary for a succesful
            sensor operation.
68      digitalWrite(trigPin, HIGH);
69      delayMicroseconds(10);  // this delay is required as well!
70      digitalWrite(trigPin, LOW);
71
72      travel_time = pulseIn(echoPin, HIGH);  // calculate the travel
            time of pulse
73      distance_1 = (travel_time / 2) / 29.1;  // calculate distance
            of obstacles
74      Serial.println(distance_1);
75      return distance_1;
76    }
77
78    void move_forward(){
79      motor1.run(FORWARD);
80      motor2.run(FORWARD);
81    }
82
```

```
83  void move_backward(){
84    motor1.run(BACKWARD);
85    motor2.run(BACKWARD);
86  }
87
88  void turn_right(){
89    motor1.run(FORWARD);
90    motor2.run(BACKWARD);
91  }
92
93  void turn_left(){
94    motor1.run(BACKWARD);
95    motor2.run(FORWARD);
96  }
```

Vita

Shuyang Chen was born in Xinxiang, China on September 26, 1991. He received his Bachelor's degree in Mechanical Engineering from Beijing Institute of Technology in 2014, and enrolled in the Mechanical Engineering M.S.E. program at Johns Hopkins University in 2014. His research focused on robot control & navigation, and robot assembly based on smart materials, especially shape memory polymers (SMPs).